UNIVERSITY OF SÃO PAULO
SÃO CARLOS SCHOOL OF ENGINEERING
DEPARTMENT OF STRUCTURAL ENGINEERING

Lucas Almeida Rocha

Bifurcating solutions of anisotropic disk problem in a constrained minimization theory of elasticity

Soluções bifurcantes do problema do disco anisotrópico em uma teoria de minimização com restrição de elasticidade

São Carlos

2021

Lucas Almeida Rocha

Bifurcating solutions of anisotropic disk problem in a constrained minimization theory of elasticity

VERSÃO CORRIGIDA

A versão original encontra-se na Escola de Engenharia de São Carlos

Master's dissertation submitted to the Department of Structural Engineering, São Carlos School of Engineering, University of São Paulo, in partial fulfillment of the requirements for the degree of Master of Science in Civil Engineering (Structures)

Concentration area: Structures

Advisor: Prof. Dr. Adair Roberto Aguiar

São Carlos

2021

Ficha catalográfica elaborada pela Biblioteca Prof. Dr. Sérgio Rodrigues Fontes da EESC/USP com os dados inseridos pelo(a) autor(a).

Rocha, Lucas Almeida
R672b Bifurcating solutions of anisotropic disk problem in a constrained minimization theory of elasticity / Lucas Almeida Rocha; orientador Adair Roberto Aguiar. São Carlos, 2021.

Dissertação (Mestrado) - Programa de Pós-Graduação em Engenharia Civil (Engenharia de Estruturas) e Área de Concentração em Estruturas -- Escola de Engenharia de São Carlos da Universidade de São Paulo, 2021.

1. Anisotropy. 2. Elasticity. 3. Constraint minimization. 4. Penalty method. 5. Finite element method. I. Título.

Eduardo Graziosi Silva - CRB - 8/8907

FOLHA DE JULGAMENTO

Candidato: Engenheiro **LUCAS ALMEIDA ROCHA.**

Título da dissertação: "Soluções bifurcantes do problema do disco anisotrópico em uma teoria de minimização com restrição de elasticidade".

Data da defesa: 09/03/2021.

Comissão Julgadora	**Resultado**
Prof. Associado **Adair Roberto Aguiar (Orientador)** (Escola de Engenharia de São Carlos – EESC/USP)	**_Aprovado___**
Prof. Dr. **Roger Lee Fosdick** (Universidade de Minnesota)	**_ Aprovado ___**
Dr. **Antônio André Novotny** (Laboratório Nacional de Computação Científica/LNCC)	**_ Aprovado ___**

Coordenador do Programa de Pós-Graduação em Engenharia Civil (Engenharia de Estruturas):
Prof. Associado **Vladimir Guilherme Haach**

Presidente da Comissão de Pós-Graduação:
Prof. Titular **Murilo Araujo Romero**

ACKNOWLEDGEMENTS

First of all, this study was financed in part by the Coordenação de Aperfeiçoamento de Pessoal de Nível Superior – Brasil (CAPES) – Finance Code 001, to which I am very grateful. I would also like to thank my advisor Professor Adair Roberto Aguiar for his patience and all the great guidance provided along this work.

I am also very grateful to my parents and my brother for their unconditional support not only in these past two years, but in all my life. My friends also deserve my gratitude for all the discussions we had as well as distractions that made these past two years much more pleasant.

I would also like to acknowledge all professors I had, without whom I would not be here today. A special thanks to Professor Julián Bravo-Castillero for the discussions that lead to the results of Section 5.2.4. Professor Julián was a visiting scholar at EESC/USP in 2019 and was supported by the PRInt USP/CAPES program, grant # 88887.372694/2019−00. I am also very grateful to the members of the examining committee, Professor Roger Lee Fosdick and Professor Antonio André Novotny, for their valuable suggestions.

Last but not least, I also express my gratitude to the wonderful staff of the Department of Structural Engineering of EESC/USP, who always assisted me in any issue I had in these past two years.

Thank you all!

ABSTRACT

Rocha, L. A. **Bifurcating solutions of anisotropic disk problem in a constrained minimization theory of elasticity**. 2021. 128p. Dissertation (M. Sc. in Civil Engineering (Structural Engineering)) - São Carlos School of Engineering, São Carlos, 2021.

This work concerns the study of problems whose solutions in classical linear elasticity theory predict material overlapping, which is not physically admissible. To eliminate this anomalous behavior, we consider a theory that minimizes the total potential energy of the classical linear elasticity subject to the constraint that the deformation field is locally injective. We apply this theory, together with an interior penalty method and a standard finite element formulation, to obtain numerical solutions that do not exhibit material overlapping. We consider the problem of an anisotropic n-dimensional solid sphere, $n = 2, 3$, of radius R_e compressed along its boundary in the context of this constrained minimization theory. First, we assume that the solutions for both cases, $n = 2$ and $n = 3$, are radially symmetric and reproduce results found in the literature with the aim of validating the computational procedure. We then assume the existence of a second solution of the disk problem ($n = 2$) that is rotationally symmetric and formulate this problem in a one-dimensional domain $(0, R_e)$, instead of the original two-dimensional domain. We compare results obtained from the numerical solution of this problem with computational results found in the literature, which were obtained by considering an asymmetric displacement field defined in a two-dimensional domain. Both solutions predict that the local injectivity constraint is active only in an annulus of inner radius R_a and outer radius R_b. Despite this good agreement, away from the center of the disk, the rotationally symmetric solution is similar to the classical solution and the asymmetric solution is similar to the radially symmetric solution of the constrained minimization theory. To verify the validity of our computational solution, we search numerically for asymmetric solutions defined in the original two-dimensional domain. In addition, we find an analytical expression for the rotationally symmetric solution in the interval $(0, R_a) \cup (R_b, R_e)$ that depends on constants of integration whose values are determined from our computational results. Both approaches, computational and analytical, confirm the existence of the rotationally symmetric solution found computationally. Besides, our results clearly suggest that we must introduce a perturbation in the tangential displacement to obtain the rotationally symmetric solution. Otherwise, we obtain only the radially symmetric solution. Our results indicate that, for a fixed mesh, there are both a maximum shear modulus above which and a minimum load below which the rotationally symmetric solution cannot be obtained. It seems, however, that no threshold values exist in the limit case of an infinitely refined mesh. Moreover, the rotationally symmetric solution yields a lower value of the total potential energy functional when compared to the radially symmetric solution. Finally, we

use a regular perturbation method to find approximate solutions of the disk problem in the context of the classical linear elasticity theory and verify that these solutions converge to the closed-form solution of the problem as a perturbation parameter tends to zero. This study aims to use this method to investigate more complex problems for which closed-form solutions are not known.

Keywords: Anisotropy. Elasticity. Constraint minimization. Penalty method. Finite element method.

RESUMO

Rocha, L. A. **Soluções bifurcantes do problema do disco anisotrópico em uma teoria de minimização com restrição de elasticidade**. 2021. 128p. Dissertação (Mestrado em Ciências - Engenharia Civil (Engenharia de Estruturas)) - São Carlos School of Engineering, São Carlos, 2021.

Neste trabalho estudam-se problemas cujas soluções no contexto da teoria da elasticidade linear clássica predizem auto-intersecção de material. Para eliminar este comportamento fisicamente inadmissível, considera-se uma teoria que minimiza o funcional de energia potencial total da elasticidade linear clássica sujeito à restrição de que a deformação seja localmente injetiva. Utiliza-se essa teoria, juntamente com um método de penalidades interiores e uma formulação de elementos finitos clássica, para obter soluções numéricas que não predizem auto-intersecção. Neste trabalho, considera-se o problema de uma esfera anisotrópica n-dimensional, $n = 2, 3$, de raio R_e comprimida ao longo de seu contorno no contexto dessa teoria de minimização com restrição. Primeiramente, assume-se que as soluções em ambos os casos, $n = 2$ e $n = 3$, são radialmente simétricas e reproduzem-se resultados disponíveis na literatura com o objetivo de validar o procedimento computacional. Em seguida, assume-se a existência de uma segunda solução para o problema do disco ($n = 2$) que é rotacionalmente simétrica, e formula-se o problema em um domínio unidimensional $(0, R_e)$, em vez do domínio bidimensional original. Compara-se a solução numérica desse problema com resultados computacionais disponíveis na literatura, que foram obtidos considerando-se um campo de deslocamento assimétrico definido em um domínio bidimensional. Ambas as soluções predizem que a restrição de injetividade local está ativa apenas em um anel de raio interno R_a e raio externo R_b. Apesar dessa semelhança, longe do centro do disco, a solução rotacionalmente simétrica é similar à solução clássica, enquanto que a solução assimétrica é similar à solução radialmente simétrica da teoria de minimização com restrição. Para verificar a validade da nossa solução computacional, busca-se numericamente por soluções assimétricas definidas no domínio bidimensional original. Também determina-se uma expressão analítica para a solução rotacionalmente simétrica no intervalo $(0, R_a) \cup (R_b, R_e)$ que depende de constantes de integração cujos valores são determinados a partir de nossos resultados computacionais. Ambas as abordagens, computacional e analítica, confirmam a existência da solução rotacionalmente simétrica obtida computacionalmente. Além disso, nossos resultados sugerem que a introdução de uma perturbação no deslocamento tangencial é necessária para a obtenção da solução rotacionalmente simétrica. Caso contrário, somente a solução radialmente simétrica é obtida. Nossos resultados também indicam que, para uma dada malha, existe um módulo de cisalhamento máximo acima do qual e um carregamento mínimo abaixo do qual a solução rotacionalmente simétrica não pode ser obtida. Entretanto esses valores limites

parecem não existir para o caso de uma malha refinada infinitamente. Ademais, a solução rotacionalmente simétrica resulta em um menor valor de funcional de energia potencial total quando comparada à solução radialmente simétrica. Por fim, utiliza-se um método de perturbações regulares para determinar soluções aproximadas do problema do disco no contexto da teoria da elasticidade linear clássica, e verifica-se que essas soluções convergem para a solução fechada do problema à medida que um parâmetro de perturbação tende a zero. Esse estudo tem como objetivo a utilização desse método na investigação de problemas mais complexos para os quais soluções fechadas sejam desconhecidas.

Palavras-chave: Anisotropia. Elasticidade. Minimização com restrição. Método das penalidades. Método dos elementos finitos.

LIST OF FIGURES

LIST OF TABLES

CONTENTS

1 INTRODUCTION

1.1 Presentation and motivation

Some problems of practical interest, such as the arbitrary loading of solids containing cracks along interfaces of dissimilar media and uniform compression of solid anisotropic disks and spheres, have solutions in the context of the classical linear elasticity theory that predict material overlapping, which, of course, is not physically realistic. To prevent this anomalous behavior, we consider a constrained minimization theory, which minimizes the total potential energy functional of linear elasticity subject to the local injectivity constraint.

Mathematically, material overlapping is characterized by the loss of injectivity of the deformation field, which is locally represented by the violation of the positiveness of the determinant of the deformation gradient. This anomalous behavior is usually associated with singular stresses and strains, which violates the basic assumption of linear elasticity that the displacement gradient is infinitesimal.

This anomalous behavior motivates the search of solutions in the context of others theories. One possible way consists of adopting a proper nonlinear elastic behavior for the material, as considered by Aguiar and Fosdick (2001). They have eliminated the anomalous behavior of material interpenetration by proposing a modified semi-linear material with the same asymptotic behavior studied by Knowles and Sternberg (1975).

Fosdick and Royer-Carfagni (2001) proposed a different approach. The authors minimize the classical energy functional of linear elasticity subject to a local injectivity constraint, which consists of imposing that the determinant of the deformation gradient is not less than an arbitrarily small positive parameter. The associated constrained minimization problem is highly nonlinear and usually requires numerical solution. Obeidat et al. (2001) proposed a finite element approach, together with a Lagrange multiplier technique to impose the local injectivity constraint. Although the numerical results were in good agreement with analytical results of Fosdick and Royer-Carfagni (2001), this approach required a carefully designed algorithm that is difficult to apply when the region where the overlapping region is not known in advance.

Aguiar (2006) proposed a different numerical procedure to determine an approximate solution for the constrained minimization problem. It is based on an interior penalty formulation, where he searched for minimizers of a penalized energy functional $\mathcal{E}_\delta = \mathcal{E} + \mathcal{P}/\delta$, where $\mathcal{E}$ is the total potential energy of linear elasticity, δ is an arbitrary positive number, and $\mathcal{P}$ is a non-negative functional defined on a constraint set $\mathcal{A}_\varepsilon$, which is the set of all admissible deformations that satisfy the local injectivity constraint. Aguiar (2006)

used this formulation to obtain an injective solution for the problem of a spherically anisotropic homogeneous sphere compressed by a uniform normal pressure. In the context of classical linear elasticity, Ting (1998) showed that the solution of this problem predicts self-intersection at the center of the sphere for a range of plausible material parameters.

In two dimensions, Lekhnitskii (1968) studied the analogous problem of a cylindrically anisotropic homogeneous disk subject to a uniform pressure. The author determined a closed form solution in the context of classical linear elasticity, which predicts stress singularities for materials with elastic modulus in radial direction being greater than the elastic modulus in tangential direction. Material properties of this type are found in carbon fibers with radial microstructure (CHRISTENSEN, 1994). In addition to stress singularities, Fosdick and Royer-Carfagni (2001) also found that this material intersects itself in a vicinity of the center of the disk.

In the context of the theoretical framework introduced by Fosdick and Royer-Carfagni (2001), the corresponding Lekhnitskii problem has a solution that is radially symmetric with respect to the center of the disk, which is different from the radially symmetric solution of classical linear elasticity.

Using the numerical procedure proposed by Aguiar (2006), Fosdick, Freddi and Royer-Carfagni (2008) found that a second solution is possible for low enough shear modulus. This solution was obtained numerically by using a very fine mesh of biquadratic finite elements to approximate both the solution and the geometry of the disk in two dimensions.

This work aims at contributing to the theory proposed by Fosdick and Royer-Carfagni (2001), which, in a way similar to the theory of classical linear elasticity, may be understood as the first step to investigate the more encompassing nonlinear theory. In this work we consider the problem of an anisotropic n-dimensional solid sphere, $n = 2, 3$, subject to uniform normal pressure in the context of the constrained minimization theory of Fosdick and Royer-Carfagni (2001). If $n = 2$, we have the disk problem investigated by Lekhnitskii (1968) in the context of the classical linear theory and by Fosdick and Royer-Carfagni (2001) and Aguiar, Fosdick and Sánchez (2008) in the context of both constrained and unconstrained theories. If $n = 3$, we have the sphere problem studied by Ting (1998) in the context of the classical linear theory and by Aguiar (2006) in the context of both the constrained and unconstrained theories. First, we assume that the solutions for both cases, $n = 2$ and $n = 3$, are radially symmetric and reproduce results obtained by these authors with the aim of validating the computational procedure. We then turn our attention to a numerical investigation of the disk problem ($n = 2$) and look for a solution that is rotationally symmetric, which means that distinct radial lines emanating from the center of the disk are deformed into curves that, although rotated, have the same shape. This assumption has allowed us to formulate the disk problem on a

one-dimensional domain, which is different from the approach used by Fosdick, Freddi and Royer-Carfagni (2008), who searched for an asymmetric solution of this problem defined in the original two-dimensional domain. In the first part of this investigation we compare our computational results with computational results obtained by these authors and find that, overall, there is good quantitative agreement. There are, however, some differences related to the radial component of the deformation, which has motivated a further study of the problem. Relevant topics of study include a discussion about the conditions for obtaining either the radially or rotationally symmetric solution and the derivation of a general expression for the rotationally symmetric solution of the Euler-Lagrange equations of the constrained optimization problem that depends on constants of integration that can be determined numerically. This expression has confirmed the numerical results found in this work at a low computational cost.

1.2 Objectives

The general objective of this work is to contribute to the development of a constrained minimization theory in elasticity by investigating problems of practical interest having solutions that predict material overlapping in the context of the classical linear elasticity theory. Specific objectives are presented below and concern the approximate solutions of some constrained minimization problems. Initially, solutions of these problems are compared to solutions found in the literature and are used to validate the computational scheme. As the problems become more complex, sequences of these solutions are constructed to investigate numerical convergence and to obtain new insight on the constrained theory.

1. Radially symmetric solution of the spherically anisotropic homogeneous sphere problem, which is called the Ting's problem after the work of Ting (1998). We obtain numerical results in the context of the constrained theory that are in very good agreement with both analytical and computational results obtained by Aguiar (2006).

2. Radially symmetric solution of the cylindrically anisotropic homogeneous disk problem, which is called the Lekhnitskii's problem after the work of Lekhnitskii (1968). Again, we obtain numerical results in the context of the constrained theory that are in very good agreement with analytical results obtained by Fosdick and Royer-Carfagni (2001) and with computational results obtained by Aguiar, Fosdick and Sánchez (2008) in the particular case of a disk with no hole.

3. Rotationally symmetric solution of the constrained Lekhnitskii's problem, which is the main contribution of this work. The displacement field has both radial and tangential components that depend only on the radius of the disk in its undeformed

configuration. We compare our computational results with computational results obtained by Fosdick, Freddi and Royer-Carfagni (2008) and find that, overall, there is good quantitative agreement. Some differences have motivated a further study of the problem. In addition of being able to verify numerical convergence of the approximate solutions at low computational cost, we investigate numerically the conditions for bifurcation from the radially symmetric solution to the rotationally symmetric one.

4. Asymmetric solution of the constrained Lekhnitskii's problem to verify the results obtained from the investigation in Objective 3. Here, no assumptions are made on the displacement field, which has the radial and tangential components depending on both the radial and azimuthal directions in the undeformed configuration of the disk. The asymmetric solution obtained is, in fact, rotationally symmetric, which confirms the solution determined in Objective 3.

5. General form of the rotationally symmetric solution of the constrained Lekhnitskii's problem in the region of the domain where the injectivity constraint is inactive. We partially solve the Euler-Lagrange equations of the constrained minimization problem to obtain analytical expressions for the rotationally symmetric solution. These expressions are in very good agreement with the solution obtained computationally in Objective 3.

1.3 Structure of the dissertation

In Chapter 2 we review the literature on material overlapping. We focus on three situations where material overlapping occurs, which concern the vicinity of crack tips, the vicinity of corners and interior points of anisotropic solids.

In Chapter 3 we present background material on concepts and principles of mechanics and how the linear elasticity is derived from a more encompassing nonlinear elasticity theory. The chapter ends with a review of the constrained minimization theory proposed by Fosdick and Royer-Carfagni (2001).

In Chapter 4 we review the numerical procedure proposed by Aguiar (2006), which is used in this work to determine minimizers for constrained minimization problems. The procedure is based on an interior penalty formulation, where we determine approximate minimizers through a standard finite element formulation together with a minimization algorithm that is based on the Newton-Raphson method and a line search.

In Chapter 5 we search for radially symmetric displacement fields for the problem of a n-sphere, $n = 2, 3$, subject to a uniform pressure along its boundary in the context of the constrained theory. The case $n = 2$ refers to Lekhnitskii's problem and the case $n = 3$ refers to Ting's problem. In Section 5.1 we formulate those problems and present

expressions for the functionals to be minimized using the procedure describe in the previous chapter. In Section 5.2 we review results reported in the literature concerning closed form solutions for those problems. We also determine an asymptotic approximate solution for the Lekhnitskii disk problem in the context of the classical linear elasticity. In Section 5.3 we present numerical results that are in very good agreement with numerical and analytical results reported in the literature, which represents a first step towards the goal of validating the computational code.

In Chapter 6 we focus on the Lekhnitskii problem and look for both rotationally symmetric and asymmetric minimizers of the corresponding constrained minimization problem. This investigation represents the main contribution of this work. Section 6.1 is analogous to Section 5.1 in the sense that we present the problem formulation, which, here, is based on the assumption that the solution is rotationally symmetric. In Section 6.2 we present numerical results and discuss different aspects of the simulation. In Section 6.2.1 we discuss about the necessity of both a very refined mesh and an appropriate initial guess for the search of a secondary solution of the constrained disk problem, being the choice of the latter very critical in this respect. In Section 6.2.2 we present convergent sequences of approximate solutions that are rotationally symmetric. These solutions yield computational results that are, overall, in good quantitative agreement with their counterparts presented by Fosdick, Freddi and Royer-Carfagni (2008). Some observed differences served as a motivation for further study of the rotationally symmetric solutions. In Section 6.2.3 we investigate the influence of the shear modulus on the existence of the secondary solution. In particular, we find numerically a maximum shear modulus beyond which a secondary solution does not exist. In Section 6.2.4 we study the influence of the loading on the existence of the rotationally symmetric solution. In Section 6.2.5 we consider asymmetric minimizers, instead of minimizers that are rotationally symmetric, and solve the constrained minimization problem numerically in a two dimensional domain with the goal of verifying the results obtained in previous sections. Two different formulations are considered, which yield approximate solutions that confirm the previous results. In Section 6.2.6 we discuss some numerical aspects pointed out in the previous sections. In Section 6.3 we use a combination of analytical and computational approaches to obtain a rotationally symmetric solution of the Euler-Lagrange equations corresponding to the constrained minimization disk problem in the region where the injective constraint is not active. Specifically, we find general expressions of the displacement field in this region, which depend on integration constants that can be determined from our computations. We then verify that, as the mesh is refined, the numerical solutions converge to this analytical solution. This procedure allows us to determine analytically the region where the constraint is active and compare it with the corresponding region obtained numerically.

In Chapter 7 we present some concluding remarks.

2 LITERATURE REVIEW ON MATERIAL OVERLAPPING

The theory of elasticity concerns the study of the behavior of those bodies that possess the property of recovering their original shapes when the forces producing deformations are removed (SOKOLNIKOFF, 1956). In particular, the classical linear theory of elasticity, whose underlying assumption is that the deformations are infinitesimal, yields accurate results in several engineering applications. In some applications, however, the linear theory may predict physically unrealistic behavior, such as material overlapping, which is the subject of this investigation. In this chapter we review some studies of this unrealistic behavior in the vicinity of crack tips, corners, and interior points. Unless stated otherwise, these studies were made in the context of classical linear elasticity.

2.1 Vicinity of crack tips

Williams (1959) considered two isotropic homogeneous half-planes separated by a traction-free crack along part of the interface, as illustrated in Figure 1. Possible applications concern the study of fault lines along the interface between two layers of rock strata. Near the crack tip, the author shows that the stress field possess a sharp oscillatory behavior of the type

$$r^{-\frac{1}{2}} \sin(b \log r), \tag{2.1}$$

where b is a function of material constants and r is the distance from the crack tip. Note from (2.1) the stress singularity at $r = 0$.

England (1965) extended the work of Williams (1959). The author shows that the solution to the problem of two bonded half-planes having a single crack along their interface and opened by an internal pressure applied on the crack surfaces is physically inadmissible, because such a solution predicts that the upper and lower surfaces of the crack should overlap near the ends of the crack.

Comninou (1977) assumed that there is a small frictionless contact zone near the crack tips. With this assumption, the solution did not present the unrealistic oscillatory singularities, nor the material overlapping between the crack surfaces. However, the shear stress component presented a square root singularity ahead of the crack tip, which suggested that the growth of an interface crack is more connected with failure in shear.

Aravas and Sharma (1991) considered the problem of a crack lying along the interface of an elastoplastic medium and a rigid substrate, as illustrated in Figure 2. The authors also discussed the elastic case and showed that asymptotic solutions based on the assumption that the vicinity of the crack tips remain closed still predicts material interpenetration. The anomalous behavior occurs in the interface between the materials in

Figure 1 – Crack along the interface of two isotropic homogeneous half-planes.

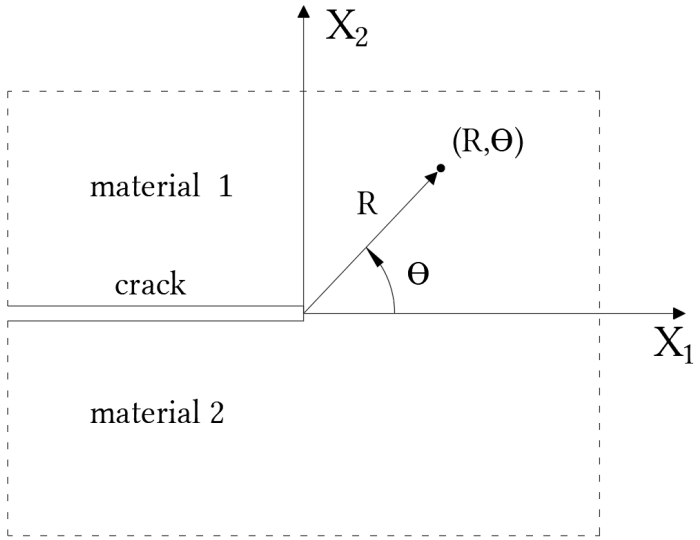

Source: Adapted from Williams (1956).

a neighborhood of the crack tip. This observation limits the applicability of the asymptotic solution of Comninou (1977) when the predicted size of the contact zone is small compared to the crack length. Moreover, the classical solutions, which assume that the crack faces are traction-free, are valid over distances larger than the contact zone but still small compared to the crack length.

Figure 2 – Crack along the interface of an elastoplastic medium and a rigid substrate.

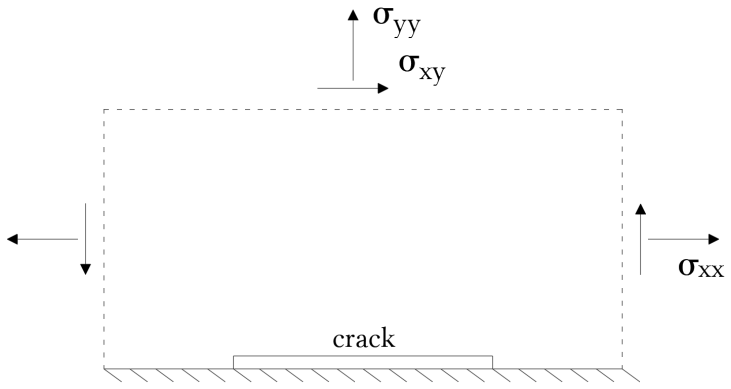

Source: Adapted from Aravas and Sharma (1991).

2.2 Vicinity of corners

Muskhelishvili (1977) considered the bonded punch problem in the context of linear elasticity, i.e., a plane-strain problem for a half-plane that arises when a finite segment of the boundary is forced to undergo a translation by means of an axially loaded flat-ended rigid punch that is bonded to this finite segment of the boundary. The remainder of the boundary, as well as points at infinity, are assumed to be traction-free. The problem is illustrated in Figure 3. The author showed that the stress changes its sign an infinite number of times as we approach the punch corner. This oscillatory character is the same as that observed by Williams (1959) for the crack problem. Moreover, the stress becomes unbounded as either corner is approached.

Figure 3 – Bonded punch problem.

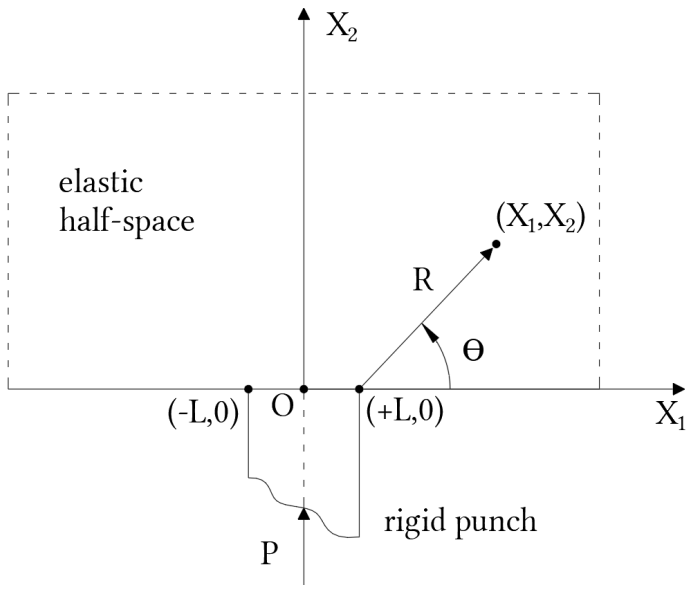

Source: Adapted from Knowles and Sternberg (1975).

Williams and Pasadena (1952) investigated stress singularities in the angular corner of a circular sector plate in extension. The authors considered three possibilities for the boundary conditions imposed on the straight sides of the circular sector: free-free, clamped-clamped and clamped-free. It was found that, when the angle is less than 180°, unbounded stress may occur at the vertex only for the mixed boundary condition, i.e., the clamped-free case. For angles between 180° and 360°, all the considered cases may present unbounded stresses.

Knowles and Sternberg (1975) investigated the singularities induced by certain mixed boundary conditions in the context of both linear and nonlinear elasticity. In the context of the classical linear elasticity, the authors reviewed results of Williams and Pasadena (1952) concerning an angle of 180° and the clamped-free case, which corresponds

to a mixed boundary condition. To illustrate it, the authors considered the bonded punch problem. They argued that the well known infinitely sign reversals of the stress in the vicinity of either corners implies that a compressive load applied to the bonded punch generates tensile traction near the corner. Therefore, a rigid flat-indenter that is pressed against a semi-infinite elastic solid with enough friction to prevent any lateral displacement along the contact zone could not maintain a full contact with the indented solid. Then, the authors showed that for a particular class of nonlinear elastic materials, this oscillatory behavior is removed.

Aguiar and Fosdick (2001) contributed to the investigation of the deformation field in the vicinity of the punch corners. The authors did an asymptotic and a computational analysis of the deformation field in the context of the linear and nonlinear plane-strain theories. In the nonlinear theory they used the semi-linear material introduced by John (1960) to model material behavior away from singular points and a subclass of harmonic materials that follow the same asymptotic constitutive structure proposed by Knowles and Sternberg (1975) to model the material behavior near these points. The resulting material model is called the modified semi-linear material. The authors showed that, in the vicinity of the punch corners, the stress field has a square root singularity. In addition, the linear and semi-linear materials predict material overlapping and the modified semi-linear material does not.

Aguiar and Fosdick (2014) used the same modified semi-linear material of Aguiar and Fosdick (2001) to investigate the behavior of the deformation field in the vicinity of the vertex of a wedge-shaped elastic body of angle $\alpha \in (0, 2\pi]$ subjected to zero traction and zero displacement conditions on either side of the vertex. On the circular arc of angle α, the displacement field was assumed to be known and smooth. The authors used a complex variable formulation to determine general expressions for the stress and deformation fields in terms of two analytic functions. The authors obtained a physically possible deformed free surface, which is similar to the free surface in the vicinity of the corners of the punch considered by Aguiar and Fosdick (2001).

2.3 Interior points

Lekhnitskii (1968) considered the problem of a cylindrically anisotropic homogeneous circular disk of radius R_e compressed along its external boundary by a uniform normal pressure p per unit of length, as illustrated in Figure 4. The author showed that, in the context of linear elasticity, the radial and hoop stresses are given by, respectively,

$$\sigma_{rr}(R) = p\left(\frac{R}{R_e}\right)^{k-1}, \qquad \sigma_{\theta\theta}(R) = pk\left(\frac{R}{R_e}\right)^{k-1}, \tag{2.2}$$

with $k \coloneqq \sqrt{E_\theta/E_r}$, where E_r and E_θ are the Young's modulus in the radial and tangential directions, respectively, and R is the distance from the center of the disk. The author also

showed the presence of a stress singularity at $R = 0$ for $k < 1$, that is, for $E_r > E_\theta$, a property that is observed in carbon fibers with radial microstructure (CHRISTENSEN, 1994).

Carbon fiber is a material employed by many industries, such as medical, construction, aerospace and military, because of its mechanical, thermal, and electric properties, which may differ significantly depending on its microstructure. In Figure 5 we show three different types of idealized microstructures. Each microstructure is characterized by the direction of the basal planes of graphite crystals in the transverse plane of the fiber. The alignment of these planes with the radial and the tangential directions characterizes the radial and the onion-skin microstructures, respectively. In addition, these planes may also have no particular alignment, which characterizes the random microstructure (HUANG, 2009).

The basal planes are carbon atom layers arranged in a hexagonal pattern, as illustrated in Figure 6. We see from this figure that the atoms are covalently bonded within the basal planes. Between basal planes, the forces are due to van der Waals forces, which are much weaker than the covalent forces. This arrangement of atoms together with the types of forces that keep them together explain the strongly anisotropic behavior found in carbon fibers (CHRISTENSEN, 1994).

Figure 4 – Anisotropic disk compressed by a uniform pressure along its external boundary.

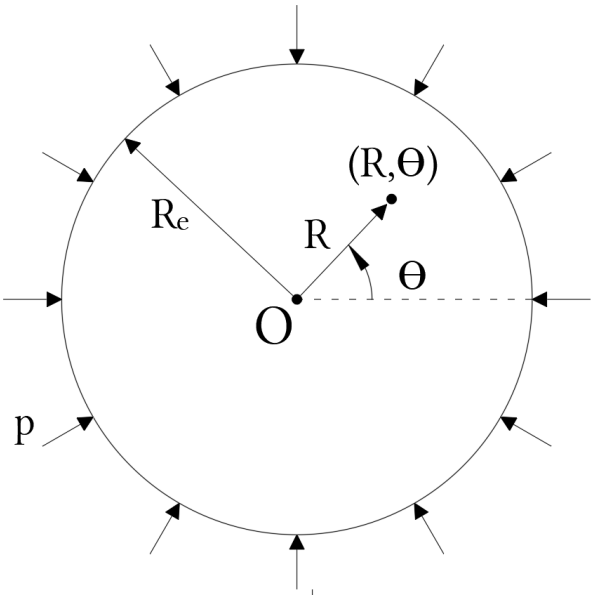

Source: The author.

Antman and Negrón-Marrero (1987) considered a sphere of nonlinear elastic material in equilibrium with no body force and subject to a uniform pressure applied on the surface of the sphere. The material is transversely isotropic with the radial axis being the axis of

Figure 5 – Types of carbon fiber microstructure.

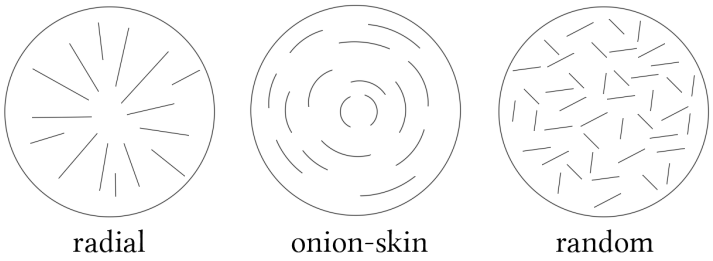

Source: Adapted from Christensen (1994).

Figure 6 – Basal planes of an ideal crystal graphite structure.

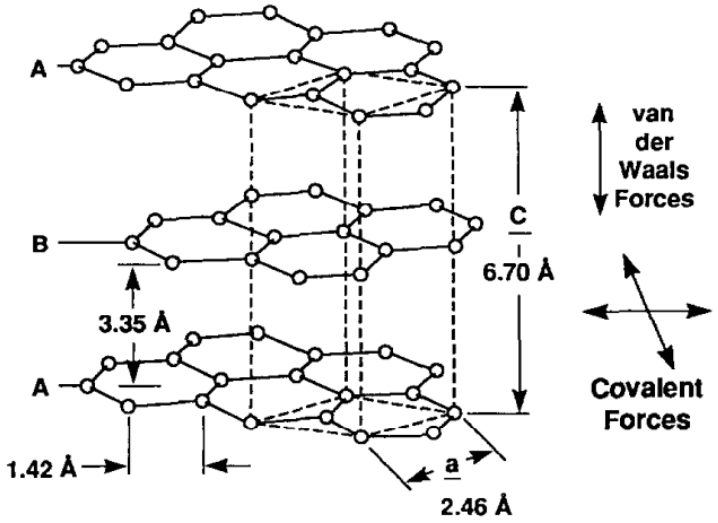

Source: Adapted from Christensen (1994).

symmetry. The authors showed that, for radially reinforced materials, the stress becomes unbounded at the center when the external pressure exceeds a critical value.

Ting (1998) also considered a sphere in equilibrium with no body force and subject to a uniform pressure applied on its external surface. Here, however, the sphere is made of a spherically uniform linear anisotropic elastic material. The author showed that the stress at the center may also become unbounded depending solely on the values of elasticity constants and not on the applied pressure.

To remove the anomalous behavior of material overlapping, Fosdick and Royer-Carfagni (2001) proposed to minimize the quadratic energy functional of classical linear

elasticity subject to the constraint of local injectivity, i.e., the determinant of the deformation gradient must not be less than an arbitrarily small positive value. This highly nonlinear constraint gives rise to an appropriate constraint reaction field. The authors prove an existence theorem for minimizers of plane problems and present the Euler-Lagrange equations for such problems. The authors then revisited the Lekhnitskii disk problem (LEKHNITSKII, 1968) and showed that, in addition to stress singularity, there is material interpenetration in a central core of the disk in the context of the classical linear elasticity theory when $E_r > E_\theta$. Using their constrained minimization theory and assuming that the displacement field is radially symmetric, i.e., the radial displacement depends only on the radius and the tangential displacement is zero, the authors found a closed form solution that does not predict material interpenetration, even when $E_r > E_\theta$.

The radial and onion-skin microstructures illustrated in Figure 5 are idealizations and may not exist up to the center of a carbon fiber. Tarn (2002) argued that, in reality, there must be a core made of, at most, a transversely isotropic material, because, in the center of the disk, the tangential direction at the polar angle Θ and the radial direction at $\Theta + \pi/2$ are indistinguishable. Tarn (2002) relied on this last argument to derive a closed-form solution for a composite cylinder in plane-strain equilibrium without body force and subject to a uniform pressure. The cylinder consists of an outer cylinder that is cylindrically anisotropic and a core that is transversely isotropic. The author verified that no stress singularities occur at the central axis of the cylinder, even for $E_r > E_\theta$. However, stress concentration still occurs as the radius of the inner core decreases. Tarn (2002) also stated that it is possible to show that the determinant of the deformation gradient is nonzero and positive in the whole composite cylinder, and therefore, no material overlapping occurs. As a simple check, the author discussed about the boundedness of the stress, however, no proof of the positiveness of the determinant of the deformation gradient was given. Later, Fosdick, Freddi and Royer-Carfagni (2008) showed that, although the solution of the compound cylinder problem considered by Tarn (2002) has bounded stresses, it still predicts material overlapping for a nonzero inner core radius.

Obeidat et al. (2001) proposed a numerical procedure to solve the Lekhnitskii disk problem (LEKHNITSKII, 1968) in the context of the constrained minimization theory. The procedure involved a finite element formulation together with a Lagrange multiplier technique to impose the local injectivity constraint. The region where the constraint is active is not known in advance, so the authors solved the problem iteratively. In the initial problem, the authors considered that the constraint was inactive in the entire disk. In the subsequent problems, they considered that the constraint was active in the region of the disk where the local injectivity constraint was violated in the previous problem. These problems should be solved until convergence of the solutions. However, this approach did not converge. The authors modified the above procedure by including in the active region, not only the points where local injectivity constraint is violated, but the entire

region where the material overlapping occurs. We will see in Section 5.2.1 that for the Lekhnitskii disk problem, this region is not limited by the points where the local injectivity constraint is violated. With this modified approach, the authors achieved convergence with no difficulties and a good agreement with analytical results of Fosdick and Royer-Carfagni (2001). However, it would be difficult to apply this procedure in more complex problems where the overlapping region is not known in advance.

Aguiar (2006) considered the problem investigated by Ting (1998) in the context of the constrained minimization theory. The author derived a closed form expression for the displacement field, which is radially symmetric with respect to the center of the sphere. The author also used the Finite Element Method together with an interior penalty formulation to solve the corresponding constrained minimization problem numerically, obtaining results that are in good agreement with the analytical results. This formulation is general and can be applied in the analysis of constrained minimization problems of elasticity in any dimension. In this approach, one determines the displacement field $\mathbf{u}$ which minimizes a penalized functional $\mathcal{E}_\delta = \mathcal{E} + \mathcal{P}/\delta$, where $\mathcal{E}$ is the total potential energy of linear elasticity, $\delta > 0$ is a penalty parameter and $\mathcal{P}$ is a penalty functional defined on the set of all kinematically admissible displacement fields $\mathcal{A}_\varepsilon$. The penalty functional must be positive and satisfy $\mathcal{P}[\mathbf{u}] \to \infty$ as $\mathbf{u}$ approaches the boundary of $\mathcal{A}_\varepsilon$. In addition, this sequence converges to the solution of the original constrained minimization problem as the penalty parameter tends to infinity. The minimization of the penalized functionals remains a constrained problem, since the minimizers are still searched in the constraint set $\mathcal{A}_\varepsilon$. However, it can be minimized by standard optimization methods from classical nonlinear programming, which is an advantage of this numerical procedure.

Aguiar, Fosdick and Sánchez (2008) considered the constrained theory and solved the problem of a circular homogeneous and anisotropic pipe fixed at its inner surface, radially compressed along its outer surface by a uniform pressure, and subjected to an axial force acting on its flat ends, as shown in Figure 7. This problem, in the context of classical linear elasticity, yields an example of material overlapping occurring in the absence of singularities. The authors obtained a closed form expression for the displacement field, which is radially symmetric. In a way similar to the numerical scheme proposed by Aguiar (2006), the authors used the Finite Element Method together with both interior and exterior penalty formulations to solve the corresponding constrained minimization problem numerically, obtaining results that are in good agreement with the analytical results. In the exterior penalty formulation, one determines the displacement field $\mathbf{u}$ that minimizes the penalized functional $\mathcal{E}_\delta = \mathcal{E} + \delta\,\mathcal{P}_e$, where $\mathcal{P}_e$ is a non-negative penalty functional such that $\mathcal{P}_e[\mathbf{u}] = 0$ iff $\mathbf{u} \in \mathcal{A}_\varepsilon$. The same remark concerning generality and applicability of the interior penalty formulation is valid for the exterior penalty formulation.

Fosdick, Freddi and Royer-Carfagni (2008) revisited the Lekhnitskii disk problem

Figure 7 – Anisotropic pipe fixed at its inner surface and radially compressed by a uniformly distributed pressure along its outer surface.

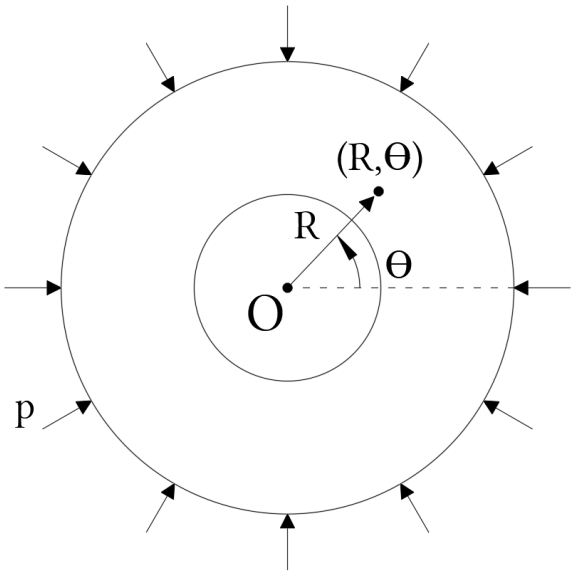

Source: The author.

in the context of the constrained minimization theory. The authors made no assumption of symmetry in the displacement field, which has radial and tangential components defined in a two-dimensional domain. Using the numerical scheme proposed by Aguiar (2006), the authors recovered the radially symmetric displacement field derived by Fosdick and Royer-Carfagni (2001) for a particular set of elastic constants. However, when the shear modulus was taken sufficiently small, the authors obtained a displacement field that is no longer radially symmetric. In this secondary solution, referred by the authors as asymmetric solution, it seems that all the radial lines undergo the same rotation with respect to the center of the disk. In addition, they observed a 180-degree rotation of a central core of the disk, as shown in the Figure 8. These observations have motivated our investigations in Chapter 6 to look for a rotationally symmetric solution of the Lekhnitskii problem in the context of the constrained minimization theory. As remarked above, the radial and tangential displacements depend only on the radius and, therefore, the domain of definition of the ensuing problem is the interval between zero and the external radius of the disk.

Figure 8 – Deformed mesh of the asymmetric solution obtained by Fosdick, Freddi and Royer-Carfagni (2008) for the disk problem in the context of the constrained theory.

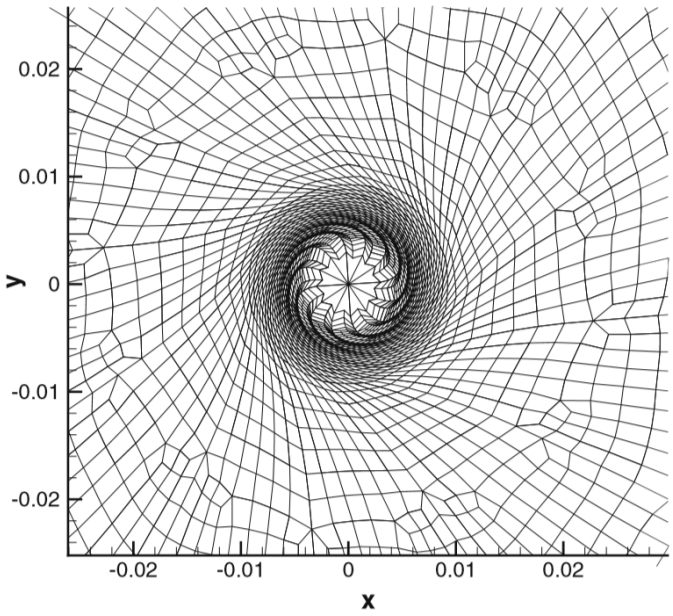

Source: Fosdick, Freddi and Royer-Carfagni (2008).

3 THEORETICAL BACKGROUND

In this chapter we present some theoretical results used in this work. We begin with kinematics, by presenting results about deformation, local injectivity, measures of strain and motion. Next, we introduce the balance laws and the constitutive assumptions used to model different material responses. We also present equivalent forms of representing the governing equations of elasticity through variational principles. We then show how the classical linear elasticity is derived from the more encompassing nonlinear elasticity theory. Finally, we present the constrained minimization theory by Fosdick and Royer-Carfagni (2001).

3.1 Kinematics

3.1.1 Body and deformation

A body is a collection of points distributed continuously throughout a region of the euclidean space at some time $t \geq 0$. These points are endowed with physical quantities, such as mass density, and, for this reason, are called material points. Here, a reference configuration $\mathcal{B}$ is a region occupied by the body at some fixed time, say, $t = 0$. Given a fixed orthonormal basis $\mathbf{e}_\alpha$ in $\mathbb{R}^3$, points of $\mathcal{B}$ are represented by $\mathbf{X} = X_\alpha\, \mathbf{e}_\alpha$, where, unless stated otherwise, implicit sum is assumed over the repeated indices $\alpha = 1, 2, 3$ throughout this work. Bounded regions within $\mathcal{B}$ are called parts $\mathcal{P}$. The deformation of a body is a mapping $\mathbf{f} : \mathcal{B} \to \mathbb{R}^3$ that maps each material point $\mathbf{X}$ into a point $\mathbf{x} \coloneqq \mathbf{f}(\mathbf{X}) = x_i\, \mathbf{e}_i$, $i = 1, 2, 3$. The region occupied by the body after deformation is called current or deformed configuration $\Omega \coloneqq \mathbf{f}(\mathcal{B})$.

If $d\mathbf{X}$ is a line element emanating from a material point $\mathbf{X}$ in the reference configuration, then its counterpart in the deformed configuration, which emanates from $\mathbf{x} = \mathbf{f}(\mathbf{X})$, is given by

$$d\mathbf{x} = \mathbf{F}\, d\mathbf{X}, \tag{3.1}$$

or, in term of components, by

$$dx_i = \frac{\partial x_i}{\partial X_\alpha} dX_\alpha, \qquad i, \alpha = 1, 2, 3, \tag{3.2}$$

where $\mathbf{F} \coloneqq \nabla \mathbf{f}$ is the deformation gradient relative to the reference configuration $\mathcal{B}$ and $\nabla(\cdot)$ denotes the gradient with respect to $\mathbf{X}$.

3.1.2 Local injectivity constraint

The vectors $d\mathbf{X}$ in $\mathcal{B}$ and $d\mathbf{x}$ in Ω are called, respectively, Lagrangian and Eulerian line elements. Equation (3.1) describes the transformation of a line element $d\mathbf{X}$ in $\mathcal{B}$ into a line element $d\mathbf{x}$ in the current configuration Ω.

Consider the volume dV of a parallelepiped generated by three noncoplanar line elements $d\mathbf{X}^{(1)}$, $d\mathbf{X}^{(2)}$ and $d\mathbf{X}^{(3)}$ emanating from the point $\mathbf{X}$ and the volume dv of a parallelepiped generated by three line elements $d\mathbf{x}^{(1)}$, $d\mathbf{x}^{(2)}$ and $d\mathbf{x}^{(3)}$ emanating from the point $\mathbf{x}$ and given by

$$d\mathbf{x}^{(i)} = \mathbf{F}\, d\mathbf{X}^{(i)} \qquad i = 1, 2, 3. \tag{3.3}$$

It is not difficult to show that

$$\det \mathbf{F} = \frac{dv}{dV}, \tag{3.4}$$

thus providing a physical meaning to the determinant of the deformation gradient $\det \mathbf{F}$. It follows from (3.4) and the physical principle that a volume $dV \neq 0$ is not allowed to become a volume $dv = 0$ after deformation that

$$\det \mathbf{F} \neq 0, \tag{3.5}$$

so that, $\mathbf{F}$ is a non-singular tensor. Furthermore, a deformation with $\det \mathbf{F} < 0$ cannot be reached by a continuous process from the reference configuration without violating (3.5), since the trivial deformation $\mathbf{f}(\mathbf{x}) = \mathbf{X}$ has $\det \mathbf{F} = 1$. Therefore, the restriction (3.5) becomes

$$\det \mathbf{F} > 0, \tag{3.6}$$

and is called the orientation-preserving condition in Mechanics, or, the local injectivity constraint in Mathematics.

3.1.3 Strain tensors

Using (3.1), we find that

$$|d\mathbf{x}|^2 - |d\mathbf{X}|^2 = d\mathbf{X} \cdot (\mathbf{F}^T\mathbf{F} - \mathbf{1})\, d\mathbf{X}, \tag{3.7}$$

where $|\cdot|$ denotes the euclidean norm and $\mathbf{1}$ is the identity tensor. Thus, if

$$\mathbf{F}^T\mathbf{F} - \mathbf{1} = \mathbf{0}, \tag{3.8}$$

the line element $d\mathbf{X}$ preserves its length and the material is said to be unstrained at $\mathbf{X}$. Otherwise, the material is said to be strained. Therefore, the tensor $\mathbf{F}^T\mathbf{F} - \mathbf{1}$ provides a measure of change in length of a line element and is used to define the Green - St-Venant strain tensor

$$\mathbf{E}_g \coloneqq \frac{1}{2}(\mathbf{F}^T\mathbf{F} - \mathbf{1}). \tag{3.9}$$

The displacement $\mathbf{u}$ of a material point $\mathbf{X}$ is defined as

$$\mathbf{u}(\mathbf{X}) \coloneqq \mathbf{f}(\mathbf{X}) - \mathbf{X}, \tag{3.10}$$

which together with the deformation gradient $\mathbf{F} \coloneqq \nabla \mathbf{f}$ yield the displacement gradient

$$\nabla \mathbf{u} = \mathbf{F} - \mathbf{1}. \tag{3.11}$$

It then follows from both (3.9) and (3.11) that $\mathbf{E}_g$ can be written as

$$\mathbf{E}_g = \frac{1}{2}(\nabla \mathbf{u} + \nabla \mathbf{u}^T + \nabla \mathbf{u}^T \nabla \mathbf{u}). \tag{3.12}$$

In the linear elasticity it is assumed that the displacement gradient $\nabla \mathbf{u}$ is small, causing the terms of order $o(\nabla \mathbf{u})$ to be neglected. It then follows from (3.12) that $\mathbf{E}_g$ can be approximated by the infinitesimal strain $\mathbf{E}$, which is defined by

$$\mathbf{E} \coloneqq \frac{1}{2}(\nabla \mathbf{u} + \nabla \mathbf{u}^T). \tag{3.13}$$

Note from the equation (3.8) together with the expression (3.9) and the approximation $\mathbf{E}_g \sim \mathbf{E}$ that $\mathbf{E} = \mathbf{0}$ satisfies (3.8) within an error $o(\nabla \mathbf{u})$, reinforcing the fact that $\mathbf{E}$ can only be used when $\nabla \mathbf{u}$ is infinitesimal.

3.1.4 Motion

A motion $\mathbf{f} : \mathcal{B} \times \mathbb{R} \to \mathbb{R}^3$ of the body $\mathcal{B}$ is a smooth one-parameter family of deformations, where the time t is the parameter. The place occupied by the material point $\mathbf{X}$ at time t is given by $\mathbf{x} = \mathbf{f}(\mathbf{X}, t)$. Similarly, the region occupied by the body $\mathcal{B}$ and the part $\mathcal{P}$ at time t are denoted as $\mathcal{B}_t = \mathbf{x}(\mathcal{B}, t)$ and $\mathcal{P}_t = \mathbf{x}(\mathcal{P}, t)$, respectively.

It is often convenient to work with the current configuration rather than with the reference configuration. For this reason, we introduce the trajectory

$$\mathscr{T} \coloneqq \{(\mathbf{x}, t) \,|\, \mathbf{x} \in \mathcal{B}_t,\ t \in \mathbb{R}\}. \tag{3.14}$$

We also define the velocity

$$\dot{\mathbf{x}}(\mathbf{X}, t) \coloneqq \frac{\partial}{\partial t}\mathbf{x}(\mathbf{X}, t), \tag{3.15}$$

the acceleration

$$\ddot{\mathbf{x}}(\mathbf{X}, t) \coloneqq \frac{\partial^2}{\partial t^2}\mathbf{x}(\mathbf{X}, t), \tag{3.16}$$

and the spatial description of the velocity

$$\mathbf{v}(\mathbf{x}, t) \coloneqq \dot{\mathbf{x}}(\mathbf{f}^{-1}(\mathbf{x}, t), t), \tag{3.17}$$

which represents the velocity of the material point that occupies the place $\mathbf{x}$ at time t. The terminology spatial description field refers to a function whose domain is $\mathscr{T}$, while material description field refers to a function with domain $\mathcal{B} \times t$.

3.2 Balance laws

3.2.1 Mass conservation

A material point occupying the position $\mathbf{x}$ at time t is endowed with a mass density $\rho(\mathbf{x}, t)$. We then have that the mass of a part of the body at time t, denoted by $\mathcal{P}_t$, is given by

$$m(\mathcal{P}_t) = \int_{\mathcal{P}_t} \rho(\mathbf{x}, t)\, dv. \tag{3.18}$$

Since a motion $\mathbf{f}$ cannot alter the mass of a part, the mass of that part is independent of the motion and, in particular, $m(\mathcal{P}) = m(\mathcal{P}_t)$, where $\mathcal{P} \subset \mathcal{B}$. We then have that

$$m(\mathcal{P}) = \int_{\mathcal{P}} \rho_0(\mathbf{X})\, dV = \int_{\mathcal{P}_t} \rho(\mathbf{x}, t)\, dv, \tag{3.19}$$

where $\rho_0(\mathbf{X})$ is the mass density in the reference configuration. Using (3.4), it follows from (3.19) that

$$\int_{\mathcal{P}} \rho(\mathbf{f}(\mathbf{X}, t), t)\ \det \mathbf{F}(\mathbf{X}, t)\, dV = \int_{\mathcal{P}} \rho_0(\mathbf{X})\, dV \tag{3.20}$$

or

$$\int_{\mathcal{P}} \left[\rho(\mathbf{f}(\mathbf{X}, t), t)\ \det \mathbf{F}(\mathbf{X}, t) - \rho_0(\mathbf{X})\right]\, dV = 0, \tag{3.21}$$

which holds for any part $\mathcal{P} \subset \mathcal{B}$. Thus, it follows from the Localization Theorem (GURTIN, 1981, p. 38) that the integrand of (3.21) must be null, yielding the local expression for the mass conservation in the reference configuration, given by

$$\rho_0(\mathbf{X}) = \rho \circ \mathbf{f}(\mathbf{X}, t)\ \det \mathbf{F}(\mathbf{X}, t), \tag{3.22}$$

where $\circ$ denotes the function composition symbol. Similarly, the local expression of the mass conservation in the current configuration may be derived. Since the mass of any part $\mathcal{P}_t \in \mathcal{B}_t$ remains constant over time, it follows from (3.19) that

$$\frac{d}{dt} m(\mathcal{P}) = \frac{d}{dt} \int_{\mathcal{P}_t} \rho(\mathbf{x}, t)\, dv = 0. \tag{3.23}$$

It follows from the Reynold's Transport Theorem (GURTIN, 1981, p. 78) that

$$\int_{\mathcal{P}_t} \left[\frac{d}{dt}\rho(\mathbf{x}, t) + \rho(\mathbf{x}, t)\, \operatorname{div} \mathbf{v}(\mathbf{x}, t)\right] dv = 0, \tag{3.24}$$

where $\operatorname{div}(\cdot)$ denotes the divergence with respect to $\mathbf{x}$. Since (3.24) holds for any part $\mathcal{P}_t \in \mathcal{B}_t$, applying again the Localization Theorem, one has the local expression of the mass conservation in the current configuration, which is given by

$$\frac{d}{dt}\rho(\mathbf{x}, t) + \rho(\mathbf{x}, t)\, \operatorname{div} \mathbf{v}(\mathbf{x}, t) = 0. \tag{3.25}$$

Since ρ_0 does not depend on time and, in this work, we use the material description of all the variables, it follows from (3.23) together with the first equality in (3.19) that mass conservation is identically satisfied.

3.2.2 Forces

Forces describe the mechanical interaction between parts of a body and the environment during a motion. Here, we consider two types of force: body and contact forces. Body forces are exerted on the interior points of a body by the environment; one typical example being the gravitational force. Contact or surface forces are exerted between two

surfaces, which can be from two parts of the same body, characterizing an interior contact force, or, between the boundary of a body and the environment, characterizing an exterior contact force.

The Cauchy's hypothesis or Cauchy's fundamental postulate is one of the most important axioms of continuum mechanics concerning contact forces. Cauchy's hypothesis states that the surface force per unit of area, $\mathbf{s}$, at place $\mathbf{x}$ and time t depends on the surface only through its unit normal $\mathbf{n}$ at $\mathbf{x}$ of the considered surface. An immediate consequence, proved in (GURTIN, 1981, p. 103), is the Newton's law of action and reaction, given by

$$\mathbf{s}(\mathbf{n}, \mathbf{x}, t) = -\mathbf{s}(-\mathbf{n}, \mathbf{x}, t). \tag{3.26}$$

Consider two smooth surfaces $\mathscr{S}_1$ and $\mathscr{S}_2$ in contact at $\mathbf{x}$ belonging respectively to the bodies $\mathcal{B}_1$ and $\mathcal{B}_2$, as illustrated in Figure 9. Equation (3.26) states that the contact force exerted by $\mathcal{B}_1$ on $\mathcal{B}_2$ and the force exerted by $\mathcal{B}_2$ on $\mathcal{B}_1$ have the same magnitude but opposite directions.

Figure 9 – Contact force between two smooth surfaces.

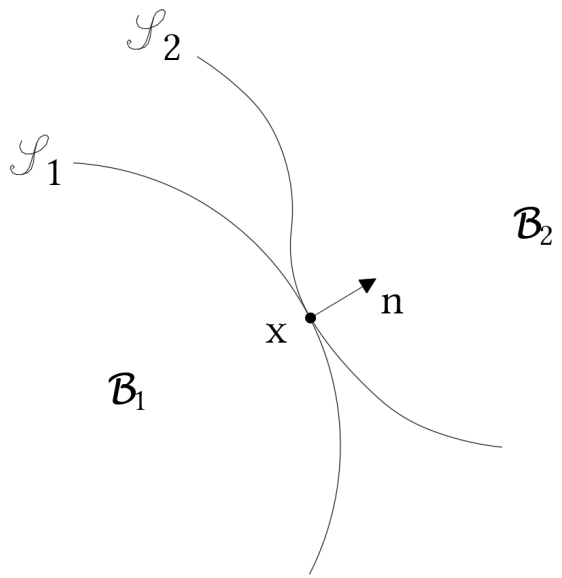

Source: Adapted from Gurtin (1981, p. 98).

To determine the total surface force exerted on a part $\mathcal{P}_t$ at time t, we simply integrate $\mathbf{s}$ over the boundary $\partial\mathcal{P}_t$, yielding

$$\int_{\partial\mathcal{P}_t} \mathbf{s}(\mathbf{n}, \mathbf{x}, t) dA. \tag{3.27}$$

Similarly, to determine the total body force exerted on a part $\mathcal{P}_t$ at time t by the environment, we integrate the body force $\mathbf{b}$ over the part $\mathcal{P}_t$, yielding

$$\int_{\mathcal{P}_t} \mathbf{b}(\mathbf{x}, t) dV. \tag{3.28}$$

3.2.3 Momentum balance laws

Momentum balance laws or Euler's laws of motion are based on Newtonian Mechanics and yield two governing equations in continuum mechanics. Considering the Cauchy's hypothesis and omitting dependence on the place $\mathbf{x}$ and time t, the balance of linear momentum is written as

$$\int_{\partial\mathcal{P}_t} \mathbf{s}(\mathbf{n})\, dA + \int_{\mathcal{P}_t} \mathbf{b}\, dV = \int_{\mathcal{P}_t} \dot{\mathbf{v}}\rho\, dV \tag{3.29}$$

and the balance of angular or rotational momentum as

$$\int_{\partial\mathcal{P}_t} \mathbf{r} \times \mathbf{s}(\mathbf{n})\, dA + \int_{\mathcal{P}_t} \mathbf{r} \times \mathbf{b}\, dV = \int_{\mathcal{P}_t} \mathbf{r} \times \dot{\mathbf{v}}\rho\, dV, \tag{3.30}$$

with $\times$ denoting the vector product, $\mathbf{r} \coloneqq \mathbf{x} - \mathbf{o}$ the position vector and $\mathbf{o}$ a fixed point in the euclidean space.

Consider the forces $\mathbf{s}$ and $\mathbf{b}$ for a body during a motion. Cauchy's Theorem states that a necessary and sufficient condition for the momentum laws to be satisfied is that there exists a second-order tensor field $\mathbf{T}$ called the Cauchy stress tensor, such that

(a) for each $\mathbf{n}$

$$\mathbf{s}(\mathbf{n}, \mathbf{x}, t) = \mathbf{T}(\mathbf{x}, t)\, \mathbf{n} \tag{3.31}$$

(b) $\mathbf{T}$ is symmetric

(c) $\mathbf{T}$ satisfies the equation of motion

$$\mathrm{div}\mathbf{T} + \mathbf{b} = \rho\dot{\mathbf{v}}. \tag{3.32}$$

The Cauchy stress tensor $\mathbf{T}$ is a measure of contact forces per unit of area in the current configuration, which in general, specially for problems concerning solids, is not known a priori. Therefore, we introduce a measure of contact force in the reference configuration, the Piola-Kirchhoff stress tensor $\mathbf{P}$, given by

$$\mathbf{P}(\mathbf{x}, t) \coloneqq \mathbf{T}(\mathbf{f}(\mathbf{X}, t), t)\, \mathrm{cof}\, \mathbf{F}(\mathbf{X}, t), \tag{3.33}$$

where

$$\mathrm{cof}\, \mathbf{F} \coloneqq (\det \mathbf{F})\, \mathbf{F}^{-T} \tag{3.34}$$

denotes the cofactor of $\mathbf{F}$. Again, omitting the dependence of the material point $\mathbf{X}$ and the time t, we may now express the balance laws (3.29) and (3.30) in the reference configuration as

$$\int_{\partial\mathcal{P}} \mathbf{P}\, \mathbf{n}\, dA + \int_{\mathcal{P}} \mathbf{b}_0\, dV = \int_{\mathcal{P}} \ddot{\mathbf{x}}\rho_0\, dV, \tag{3.35}$$

$$\int_{\partial\mathcal{P}} \mathbf{r}_0 \times \mathbf{P}\, \mathbf{n}\, dA + \int_{\mathcal{P}} \mathbf{r}_0 \times \mathbf{b}_0\, dV = \int_{\mathcal{P}} \mathbf{r}_0 \times \ddot{\mathbf{x}}\rho_0\, dV, \tag{3.36}$$

respectively, where $\mathbf{r}_0 \coloneqq \mathbf{f} - \mathbf{o}$, $\mathbf{b}_0 \coloneqq (\det \mathbf{F})\, \mathbf{b} \circ \mathbf{f}$, and $\rho_0 \coloneqq (\det \mathbf{F})\, \rho \circ \mathbf{f}$. The equation of motion (3.32) in the reference configuration becomes

$$\mathrm{Div}\mathbf{P} + \mathbf{b}_0 = \rho_0 \ddot{\mathbf{x}}, \tag{3.37}$$

where $\mathrm{Div}(\cdot)$ denotes the divergence with respect to $\mathbf{X}$.

Note from both (3.33) and (3.34) that, in general, the Piola-Kirchhoff stress tensor $\mathbf{P}$ is not symmetric. However, it satisfies the relation

$$\mathbf{P}\,\mathbf{F}^T = \mathbf{F}\,\mathbf{P}^T. \tag{3.38}$$

3.3 Constitutive assumptions

3.3.1 Types of constitutive assumptions

The mass conservation equation (3.25) and the equation of motion (3.32) are not enough to fully characterize the motion of a body. In fact, they constitute 4 scalar equations for 10 scalar variables, which are the mass density ρ, three components of the position vector $\mathbf{x}$, and six components from the Cauchy stress tensor $\mathbf{T}$. In addition, equations (3.25) and (3.32) do not distinguish between different types of material; for instance, it does not distinguish between liquid and solid or rubber and steel.

Here, we list three types of constitutive assumptions.

(a) Constitutive relation between the stress and the motion. It provides the missing six equations needed for the mathematical system. It is a mathematical representation of the body response to stimuli from the environment;

(b) Constraints on the possible deformations the body may undergo. For instance, one may impose incompressibility, in which case deformations must satisfy $\det \mathbf{F} = 1$;

(c) Assumptions on the form of the stress tensor. This type of assumption is usually found when one considers the stress to be a pressure, which is a common assumption found in the study of fluid and gases. It will not be discussed in this work, since we consider only solids.

3.3.2 Constitutive relation for an elastic body

An elastic body has the property of recovering its initial size and shape when the forces causing the deformation are removed. A classical example is an elastic spring under traction. The applied force depends only on the change in length of the spring and is independent of the rate of change at which the force is being applied or the past lengths. Broadly stated, an elastic material is defined as a material whose stress at place $\mathbf{x}$ and

time t is determined solely by the deformation gradient at the corresponding point in the reference configuration, i.e., the constitutive relation can be written as

$$\mathbf{T}(\mathbf{x}, t) = \hat{\mathbf{T}}(\mathbf{F}(\mathbf{X}, t), \mathbf{X}), \tag{3.39}$$

where $\hat{\mathbf{T}}$ is the response function for the Cauchy stress. In addition, since $\mathbf{P} \coloneqq \mathbf{T}\,\mathrm{cof}\,\mathbf{F}$, one may also express the Piola-Kirchhoff stress tensor solely in terms of the deformation gradient $\mathbf{F}$. i.e.,

$$\mathbf{P}(\mathbf{X}, t) = \hat{\mathbf{P}}(\mathbf{F}(\mathbf{X}, t), \mathbf{X}), \tag{3.40}$$

where $\hat{\mathbf{P}}$ is the response function for the Piola-Kirchhoff stress.

3.3.3 Stress state on internally constrained bodies

Some problems in the real world may be more properly represented when the deformation is subject to some kind of local internal constraint. For instance, the material may be considered incompressible or inextensible in a given direction.

Internal constraints can be represented by a scalar equation of the form

$$c(\mathbf{F}) = 0, \tag{3.41}$$

where c is a scalar function. The constraint axiom (GURTIN, 1981, p. 118) states that the stress is determined by the motion only within a stress $\mathbf{T}_c$ that does no work in any motion consistent with the constraint (3.41). Therefore,

$$\mathbf{T} = \hat{\mathbf{T}}(\mathbf{F}) + \mathbf{T}_c, \qquad \mathbf{T}_c \in \mathscr{R}, \tag{3.42}$$

where $\mathscr{R}$ is the reaction space defined by

$$\mathscr{R} \coloneqq \{\mathbf{T}_c \in \mathrm{Sym} \mid \mathbf{T}_c \cdot \mathbf{D} = 0 \quad \forall\, \mathbf{D} \in \mathscr{D}\}. \tag{3.43}$$

In (3.43), the stretching $\mathbf{D}$ is the symmetric part of

$$\mathbf{L} \coloneqq \mathrm{grad}\,\mathbf{v} = \dot{\mathbf{F}}\,\mathbf{F}^{-1}, \tag{3.44}$$

with grad denoting the gradient with respect to $\mathbf{x}$, and $\mathscr{D}$ is the set of all stretching tensors $\mathbf{D}$ that are consistent with the constraint (3.41).

3.4 Variational principles

3.4.1 Strong formulation

From now on, we consider only elastostatic problems, for which $\ddot{\mathbf{x}} = \mathbf{0}$ in (3.37). The resulting expression is the well known equilibrium equation in the reference configuration.

Consider that the boundary $\partial\mathcal{B}$ of the reference configuration $\mathcal{B}$ is composed of two non-intersecting parts, $\partial_1\mathcal{B}$ and $\partial_2\mathcal{B}$, $\partial\mathcal{B} = \partial_1\mathcal{B} \cup \partial_2\mathcal{B}$, $\partial_1\mathcal{B} \cap \partial_2\mathcal{B} = \emptyset$, such that

$\mathbf{x} \coloneqq \mathbf{f}(\mathbf{X}) = \overline{\mathbf{f}}(\mathbf{X})$ in $\mathbf{X} \in \partial_1\mathcal{B}$, where $\overline{\mathbf{f}}$ is a known function, and a dead load traction field $\overline{\mathbf{t}}(\mathbf{X})$ is prescribed for $\mathbf{X} \in \partial_2\mathcal{B}$. From the equation of motion in the reference configuration (3.37), the response function (3.40) and the above boundary conditions, one has the following boundary value problem for $\mathbf{f}(\mathbf{X})$

$$\begin{cases} \operatorname{Div} \hat{\mathbf{P}}(\mathbf{F}(\mathbf{X})) + \mathbf{b}_0(\mathbf{X}) = \mathbf{0}, & \mathbf{X} \in \mathcal{B}, \\ \mathbf{f}(\mathbf{X}) = \overline{\mathbf{f}}(\mathbf{X}), & \mathbf{X} \in \partial_1\mathcal{B}, \\ \hat{\mathbf{P}}(\mathbf{F}(\mathbf{X}))\,\mathbf{n} = \overline{\mathbf{t}}(\mathbf{X}), & \mathbf{X} \in \partial_2\mathcal{B}, \end{cases} \tag{3.45}$$

where we recall from Section 3.1.1 that $\mathbf{F}(\mathbf{X}) \coloneqq \nabla\mathbf{f}(\mathbf{X})$, and $\mathbf{n}$ is a unit normal to $\partial_2\mathcal{B}$. The expressions in (3.45) comprise the strong form of the associated boundary value problem, which must hold at every material point $\mathbf{X}$.

3.4.2 Hyperelastic material

An elastic material is hyperelastic or Green elastic material if there exists a scalar function $\hat{W}(\mathbf{F}, \mathbf{X})$, called the strain energy density function, so that the Piola-Kirchhoff stress tensor is given by

$$\mathbf{P} = \frac{\partial \hat{W}}{\partial \mathbf{F}}(\mathbf{X}, \mathbf{F}). \tag{3.46}$$

Using the fixed orthonormal basis $\{\mathbf{e}_1, \mathbf{e}_2, \mathbf{e}_3\}$, the components of $\mathbf{P}$ and $\mathbf{F}$ are given by, respectively, $P_{ij} = \mathbf{e}_i \cdot \mathbf{P}\,\mathbf{e}_j$, $F_{ij} = \mathbf{e}_i \cdot \mathbf{F}\,\mathbf{e}_j$, and we can write the components of (3.46) as

$$P_{ij} = \frac{\partial \hat{W}}{\partial F_{ij}}(\mathbf{X}, \mathbf{F}). \tag{3.47}$$

3.4.3 Principle of stationary potential energy

The total potential energy functional or, simply, total energy of the hyperelastic body is given by (CIARLET, 1988, p. 137)

$$\mathcal{E}[\mathbf{f}] = \int_{\mathcal{B}} \hat{W}(\mathbf{X}, \mathbf{F})\, dV - \int_{\mathcal{B}} \mathbf{b}_0 \cdot \mathbf{f}\, dV - \int_{\partial_2\mathcal{B}} \overline{\mathbf{t}} \cdot \mathbf{f}\, dA, \tag{3.48}$$

and its first variation by (CIARLET, 1988, p. 143)

$$\partial\mathcal{E} = \int_{\mathcal{B}} \mathbf{P} \cdot \nabla\mathbf{v}\, dV - \int_{\mathcal{B}} \mathbf{b}_0 \cdot \mathbf{v}\, dV - \int_{\partial_2\mathcal{B}} \overline{\mathbf{t}} \cdot \mathbf{v}\, dA \tag{3.49}$$

for an arbitrary vector field $\mathbf{v} : \mathcal{B} \to \mathbb{R}^3$, where we recall from Section 3.1.1 that $\mathbf{F} \coloneqq \nabla\,\mathbf{f}$, from Section 3.2.3 that $\mathbf{b}_0$ is the body force in the reference configuration, and from Section 3.4.1 that $\overline{\mathbf{t}}$ is a dead load traction field prescribed on $\partial_2\mathcal{B}$.

The principle of stationary potential energy states that the deformation $\mathbf{f}$ is a solution of the boundary value problem (3.45) if and only if the first variation $\partial\mathcal{E}$, given by (3.49), vanishes for all variations $\mathbf{v}$ such that $\mathbf{v} = \mathbf{0}$ on $\partial_1\mathcal{B}$.

The deformation $\mathbf{f}$ renders $\mathcal{E}$ stationary in the considered class of kinematically admissible deformations. In particular, the minimum of the total energy is a stationary function. In variational calculus, the boundary value problem (3.45) constitutes the Euler-Lagrange equations associated with the total energy $\mathcal{E}$. In other words, any minimizer $\mathbf{f}$ of $\mathcal{E}$, that belongs to the set of admissible solutions, is a solution of the boundary value problem (3.45).

For convenience, all the above considerations may be expressed in terms of the displacement field $\mathbf{u}(\mathbf{X}) \coloneqq \mathbf{f}(\mathbf{X}) - \mathbf{X}$, instead of the deformation $\mathbf{f}(\mathbf{X})$.

3.5 Linear elasticity

3.5.1 Elasticity tensor

The elasticity tensor, denoted by $\mathbb{C}$, is defined as

$$\mathbb{C}(\mathbf{X}) \coloneqq \left(\frac{\partial \hat{\mathbf{P}}}{\partial \mathbf{F}}(\mathbf{X}, \mathbf{F}) \right) \Bigg|_{\mathbf{F}=\mathbf{1}} \tag{3.50}$$

or, in Cartesian components,

$$C_{ijkl} = \left(\frac{\partial \hat{P}_{ij}}{\partial F_{kl}}(\mathbf{X}, \mathbf{F}) \right) \Bigg|_{\mathbf{F}=\mathbf{1}}. \tag{3.51}$$

This fourth-order tensor defines a linear transformation $\mathbb{C} : \mathrm{Lin} \to \mathrm{Lin}$, where Lin denotes the set of all second-order tensors, and plays an important role in the analysis of the constitutive response of materials in the vicinity of the reference configuration, for which $\mathbf{F} = \mathbf{1}$ or $\mathbf{f}(\mathbf{X}) = \mathbf{X}$. In this work, we consider that the residual stress vanishes, which means that

$$\hat{\mathbf{P}}(\mathbf{F}) = \hat{\mathbf{T}}(\mathbf{F}) = \mathbf{0} \qquad \text{for } \mathbf{F} = \mathbf{1}. \tag{3.52}$$

It is then possible to show (GURTIN, 1981, p. 194) that

$$\mathbb{C}(\mathbf{X}) = \left(\frac{\partial \hat{\mathbf{T}}}{\partial \mathbf{F}}(\mathbf{X}, \mathbf{F}) \right) \Bigg|_{\mathbf{F}=\mathbf{1}}. \tag{3.53}$$

The elasticity tensor $\mathbb{C}$ has the following properties

(a) $\mathbb{C}[\mathbf{A}] \in \mathrm{Sym}, \ \forall\, \mathbf{A} \in \mathrm{Lin}$

(b) $\mathbb{C}[\mathbf{W}] = \mathbf{0}, \ \forall\, \mathbf{W} \in \mathrm{Skw}$

where Sym and Skw denote the set of all symmetric and anti-symmetric second-order tensors, respectively.

As a result of the above properties, first, consider the decomposition of the displacement gradient into its symmetric and anti-symmetric parts, i.e., $\nabla \mathbf{u} = \mathbf{E} + \mathbf{W}$, where

$\mathbf{E}$ is the infinitesimal strain tensor defined by (3.13) and $\mathbf{W} = (\nabla\mathbf{u} - \nabla\mathbf{u}^T)/2$. Then, from the linearity of $\mathbb{C}$ and the property (b), one has

$$\mathbb{C}[\nabla\mathbf{u}] = \mathbb{C}[\mathbf{E}]. \tag{3.54}$$

In addition, we say that the elasticity tensor $\mathbb{C}$ is positive definite if

$$\mathbf{A} \cdot \mathbb{C}[\mathbf{A}] > 0 \qquad \text{for all symmetric tensors } \mathbf{A} \neq \mathbf{0}. \tag{3.55}$$

3.5.2 Constitutive and equilibrium equations

A fundamental assumption in linear elasticity is that the displacement gradient $\nabla\mathbf{u}$ is infinitesimal. It then follows from the constitutive relation (3.40), the relation (3.11), the definition (3.50), and the property (3.54) that

$$\begin{aligned}\mathbf{P} = \hat{\mathbf{P}}(\mathbf{F}) = \hat{\mathbf{P}}(\mathbf{1} + \nabla\mathbf{u}) &= \hat{\mathbf{P}}(\mathbf{1}) + \left(\frac{\partial\hat{\mathbf{P}}}{\partial\mathbf{F}}(\mathbf{X},\mathbf{F})\right)\Big|_{\mathbf{F}=\mathbf{1}}[\nabla\mathbf{u}] + o(\nabla\mathbf{u}) \\ &= \hat{\mathbf{P}}(\mathbf{1}) + \mathbb{C}[\nabla\mathbf{u}] + o(\nabla\mathbf{u}) \\ &= \hat{\mathbf{P}}(\mathbf{1}) + \mathbb{C}[\mathbf{E}] + o(\nabla\mathbf{u}).\end{aligned} \tag{3.56}$$

Assuming that the residual stress vanishes, i.e., the relation (3.52) holds, the last equation in (3.56) becomes

$$\mathbf{P} = \mathbb{C}[\mathbf{E}] + o(\nabla\mathbf{u}). \tag{3.57}$$

Thus, the Piola-Kirchhoff stress $\mathbf{P}$ is symmetric and linear with respect to the infinitesimal strain tensor $\mathbf{E}$ to within an error of $o(\nabla\mathbf{u})$. In addition, from (3.53), the above steps can be repeated taking $\mathbf{T}$ and $\hat{\mathbf{T}}$ in the place of $\mathbf{P}$ and $\hat{\mathbf{P}}$, respectively, yielding

$$\mathbf{T} = \mathbb{C}[\mathbf{E}] + o(\nabla\mathbf{u}). \tag{3.58}$$

Comparing equations (3.57) and (3.58), one has

$$\mathbf{P} = \mathbf{T} + o(\nabla\mathbf{u}). \tag{3.59}$$

Therefore, to within an error of $o(\nabla\mathbf{u})$, the stress tensors $\mathbf{P}$ and $\mathbf{T}$ are equal.

Thus, within an error of order $o(\nabla\mathbf{u})$ it follows from (3.13), (3.37) and (3.59) that the basic equations of classical linear elasticity for static problems are given by

$$\begin{cases}\mathbf{P} = \mathbf{T} = \mathbb{C}[\mathbf{E}], \\ \mathbf{E} = (\nabla\mathbf{u} + \nabla\mathbf{u}^T)/2, \\ \mathrm{Div}\mathbf{P} + \mathbf{b}_0 = \mathbf{0}\end{cases} \tag{3.60}$$

which are, respectively, the generalized Hooke's law, the infinitesimal strain tensor and the linearized equation of equilibrium.

3.5.3 Principle of minimum potential energy

We recall the boundary value problem from Section 3.4.1, but, here, in the context of the classical linear elasticity.

Let $\mathcal{B} \subset \mathbb{R}^n$, $n = 2$ or 3, be the undistorted natural reference configuration of the body. Points $\mathbf{X} \in \mathcal{B}$ are mapped to points $\mathbf{x} \coloneqq \mathbf{f}(\mathbf{X}) = \mathbf{X} + \mathbf{u}(\mathbf{X})$, $\mathbf{x} \in \mathbb{R}^n$, where $\mathbf{u}(\mathbf{X})$ is the displacement of $\mathbf{X}$. The boundary $\partial\mathcal{B}$ of $\mathcal{B}$ is composed of two non-intersecting parts, $\partial_1\mathcal{B}$ and $\partial_2\mathcal{B}$, $\partial\mathcal{B} = \partial_1\mathcal{B} \cup \partial_2\mathcal{B}$, $\partial_1\mathcal{B} \cap \partial_2\mathcal{B} = \emptyset$ such that $\mathbf{u}(\mathbf{X}) = \bar{\mathbf{u}}(\mathbf{X})$ for $\mathbf{X} \in \partial_1\mathcal{B}$, where $\bar{\mathbf{u}}$ is a given function, and a dead load traction field $\bar{\mathbf{t}}(\mathbf{X})$ is prescribed for $\mathbf{X} \in \partial_2\mathcal{B}$. In addition, a body force $\mathbf{b}_0(\mathbf{X})$ per unit of volume acts in $\mathbf{X} \in \mathcal{B}$.

Assuming that the elasticity tensor $\mathbb{C}$ is positive definite in the sense of (3.55), it is possible to show (GURTIN, 1981, p. 207) that the displacement field $\mathbf{u}$ that satisfies the basic equations of classical linear elasticity (3.60) together with the above boundary conditions is unique. In addition, according to the Principle of Minimum Potential Energy (GURTIN, 1981, p. 208), this displacement field corresponds to an absolute minimum of the potential energy functional, which, in the context of linear elasticity, is given by

$$\mathcal{E}[\mathbf{u}] = \frac{1}{2}\int_{\mathcal{B}} \mathbb{C}[\mathbf{E}] \cdot \mathbf{E}\, dV - \int_{\mathcal{B}} \mathbf{b}_0 \cdot \mathbf{u}\, dV - \int_{\partial_2\mathcal{B}} \bar{\mathbf{t}} \cdot \mathbf{u}\, dA. \tag{3.61}$$

3.6 Linear elasticity with local injectivity constraint

3.6.1 Constrained minimization problem

The basic equations of linear elasticity in (3.60) or the Principle of Minimum Potential Energy do not guarantee that the solution satisfies the local injectivity constraint (3.6). In fact, there are solutions that violate this constraint, leading to material overlapping, which is not a physically realistic behavior. Nevertheless, these solutions are still employed in engineering applications.

To search for a solution that prevent this unrealistic behavior, Fosdick and Royer-Carfagni (2001) proposed a constrained minimization theory, which consists of minimizing the classical potential energy functional (3.61) subject to the constraint of local injectivity (3.6). In particular, the determinant of the deformation gradient must be greater than an arbitrary small positive parameter ε.

Consider the region $\mathcal{B}$ and the boundary conditions described in Section 3.5.3, the associated constrained minimization problem is given by

$$\min_{\mathbf{u} \in \mathcal{A}_\varepsilon} \mathcal{E}[\mathbf{u}], \tag{3.62}$$

where we recall from (3.61) that $\mathcal{E}[\mathbf{u}]$ is the classical potential energy functional of linear elasticity theory and

$$\mathcal{A}_\varepsilon \coloneqq \left\{ \mathbf{u} \in \mathcal{W}^{1,2}(\mathcal{B}) \to \mathbb{R}^n \mid \det(\mathbf{1} + \nabla\mathbf{u}) \geq \varepsilon > 0,\ \mathbf{u} = \bar{\mathbf{u}} \text{ on } \partial_1\mathcal{B} \right\} \tag{3.63}$$

is the set of admissible displacement fields, with ε being a sufficiently small positive scalar. In (3.61), $\mathbf{E}$ is the infinitesimal strain tensor given by (3.60b) and $\mathbb{C} = \mathbb{C}(\mathbf{X})$ is the elasticity tensor that appears in (3.60a), which is symmetric and positive definite. If the injectivity constraint $\det(\mathbf{1} + \nabla\mathbf{u}) \geq \varepsilon > 0$ were not present, the minimization problem would become a classical problem of linear elasticity theory.

3.6.2 Euler-Lagrange equations

Let $\mathbf{u}^*$ be the minimizer of the constrained problem defined by (3.62) - (3.63). We then have that $\mathbf{f}^*$, $\mathbf{E}^*$ and $\mathbf{T}^*$ are the associated deformation, strain and stress fields, respectively, and are given by

$$\mathbf{f}^*(\mathbf{X}) \coloneqq \mathbf{X} + \mathbf{u}^*(\mathbf{X}), \qquad \mathbf{E}^* \coloneqq \frac{1}{2}(\nabla\mathbf{u}^* + (\nabla\mathbf{u}^*)^T), \qquad \mathbf{T}^* \coloneqq \mathbb{C}[\mathbf{E}^*]. \tag{3.64}$$

In addition, let $\mathcal{B}$ be divided in two open subregions $\mathcal{B}_>$ and $\mathcal{B}_=$, such that $\mathcal{B} = \mathcal{B}_> \cup \mathcal{B}_= \cup \Sigma$ and $\mathcal{B}_> \cap \mathcal{B}_= = \emptyset$, where Σ is the interface between $\mathcal{B}_>$ and $\mathcal{B}_=$. The subregions $\mathcal{B}_>$ and $\mathcal{B}_=$ are defined by

$$\mathcal{B}_> \coloneqq \text{int}[\{\mathbf{X} \in \mathcal{B} \mid \det\nabla\mathbf{f}^*(\mathbf{X}) > \varepsilon\}], \qquad \mathcal{B}_= \coloneqq \text{int}[\{\mathbf{X} \in \mathcal{B} \mid \det\nabla\mathbf{f}^*(\mathbf{X}) = \varepsilon\}], \tag{3.65}$$

where int$[\cdot]$ denotes the interior of a set.

Fosdick and Royer-Carfagni (2001) show that the Euler-Lagrange equations for the constrained minimization problem (3.62), i.e., the necessary conditions for the existence of a minimizer $\mathbf{u}^*$, are given by

$$\text{Div}\,\mathbf{T}^* + \mathbf{b}_0 = \mathbf{0} \quad \text{in } \mathcal{B}_>\,, \qquad \text{Div}\,(\mathbf{T}^* - \varepsilon\lambda^*(\nabla\mathbf{f}^*)^{-T}) + \mathbf{b}_0 = \mathbf{0} \quad \text{in } \mathcal{B}_=\,, \tag{3.66}$$

where $\lambda^*(\mathbf{X}) \geq 0$ is the Lagrange multiplier field associated with the injectivity constraint $\det(\mathbf{1} + \nabla\mathbf{u}^*) \geq \varepsilon > 0$. The boundary conditions are given by

$$\mathbf{T}^*\,\mathbf{n} = \bar{\mathbf{t}} \quad \text{in } \partial_2\mathcal{B}_>\,, \qquad (\mathbf{T}^* - \varepsilon\lambda^*(\nabla\mathbf{f}^*)^{-T})\,\mathbf{n} = \bar{\mathbf{t}} \quad \text{in } \partial_2\mathcal{B}_=\,, \tag{3.67}$$

where $\mathbf{n}$ is a unit normal to $\partial_2\mathcal{B}$. In addition, the jump condition

$$(\mathbf{T}^* - \varepsilon\lambda^*(\nabla\mathbf{f}^*)^{-T})|_{\Sigma\cap\bar{\mathcal{B}}_=}\,\mathbf{n} = \mathbf{T}^*|_{\Sigma\cap\bar{\mathcal{B}}_>}\,\mathbf{n} \tag{3.68}$$

must hold across $\Sigma \coloneqq \bar{\mathcal{B}}_> \cap \bar{\mathcal{B}}_=$, where $\mathbf{n}$ is a unit normal to Σ and where $\Sigma \cap \bar{\mathcal{B}}_=$ and $\Sigma \cap \bar{\mathcal{B}}_>$ mean that the evaluations are understood as limits to the dividing interface Σ from within $\mathcal{B}_=$ and $\mathcal{B}_>$, respectively.

4 NUMERICAL PROCEDURE

In this chapter we describe the numerical procedure used to search for a minimizer of the constrained minimization problem (3.62) - (3.63). For this, we present an interior penalty formulation, which was introduced by Aguiar (2006), followed by a finite element formulation that yields a discrete objective function to be minimized by standard nonlinear programming techniques. This numerical procedure is implemented in a C++ code based on the open source package deal.II (ARNDT et al., 2019).

4.1 Interior penalty formulation

In the interior penalty method, we determine an approximate solution for the constrained minimization problem (3.62) by solving a sequence of minimization problems that, albeit still constrained, allow the use of techniques commonly employed in the investigation of unconstrained minimization problems. For that, we replace the original functional to be minimized, given by $\mathcal{E}[\mathbf{u}]$ in (3.61) with $\mathbf{u}$ belonging to the set $\mathcal{A}_\varepsilon$ in (3.63), by the penalized functional $\mathcal{E}_\delta : \mathcal{A}_\varepsilon \to \mathbb{R}$ defined by

$$\mathcal{E}_\delta[\mathbf{u}] \coloneqq \mathcal{E}[\mathbf{u}] + \frac{1}{\delta}\mathcal{P}[\mathbf{u}]. \tag{4.1}$$

In expression (4.1), $\delta > 0$ is a penalty parameter and $\mathcal{P}[\mathbf{u}]$ is a barrier functional, which must satisfy $\mathcal{P}[\mathbf{u}] > 0 \; \forall \, \mathbf{u} \in \mathcal{A}_\varepsilon$ and $\mathcal{P}[\mathbf{u}] \to \infty$ as $\mathbf{u} \to \partial\mathcal{A}_\varepsilon$, where $\partial\mathcal{A}_\varepsilon$ stands for the boundary of the set $\mathcal{A}_\varepsilon$. The addition of the term $\mathcal{P}/\delta$ establishes a barrier on the boundary of the constraint set $\mathcal{A}_\varepsilon$ that prevents the minimizing procedure from leaving the set $\mathcal{A}_\varepsilon$. To determine the minimizer of (3.62), we solve a sequence of minimization problems of the form

$$\min_{\mathbf{u}\in\mathcal{A}_\varepsilon} \mathcal{E}_\delta[\mathbf{u}], \tag{4.2}$$

where we must take increasingly higher values for δ. Let $\mathbf{u}_\delta^*$ denote a minimizer of (4.2). We expect that, in the limit as $\delta \to \infty$, the sequence $\{\mathbf{u}_\delta^*\}$ yields a limit function that is a solution of the original constrained minimization problem (3.62). In this work, we consider the same barrier functional proposed by Aguiar (2006) and used by Fosdick, Freddi and Royer-Carfagni (2008), which is given by

$$\mathcal{P}[\mathbf{u}] \coloneqq \int_{\mathcal{B}} \frac{1}{\det(\mathbf{1} + \nabla\mathbf{u}) - \varepsilon} \, d\mathbf{X}, \qquad \forall \mathbf{u} \in \mathcal{A}_\varepsilon. \tag{4.3}$$

Similarly, we expect that the Lagrange multiplier λ^* that appears in the expressions (3.66) - (3.68) is the limit function of the sequence $\{\lambda_\delta\}$, where, according to Aguiar (2006),

$$\lambda_\delta = \frac{1}{\delta\,(\det(\mathbf{1} + \nabla\mathbf{u}) - \varepsilon)^2}. \tag{4.4}$$

4.2 Discrete formulation

We consider a Finite Element formulation of the minimization problem

$$\min_{\mathbf{u}\in\mathcal{A}_\varepsilon} \mathcal{E}_\delta[\mathbf{u}], \tag{4.5}$$

where $\mathcal{E}_\delta[\mathbf{u}]$ is given by (4.1). Therefore, we search for minimizers $\mathbf{u}_h$ in a finite dimensional subspace $\mathcal{V}_h$ spanned by a set of basis functions $\{\mathbf{w}_i\}$, where h stands for the characteristic length of the finite element. Since $\mathbf{u}_h \in \mathcal{V}_h$, we write

$$\mathbf{u}_h = \sum_{i=1}^{m} s^i \, \mathbf{w}_i, \tag{4.6}$$

where $s^i \in \mathbb{R}, i = 1, 2, ..., m$ is a degree of freedom and m is the total number of degrees of freedom associated with the discretization.

In this work, as we will see in the next chapters, we use meshes composed of linear and bi-linear finite elements for the 1D and 2D cases, respectively. Thus, at each mesh node $\mathbf{X}_j$, $j = 1, 2, ..., M$, we associate a degree of freedom s^i for each component of the displacement field $\mathbf{u} = u_r \, \mathbf{e}_r + u_\theta \, \mathbf{e}_\theta$, where $(\mathbf{e}_r, \mathbf{e}_\theta)$ is the polar orthonormal basis. In Chapter 5, the displacement field has only the radial component, therefore, $s^j = u_r(\mathbf{X}_j)$ and $m = M$. In Chapter 6, the displacement field has both radial and tangential components, therefore, we adopt $s^{2j-1} = u_r(\mathbf{X}_j)$ and $s^{2j} = u_\theta(\mathbf{X}_j)$, which yield $m = 2M$. In Chapter 6, there is also a case where the displacement field is represented in terms of the Cartesian orthonormal basis $(\mathbf{e}_1, \mathbf{e}_2)$. In this case, we still have $m = 2M$, but $s^{2j-1} = u_1(\mathbf{X}_j)$ and $s^{2j} = u_2(\mathbf{X}_j)$, where $u_1 \coloneqq \mathbf{u} \cdot \mathbf{e}_1$ and $u_2 \coloneqq \mathbf{u} \cdot \mathbf{e}_2$.

Let us introduce the vector $\mathbf{s} \coloneqq (s^1, s^2, ..., s^m)$ and the functions $\mathcal{E}_h(\mathbf{s}) \coloneqq \mathcal{E}[\mathbf{u}_h]$ and $\mathcal{P}_h(\mathbf{s}) \coloneqq \mathcal{P}[\mathbf{u}_h]$. Then, the discrete version of the penalized potential (4.1) is defined by

$$\mathcal{F}_\delta(\mathbf{s}) \coloneqq \mathcal{E}_h(\mathbf{s}) + \frac{1}{\delta}\mathcal{P}_h(\mathbf{s}) \tag{4.7}$$

and the associated discrete minimization problem is given by

$$\min_{\mathbf{s}\in\mathbb{R}^m} \mathcal{F}_\delta(\mathbf{s}) \tag{4.8}$$

subject to $\det(\mathbf{1} + \nabla\mathbf{u}_h) \geq \varepsilon > 0$ in parts of the domain where $\mathbf{u}_h$, given by (4.6), is smooth. This minimization problem is solved iteratively by a standard unconstrained minimization method. Below, we briefly discuss this method, which was proposed by Aguiar (2006). Besides, we evaluate definite integrals by using a Gauss-Legendre quadrature rule with three quadrature points in each mesh space direction, which corresponds to three and nine quadrature points in each finite element of the 1D and 2D meshes, respectively.

Starting from an initial guess $\mathbf{s}_0$, which is assumed to be sufficiently close to the minimizer of (4.8), we generate a sequence of solutions $\mathbf{s}_k$, $k = 0, 1, 2, ...$, using the recursive formula

$$\mathbf{s}_{k+1} = \mathbf{s}_k + \alpha_k \mathbf{d}_k, \tag{4.9}$$

where $\alpha_k \in \mathbb{R}$ is a step length and $\mathbf{d}_k$ is a search direction. Each iteration k consists of determining the search direction $\mathbf{d}_k$ followed by a line search that minimizes $\mathcal{F}_\delta$ along the line $\mathbf{s}_k + \alpha\mathbf{d}_k, \alpha \in \mathbb{R}$.

To determine the search direction $\mathbf{d}_k$, we consider that, in the vicinity of $\mathbf{s}_k$, the potential $\mathcal{F}_\delta(\mathbf{s})$ may be approximated by the quadratic form

$$\mathcal{F}_\delta(\mathbf{s}) \approx \mathcal{Q}_m(\mathbf{s}) \coloneqq \mathcal{F}_\delta(\mathbf{s}_k) + \nabla_{\mathbf{s}}\mathcal{F}_\delta(\mathbf{s}_k) \cdot (\mathbf{s} - \mathbf{s}_k) + \frac{1}{2}(\mathbf{s} - \mathbf{s}_k) \cdot \nabla^2_{\mathbf{s}}\mathcal{F}_\delta(\mathbf{s}_k)(\mathbf{s} - \mathbf{s}_k), \quad (4.10)$$

where $\nabla_{\mathbf{s}}\mathcal{F}_\delta \coloneqq (\partial\mathcal{F}_\delta/\partial s^1, \partial\mathcal{F}_\delta/\partial s^2, ..., \partial\mathcal{F}_\delta/\partial s^m)$ is the gradient of $\mathcal{F}_\delta$ and $\nabla^2_{\mathbf{s}}\mathcal{F}_\delta$ is the Hessian of $\mathcal{F}_\delta$. By solving the vector equation $\nabla_{\mathbf{s}}\mathcal{Q}_m(\mathbf{s}) = \mathbf{0}$, which is a necessary condition for the existence of a minimizer $\hat{\mathbf{s}}$ of the quadratic form $\mathcal{Q}_m$, we obtain

$$\mathbf{d}_k \coloneqq \hat{\mathbf{s}} - \mathbf{s}_k = -\left(\nabla^2_{\mathbf{s}}\mathcal{F}_\delta(\mathbf{s})\right)^{-1} \nabla_{\mathbf{s}}\mathcal{F}_\delta(\mathbf{s}). \quad (4.11)$$

If we replace $\hat{\mathbf{s}}$ in (4.11) by $\mathbf{s}_{k+1}$, we would have the standard Newton's method. Instead, in this work $\mathbf{s}_{k+1}$ is given by (4.9), where $\mathbf{d}_k$ is given by the second term of (4.11) and the scalar α_k in (4.9) minimizes the objective function $\mathcal{F}_\delta(\mathbf{s}_k + \alpha\,\mathbf{d}_k)$ along the direction $\mathbf{d}_k$.

Let $\mathbf{u}_h^k$ denote the discrete displacement field associated with the vector $\mathbf{s}_k$ through (4.6). The stop criterium for the construction of a finite sequence of solutions $\mathbf{s}_k$ for a given δ is given by

$$||\mathbf{u}_h^{k+1} - \mathbf{u}_h^k||_{H_1} + \beta_\delta\,|\mathcal{F}_\delta(\mathbf{s}_{k+1}) - \mathcal{F}_\delta(\mathbf{s}_k)| < \varepsilon_{\mathbf{s}}, \quad (4.12)$$

where $\varepsilon_{\mathbf{s}} > 0$ is the adopted tolerance, $||\mathbf{u}_h^{k+1} - \mathbf{u}_h^k||_{H1}$ is the H_1-norm of $\mathbf{u}_h^{k+1} - \mathbf{u}_h^k$, which is given by

$$||\mathbf{u}_h^{k+1} - \mathbf{u}_h^k||_{H1} = \left[\int_{\mathcal{B}} (|\mathbf{u}_h^{k+1} - \mathbf{u}_h^k|^2 + |\nabla\mathbf{u}_h^{k+1} - \nabla\mathbf{u}_h^k|^2)\, d\mathbf{X}\right]^{\frac{1}{2}}, \quad (4.13)$$

and the factor β_δ is calculated once for each penalty parameter δ as

$$\beta_\delta = \frac{||\mathbf{u}_h^1 - \mathbf{u}_h^0||_{H1}}{|\mathcal{F}_\delta(\mathbf{s}_1) - \mathcal{F}_\delta(\mathbf{s}_0)|}. \quad (4.14)$$

The step length α_k is the solution of the nonlinear unidirectional minimization problem

$$\min_{\alpha\in\mathbb{R}} \mathcal{H}(\alpha) \coloneqq \min_{\alpha\in\mathbb{R}} \mathcal{F}_\delta(\mathbf{s}_k + \alpha\mathbf{d}_k) \quad (4.15)$$

subject to the constraint that $\det(\mathbf{1} + \nabla\mathbf{u}_h^k(\mathbf{X})) \geq \varepsilon$ at every point $\mathbf{X}$ where $\mathbf{u}_h^k$ is smooth. Starting from the initial guess $\alpha^{(0)} = 0$, we generate a sequence of step lengths $\alpha^{(i)}, i = 0, 1, 2, ...$, which is expected to converge to α_k as $i \to \infty$. We assume that $\mathcal{H}(\alpha)$ is, at least, twice differentiable for α close enough to $\alpha^{(i)}$, so that $\mathcal{H}(\alpha)$ may be approximated by the quadratic function

$$\mathcal{H}(\alpha) \approx \mathcal{Q}_1(\alpha) \coloneqq \mathcal{H}(\alpha^{(i)}) + \mathcal{H}'(\alpha^{(i)})(\alpha - \alpha^{(i)}) + \mathcal{H}''(\alpha^{(i)})\frac{(\alpha - \alpha^{(i)})^2}{2}, \quad (4.16)$$

where $(\cdot)'$ stands for $d(\cdot)/d\alpha$. The step length $\alpha^{(i+1)}$ is obtained by solving the equation $Q_1'(\alpha) = 0$, yielding

$$\alpha^{(i+1)} = \alpha^{(i)} - \frac{\mathcal{H}'(\alpha^{(i)})}{\mathcal{H}''(\alpha^{(i)})}. \tag{4.17}$$

For each $\alpha^{(i+1)}$ calculated from (4.17), we check if the local injectivity constraint for $\mathbf{s} = \mathbf{s}_k + \alpha^{(i+1)}\mathbf{d}_k$ is violated at the quadrature points. If it is violated, the step length $\alpha^{(i+1)}$ is halved until the constraint holds for all the quadrature points. This is the only place in the algorithm where we check for constraint violations. The stop criterium for the construction of a finite sequence of solutions $\alpha^{(i+1)}$ is given by

$$\frac{\mathbf{d}_k \cdot \nabla_{\mathbf{s}} \mathcal{F}(\mathbf{s}_k + \alpha^{(i+1)}\mathbf{d}_k)}{|\mathbf{d}_k|\,|\nabla_{\mathbf{s}} \mathcal{F}(\mathbf{s}_k + \alpha^{(i+1)}\mathbf{d}_k)|} < \varepsilon_\alpha \qquad \text{or} \qquad i+1 = N_\alpha, \tag{4.18}$$

where $\varepsilon_\alpha > 0$ is an adopted tolerance and N_α is the maximum number of iterations allowed. The inequality in (4.18a) states that the search direction $\mathbf{d}_k$ and the gradient of the objective function $\mathcal{F}_\delta$ must be orthogonal to each other to within an error ε_α.

In summary, starting from both an initial guess $\mathbf{s}_0$ and a penalty parameter δ and following the numerical procedure outlined above, we generate a sequence of approximations $\{\mathbf{s}_k\}$, which converges to a solution $\mathbf{s}_h^\delta$ of the discrete minimization problem (4.8). Next, we increase the penalty parameter δ and minimize again the corresponding functional $\mathcal{F}_\delta$. However, this time we take $\mathbf{s}_0$ to be the solution obtained from the previous δ. As the penalty parameter $\delta \to \infty$, the sequence of solutions $\{\mathbf{s}_h^\delta\}$ converges to a vector $\mathbf{s}_h = \{s^i\}$, $i = 1, 2, \ldots, m$, that yields the approximate solution $\mathbf{u}_h \in \mathcal{V}_h$, given by (4.6), of the original minimization problem (3.62). By letting $h \to 0$, we generate a sequence of approximations $\{\mathbf{u}_h\}$, which is expected to converge to the minimizer of the problem (3.62).

5 RADIALLY SYMMETRIC N-DIMENSIONAL SPHERE PROBLEM

In this chapter we consider the problem of an anisotropic n-dimensional solid sphere, $n = 2, 3$, subject to uniform normal pressure in the context of the constrained minimization theory. We assume that the solutions for both cases, $n = 2$ and $n = 3$, are radially symmetric and reproduce results found in the literature with the aim of validating the computational procedure.

5.1 Problem formulation

Consider the constrained minimization problem defined by (3.62) and (3.63). Here, let $\mathcal{B}$ be the natural undistorted reference configuration of an n-sphere of radius R_e, where $n = 2$ corresponds to a circular disk and $n = 3$ corresponds to an ordinary sphere. The n-sphere is in equilibrium with no body force and is subject to a uniform pressure $\bar{\mathbf{t}} = -p\,\mathbf{e}_r$ on its entire outer surface $\partial\mathcal{B}$. This pressure is a force per unit length in the case of $n = 2$ and a force per unit area in the case of $n = 3$. In addition, the displacement field is null at the center of the n-sphere.

For $n = 2$, the corresponding circular disk problem is two dimensional and the material is cylindrically anisotropic, with the elasticity tensor $\mathbb{C}$ being constant relative to the orthonormal cylindrical basis $(\mathbf{e}_r, \mathbf{e}_\theta)$ associated with the polar coordinate system (R, Θ) at any material point $\mathbf{X} \in \mathcal{B}$. Similarly, for $n = 3$, the corresponding ordinary sphere problem is three dimensional and the material is spherically anisotropic, with the elasticity tensor $\mathbb{C}$ being constant relative to the orthonormal spherical basis $(\mathbf{e}_r, \mathbf{e}_\theta, \mathbf{e}_\phi)$ associated with the spherical coordinate system (R, Θ, Φ) at any material point $\mathbf{X} \in \mathcal{B}$. In Voigt notation, the matrix representation of the elasticity tensor $\mathbb{C}$ is given by

$$\mathbf{C} = \begin{bmatrix} c_{11} & c_{12} & 0 \\ c_{12} & c_{22} & 0 \\ 0 & 0 & c_{66} \end{bmatrix} \tag{5.1}$$

for $n = 2$ and by

$$\mathbf{C} = \begin{bmatrix} c_{11} & c_{12} & c_{12} & 0 & 0 & 0 \\ c_{12} & c_{22} & c_{23} & 0 & 0 & 0 \\ c_{12} & c_{23} & c_{22} & 0 & 0 & 0 \\ 0 & 0 & 0 & c_{44} & c_{45} & c_{46} \\ 0 & 0 & 0 & c_{45} & c_{55} & c_{56} \\ 0 & 0 & 0 & c_{46} & c_{56} & c_{66} \end{bmatrix}, \tag{5.2}$$

for $n = 3$.

We now assume that the displacement field is radially symmetric, i.e.,

$$\mathbf{u}(R,\Theta) = u(R)\,\mathbf{e}_r \qquad \text{for } n=2 \tag{5.3}$$

and

$$\mathbf{u}(R,\Theta,\Phi) = u(R)\,\mathbf{e}_r \qquad \text{for } n=3. \tag{5.4}$$

We then have that the infinitesimal strain tensor is given by either

$$\mathbf{E} = \epsilon_{rr}\,\mathbf{e}_r\otimes\mathbf{e}_r + \epsilon_{\theta\theta}\,\mathbf{e}_\theta\otimes\mathbf{e}_\theta + \epsilon_{r\theta}\,(\mathbf{e}_r\otimes\mathbf{e}_\theta + \mathbf{e}_\theta\otimes\mathbf{e}_r) \qquad \text{for } n=2 \tag{5.5}$$

or by

$$\begin{aligned}\mathbf{E} =\,&\epsilon_{rr}\,\mathbf{e}_r\otimes\mathbf{e}_r + \epsilon_{\theta\theta}\,\mathbf{e}_\theta\otimes\mathbf{e}_\theta + \epsilon_{\phi\phi}\,\mathbf{e}_\phi\otimes\mathbf{e}_\phi + \epsilon_{r\theta}\,(\mathbf{e}_r\otimes\mathbf{e}_\theta + \mathbf{e}_\theta\otimes\mathbf{e}_r)\\ &+\,\epsilon_{r\phi}\,(\mathbf{e}_r\otimes\mathbf{e}_\phi + \mathbf{e}_\phi\otimes\mathbf{e}_r) + \epsilon_{\theta\phi}\,(\mathbf{e}_\theta\otimes\mathbf{e}_\phi + \mathbf{e}_\phi\otimes\mathbf{e}_\theta) \qquad \text{for } n=3\end{aligned} \tag{5.6}$$

with its components being

$$\epsilon_{rr} = u', \qquad \epsilon_{\theta\theta} = \epsilon_{\phi\phi} = \frac{u}{r}, \qquad \epsilon_{r\theta} = \epsilon_{r\phi} = \epsilon_{\theta\phi} = 0, \tag{5.7}$$

where $(\cdot)' \coloneqq d(\cdot)/dR$. Similarly, the stress tensor is given by either

$$\mathbf{T} = \sigma_{rr}\,\mathbf{e}_r\otimes\mathbf{e}_r + \sigma_{\theta\theta}\,\mathbf{e}_\theta\otimes\mathbf{e}_\theta + \sigma_{r\theta}\,(\mathbf{e}_r\otimes\mathbf{e}_\theta + \mathbf{e}_\theta\otimes\mathbf{e}_r) \qquad \text{for } n=2 \tag{5.8}$$

or by

$$\begin{aligned}\mathbf{T} =\,&\sigma_{rr}\,\mathbf{e}_r\otimes\mathbf{e}_r + \sigma_{\theta\theta}\,\mathbf{e}_\theta\otimes\mathbf{e}_\theta + \sigma_{\phi\phi}\,\mathbf{e}_\phi\otimes\mathbf{e}_\phi + \sigma_{r\theta}\,(\mathbf{e}_r\otimes\mathbf{e}_\theta + \mathbf{e}_\theta\otimes\mathbf{e}_r)\\ &+\,\sigma_{r\phi}\,(\mathbf{e}_r\otimes\mathbf{e}_\phi + \mathbf{e}_\phi\otimes\mathbf{e}_r) + \sigma_{\theta\phi}\,(\mathbf{e}_\theta\otimes\mathbf{e}_\phi + \mathbf{e}_\phi\otimes\mathbf{e}_\theta) \qquad \text{for } n=3\end{aligned} \tag{5.9}$$

and is related to its respective strain tensor $\mathbf{E}$ by the Generalized Hooke's law given by (3.60a). Thus, the stress components of (5.8) and (5.9) are given by

$$\begin{aligned}\sigma_{rr} &= c_{11}u' + (n-1)\,c_{12}\frac{u}{R},\\ \sigma_{\theta\theta} = \sigma_{\phi\phi} &= c_{12}u' + c_{22}\frac{u}{R} + (n-2)\,c_{23}\frac{u}{R},\\ \sigma_{r\theta} &= \sigma_{r\phi} = \sigma_{\theta\phi} = 0.\end{aligned} \tag{5.10}$$

Because of the assumption of radial symmetry of the displacement field, given by either (5.3) or (5.4), the determinant of the deformation gradient can be written as

$$\det(\mathbf{1}+\nabla\mathbf{u}) = (1+u')\left(1+\frac{u}{R}\right)^{n-1}. \tag{5.11}$$

For $n=2$, it follows from (3.60a) and (3.61) together with (5.5) and (5.8) that

$$\mathcal{E}[\mathbf{u}] = \frac{1}{2}\int_{\mathcal{B}} (\sigma_{rr}\,\epsilon_{rr} + \sigma_{\theta\theta}\,\epsilon_{\theta\theta} + 2\,\sigma_{r\theta}\,\epsilon_{r\theta})\;dV - \int_{\partial\mathcal{B}} -p\,\mathbf{e}_r\cdot\mathbf{u}\,dA \tag{5.12}$$

and from (4.3) and (5.11) that

$$\mathcal{P}[\mathbf{u}] = \int_{\mathcal{B}} \frac{1}{(1+u')(1+u/R)-\varepsilon}\, dV. \tag{5.13}$$

Since $\mathcal{B}$ is two dimensional, we have that $dV = R\, dR\, d\Theta$ and $dA = R_e\, d\Theta$, which together with (5.3), (5.7) and (5.10) allow us to write

$$\begin{aligned}\mathcal{E}[\mathbf{u}] = &\frac{1}{2}\int_0^{2\pi}\int_0^{R_e}\left[c_{11}\,(u')^2 + 2c_{12}\,\frac{u}{R}\,u' + c_{22}\frac{u^2}{R^2}\right] R\, dR\, d\Theta \\ &+ \int_0^{2\pi} p\, u(R_e)\, R_e\, d\Theta\end{aligned} \tag{5.14}$$

and

$$\mathcal{P}[\mathbf{u}] = \int_0^{2\pi}\int_0^{R_e} \frac{1}{(1+u')(1+u/R)-\varepsilon}\, R\, dR\, d\Theta. \tag{5.15}$$

After integrating on Θ, (5.14) and (5.15) become

$$\mathcal{E}[\mathbf{u}] = \pi \int_0^{R_e}\left[c_{11}\, R\,(u')^2 + 2c_{12}\, u\, u' + c_{22}\frac{1}{R}u^2\right] dR + 2\pi\, R_e\, p\, u(R_e) \tag{5.16}$$

and

$$\mathcal{P}[\mathbf{u}] = 2\pi \int_0^{R_e} \frac{R}{(1+u')\,(1+u/R)-\varepsilon}\, dR. \tag{5.17}$$

Similarly, for $n = 3$, it follows from (3.60a) and (3.61) together with (5.6) and (5.9) that

$$\begin{aligned}\mathcal{E}[\mathbf{u}] = &\frac{1}{2}\int_{\mathcal{B}} (\sigma_{rr}\,\epsilon_{rr} + \sigma_{\theta\theta}\,\epsilon_{\theta\theta} + \sigma_{\phi\phi}\,\epsilon_{\phi\phi} + 2\,\sigma_{r\theta}\,\epsilon_{r\theta} + 2\,\sigma_{r\phi}\,\epsilon_{r\phi} + 2\,\sigma_{\theta\phi}\,\epsilon_{\theta\phi})\, dV \\ &- \int_{\partial\mathcal{B}} -p\,\mathbf{e}_r\cdot\mathbf{u}\, dA\end{aligned} \tag{5.18}$$

and from (4.3) and (5.11) that

$$\mathcal{P}[\mathbf{u}] = \int_{\mathcal{B}} \frac{1}{(1+u')(1+u/R)^2-\varepsilon}\, dV. \tag{5.19}$$

Here, $\mathcal{B}$ is three dimensional, yielding $dV = R^2\,\sin\Phi\, dR\, d\Theta\, d\Phi$ and $dA = R_e^2\,\sin\Phi\, d\Theta\, d\Phi$, which together with (5.4), (5.7) and (5.10) allow us to write

$$\begin{aligned}\mathcal{E}[\mathbf{u}] = &\frac{1}{2}\int_0^{\pi}\int_0^{2\pi}\int_0^{R_e}\left[c_{11}\,(u')^2 + 4c_{12}\,\frac{u}{R}\,u' + 2(c_{22}+c_{23})\frac{u^2}{R^2}\right] R^2\, dR\, d\Theta\, d\Phi \\ &+ \int_0^{\pi}\int_0^{2\pi} p\, u(R_e)\, R_e^2\,\sin\Phi\, d\Theta\, d\Phi\end{aligned} \tag{5.20}$$

and

$$\mathcal{P}[\mathbf{u}] = \int_0^{\pi}\int_0^{2\pi}\int_0^{R_e} \frac{1}{(1+u')(1+u/R)^2-\varepsilon}\, R^2\,\sin\Phi\, dR\, d\Theta\, d\Phi. \tag{5.21}$$

After integrating on both Θ and Φ, (5.20) and (5.21) become

$$\mathcal{E}[\mathbf{u}] = 2\pi \int_0^{R_e}\left[c_{11}\,(Ru')^2 + 4c_{12}\, R\, u\, u' + 2(c_{22}+c_{23})u^2\right] dR + 4\pi\, p\, u(R_e)\, R_e^2 \tag{5.22}$$

and

$$\mathcal{P}[\mathbf{u}] = 4\pi \int_0^{R_e} \frac{R^2}{(1+u')\,(1+u/R)^2 - \varepsilon}\, dR. \tag{5.23}$$

Finally, comparing expressions (5.16) with (5.22) and (5.17) with (5.23), we can write the potential energy $\mathcal{E}[\mathbf{u}]$ and the barrier functional $\mathcal{P}[\mathbf{u}]$ for the n-sphere problem as

$$\mathcal{E}[\mathbf{u}] = (n-1)\,\pi \int_0^{R_e} \left[c_{11}\, R\,(u')^2 + (n-1)\,(2c_{12}\,u\,u' + c_{22}\frac{u^2}{R}) + 2(n-2)\,c_{23}\,\frac{u^2}{R} \right] R^{n-2}\, dR$$
$$+ 2(n-1)\,\pi\, R_e\, p\, u(R_e) \tag{5.24}$$

and

$$\mathcal{P}[\mathbf{u}] = 2(n-1)\pi \int_0^{R_e} \frac{R^{n-1}}{(1+u')\,(1+u/R)^{n-1} - \varepsilon}\, dR. \tag{5.25}$$

5.2 Analytical results

5.2.1 Unconstrained disk problem

We review the main results found by Lekhnitskii (1968) concerning the analytical solution of the circular disk problem ($n = 2$) in the context of the classical linear elasticity theory. Following Fosdick and Royer-Carfagni (2001), we show that this solution predicts material overlapping. The radial symmetry of the displacement field (5.3) reduces the vector equation of equilibrium (3.60c) into only one non-trivial scalar equation given by

$$\sigma'_{rr} + \frac{\sigma_{rr} - \sigma_{\theta\theta}}{R} = 0, \tag{5.26}$$

which, because of (5.10), takes the form

$$c_{11} u'' + c_{11}\frac{u'}{R} - c_{22}\frac{u}{R^2} = 0. \tag{5.27}$$

By imposing the boundary condition $\sigma_{rr}(R_e) = -p$ and the compatibility equation $u(0) = 0$, we obtain

$$u(R) = \frac{-p}{(\sqrt{c_{22}c_{11}} + c_{12}) R_e^{k-1}} R^k, \tag{5.28}$$

where k is defined as

$$k \coloneqq \sqrt{\frac{c_{22}}{c_{11}}} > 0. \tag{5.29}$$

Uniqueness of solution in the classical linear elasticity theory guarantees that (5.28) is the only solution for the unconstrained disk problem. In this work we refer to (5.28) as the unconstrained solution.

It follows from (5.10) and (5.28) that the radial and hoop stresses are given by, respectively,

$$\sigma_{rr} = -p \left(\frac{R}{R_e}\right)^{k-1}, \qquad \sigma_{\theta\theta} = -p\,k \left(\frac{R}{R_e}\right)^{k-1}. \tag{5.30}$$

Observe from (5.30) that both σ_{rr} and $\sigma_{\theta\theta}$ are singular at the origin for any value of pressure p when $k < 1$.

In order to show that (5.28) predicts material overlapping for any value of pressure $p > 0$ if $k < 1$, we consider each one of the two terms inside the parentheses in (5.11) separately. It follows from (5.28) that these terms are given by

$$1 + u' = 1 - \frac{p}{\sqrt{c_{11}c_{22}} + c_{12}} k \left(\frac{R}{R_e}\right)^{k-1} \tag{5.31}$$

and

$$1 + \frac{u}{R} = 1 - \frac{p}{\sqrt{c_{11}c_{22}} + c_{12}} \left(\frac{R}{R_e}\right)^{k-1}. \tag{5.32}$$

We then see from (5.31) and (5.32) that, respectively,

$$1 + u' \begin{cases} \leq 0 & \text{if } \left(\dfrac{R}{R_e}\right)^{1-k} \leq \dfrac{p}{\sqrt{c_{11}c_{22}} + c_{12}} k, \\ > 0 & \text{otherwise,} \end{cases} \tag{5.33}$$

and

$$1 + \frac{u}{R} \begin{cases} < 0 & \text{if } \left(\dfrac{R}{R_e}\right)^{1-k} < \dfrac{p}{\sqrt{c_{11}c_{22}} + c_{12}}, \\ \geq 0 & \text{otherwise.} \end{cases} \tag{5.34}$$

Note from (5.33) and (5.34) that if $k < 1$, we have $1 + u' > 0$ and $1 + u/R < 0$ for

$$\frac{p}{\sqrt{c_{11}c_{22}} + c_{12}} k < \left(\frac{R}{R_e}\right)^{1-k} < \frac{p}{\sqrt{c_{11}c_{22}} + c_{12}}, \tag{5.35}$$

and therefore, the determinant of the deformation gradient $\det \nabla \mathbf{f}$, given by (5.11), is negative in the annular region defined by (5.35). Moreover, observe from (5.28) that in the region defined by

$$0 < \left(\frac{R}{R_e}\right)^{1-k} < \frac{p}{\sqrt{c_{11}c_{22}} + c_{12}}, \tag{5.36}$$

we have $u(R) < -R$. Since the tangential displacement is null, this means that points $\mathbf{X}$ in this region are mapped to points $\mathbf{x}$ through the center of the disk, which characterizes material overlapping, in spite of the fact that the determinant of the deformation gradient is positive inside the circle defined by the inner radius of the annular region (5.35). Finally, note that the region (5.36) exists for any value of pressure $p > 0$ when $k < 1$.

5.2.2 Constrained radially symmetric disk problem

Fosdick and Royer-Carfagni (2001) solved the Euler-Lagrange equations (3.66)-(3.68) for the problem of the circular disk ($n = 2$). Here, we present some of the results found by the authors. The radial displacement u in (5.3) is given by

$$u(R) = \begin{cases} (-1 + \sqrt{\varepsilon})R & \text{in } \mathcal{B}_=, \\ AR^k + BR^{-k} & \text{in } \mathcal{B}_>, \end{cases} \tag{5.37}$$

where

$$\mathcal{B}_{=} \coloneqq \{\mathbf{X} = R\,\mathbf{e}_r \in \mathcal{B} \mid 0 \leq R \leq R_c\}, \qquad \mathcal{B}_{>} \coloneqq \{\mathbf{X} = R\,\mathbf{e}_r \in \mathcal{B} \mid R_c \leq R \leq R_e\}, \tag{5.38}$$

$$A = \frac{1+k}{2k}(\sqrt{\varepsilon}-1)R_c^{-k+1}, \qquad B = \frac{-1+k}{2k}(\sqrt{\varepsilon}-1)R_c^{k+1}. \tag{5.39}$$

In (5.38), R_c is the radius of the region where the injectivity constraint is active, i.e., $\det \nabla \mathbf{f} = \varepsilon$, which is obtained by solving the equation

$$(1+k)(c_{11}k + c_{12})\left(\frac{R_e}{R_c}\right)^{k-1} + (1-k)(c_{11}k - c_{12})\left(\frac{R_e}{R_c}\right)^{-k-1} + \frac{2kp}{\sqrt{\varepsilon}-1} = 0. \tag{5.40}$$

The Lagrange multiplier field is given by

$$\lambda(R) = \begin{cases} -\dfrac{1-\sqrt{\varepsilon}}{\sqrt{\varepsilon}}(c_{11}-c_{22})\log\left(\dfrac{R}{R_c}\right) & \text{in } \mathcal{B}_{=}, \\ 0 & \text{in } \mathcal{B}_{>}, \end{cases} \tag{5.41}$$

and the determinant of the deformation gradient can be written as

$$\det \nabla \mathbf{f}(R\,\mathbf{e}_r) = \begin{cases} \varepsilon & \text{in } \mathcal{B}_{=}, \\ g_1\left(\dfrac{R}{R_c}\right) g_2\left(\dfrac{R}{R_c}\right) & \text{in } \mathcal{B}_{>}, \end{cases} \tag{5.42}$$

where $\mathbf{f}(R\,\mathbf{e}_r) = [R + u(R)]\mathbf{e}_r$ and

$$\begin{aligned} g_1\left(\frac{R}{R_c}\right) &\coloneqq 1 + \frac{\sqrt{\varepsilon}-1}{2k}\left[(k+1)\left(\frac{R}{R_c}\right)^{k-1} + (k-1)\left(\frac{R}{R_c}\right)^{-k-1}\right], \\ g_2\left(\frac{R}{R_c}\right) &\coloneqq 1 + \frac{\sqrt{\varepsilon}-1}{2}\left[(k+1)\left(\frac{R}{R_c}\right)^{k-1} - (k-1)\left(\frac{R}{R_c}\right)^{-k-1}\right]. \end{aligned} \tag{5.43}$$

Even though expression (5.42) yields $\det \nabla \mathbf{f} \geq \varepsilon$ everywhere in the interval $(0, R_e)$, expression (5.41) yields a constraint reaction inside the body, given by $-\varepsilon\,\lambda\,(\nabla \mathbf{f})^{-T}$, that is still singular at the center of the disk.

5.2.3 Constrained radially symmetric sphere problem

Aguiar (2006) solved the Euler-Lagrange equations (3.66)-(3.68) for the ordinary sphere problem ($n = 3$). Here, we present some of the results found by the author. The radial displacement u in (5.4) is given by

$$u(R) = \begin{cases} -(1-\varepsilon^{1/3})\,R & \text{in } \mathcal{B}_{=}, \\ \dfrac{(1-\varepsilon^{1/3})\,R_c}{2\,\kappa}\left[-(1+\kappa)\left(\dfrac{R}{R_c}\right)^{-(1-3\kappa)/2} + (1-\kappa)\left(\dfrac{R}{R_c}\right)^{-(1+3\kappa)/2}\right] & \text{in } \mathcal{B}_{>}, \end{cases} \tag{5.44}$$

where

$$\mathcal{B}_{=} \coloneqq \{\mathbf{X} = R\,\mathbf{e}_r \in \mathcal{B} \mid 0 < R < R_c\}, \qquad \mathcal{B}_{>} \coloneqq \{\mathbf{X} = R\,\mathbf{e}_r \in \mathcal{B} \mid R_c < R < R_e\}, \tag{5.45}$$

$$\kappa := \frac{1}{3}\sqrt{1+8\,\gamma}, \qquad \gamma := \frac{c_{22}+c_{23}-c_{12}}{c_{11}}. \tag{5.46}$$

As in Section 5.2.2, R_c in (5.45) is the radius of the region where the injectivity constraint is active, i.e., $\det \nabla \mathbf{f} = \varepsilon$, which is obtained by solving the equation

$$(\lambda^+ + 2\,\eta)\left(\frac{1+\kappa}{2\,\kappa}\right)\zeta^{3(\kappa-1)/2} - (\lambda^- + 2\,\eta)\left(\frac{1-\kappa}{2\,\kappa}\right)\zeta^{-3(\kappa+1)/2} - \frac{p}{c_{11}\,(1-\varepsilon^{1/3})} = 0, \tag{5.47}$$

where

$$\zeta := \frac{R_e}{R_c}\,, \qquad \eta := \frac{c_{12}}{c_{11}}\,, \qquad \lambda^{\pm} := \frac{1}{2}\,(-1 \pm 3\,\kappa). \tag{5.48}$$

Equation (5.47) is analogous to equation (5.40) in the case of the constrained radially symmetric disk problem. The Lagrange multiplier field is given by

$$\lambda(R) = \begin{cases} 2c_{11}\,\varepsilon^{-2/3}(1-\varepsilon^{-1/3})(-1+\gamma)\log(R/R_c) & \text{in } \mathcal{B}_{=}, \\ 0 & \text{in } \mathcal{B}_{>}, \end{cases} \tag{5.49}$$

and the determinant of the deformation gradient can be written as

$$\det \nabla \mathbf{f}(R\,\mathbf{e}_r) = \begin{cases} \varepsilon & \text{in } \mathcal{B}_{=}, \\ [1+\chi_1(\psi)]\,[1-\chi_2(\psi)]^2 & \text{in } \mathcal{B}_{>}, \end{cases} \tag{5.50}$$

where $\mathbf{f}(R\,\mathbf{e}_r) = [R + u(R)]\mathbf{e}_r$ and

$$\begin{aligned} \chi_1(\psi) &:= \frac{(1-\varepsilon^{1/3})}{4\,\kappa\,\psi^{3/2}}\left[(1+\kappa)(1-3\,\kappa)\,\psi^{3\,\kappa/2} - (1-\kappa)(1+3\,\kappa)\,\psi^{-3\,\kappa/2}\right], \\ \chi_2(\psi) &:= \frac{(1-\varepsilon^{1/3})}{2\,\kappa\,\psi^{3/2}}\left[(1+\kappa)\,\psi^{3\,\kappa/2} - (1-\kappa)\,\psi^{-3\,\kappa/2}\right], \qquad \psi := \frac{R}{R_c} \geq 1. \end{aligned} \tag{5.51}$$

As in Section 5.2.2, expression (5.50) yields $\det \nabla \mathbf{f} \geq \varepsilon$ everywhere in the interval $(0, R_e)$ and expression (5.49) yields a constraint reaction inside the body, given by $-\varepsilon\,\lambda\,(\nabla \mathbf{f})^{-T}$, that is singular at the center of the sphere.

5.2.4 Asymptotic analysis of the unconstrained disk problem

In the previous sections we have considered the n-dimensional sphere problem in the context of unconstrained and constrained minimization theories. The assumption of radially symmetric solutions of the corresponding boundary value problems has allowed us to find closed-form expressions for these solutions. The search for more general solutions in the case of the constrained theory and for solutions of more complex problems, for which closed-form expressions may not be known, has motivated the study of the present section. The study is based on the fact that the governing differential equations of these problems may contain a small parameter ξ that can be used to represent approximate solutions of these equations in terms of power series. This representation is the basis of the regular

perturbation method presented in this section, which is used to obtain an approximate solution of the unconstrained disk problem of Section 5.2.1.

We begin by considering that $c_{22} \approx c_{11}$. We then define the small parameter

$$\xi := 1 - \frac{c_{22}}{c_{11}} \tag{5.52}$$

and write the governing differential equation of the unconstrained disk problem, given by (5.27), as

$$L^{\xi} u = f, \qquad L^{\xi} := \frac{d^2}{dR^2} + \frac{1}{R}\frac{d}{dR} - \frac{1}{R^2}(1-\xi), \qquad f = 0. \tag{5.53}$$

In the particular case $\xi = 0$, the expressions in (5.53) become

$$L^{0} u = f, \qquad L^{0} := \frac{d^2}{dR^2} + \frac{1}{R}\frac{d}{dR} - \frac{1}{R^2}, \qquad f = 0. \tag{5.54}$$

In perturbation theory, equations (5.53) and (5.54) are called perturbed and unperturbed equations, respectively (NAYFEH, 1993, p. 28). The regular perturbation method is particularly appropriate when the unperturbed equation (5.54) corresponds to a relatively simple problem with known solution. This is the case here, because $\xi = 0$ in (5.52) corresponds to the isotropic case, $c_{11} = c_{22}$, which is simpler than the anisotropic case represented by the perturbed equation (5.53). In addition, in our case, even the solution of the perturbed equation (5.53) is known and given by (5.28). Recall from above, however, that the objective of this section is to introduce a method that could be applied in the investigation of more complex problems.

Then, we propose an approximate solution of (5.53) given by the power series

$$u^{(m)}(R,\xi) = \sum_{i=0}^{m} \xi^i \, u_i(R), \tag{5.55}$$

where u_i are functions to be determined below. Substituting (5.55) into (5.53), we obtain

$$\begin{aligned} L^{\xi}\, u^{(m)} - f &= \left[\frac{d^2}{dR^2} + \frac{1}{R}\frac{d}{dR} - \frac{1}{R^2}(1-\xi)\right] \sum_{i=0}^{m} \xi^i \, u_i(R) \\ &= \xi^{m+1}\frac{u_m}{R^2} + \xi^0 \left(\frac{d^2}{dR^2}u_0 + \frac{1}{R}\frac{d}{dR}u_0 - \frac{u_0}{R^2}\right) \\ &\quad + \sum_{i=1}^{m} \xi^i \left(\frac{d^2}{dR^2}u_i + \frac{1}{R}\frac{d}{dR}u_i - \frac{u_i}{R^2} + \frac{u_{i-1}}{R^2}\right). \end{aligned} \tag{5.56}$$

To determine $u_i(R)$, $i = 0, 1, 2, ..., m$, we solve a sequence of differential equations given by

$$\begin{aligned} &\frac{d^2}{dR^2}u_0 + \frac{1}{R}\frac{d}{dR}u_0 - \frac{u_0}{R^2} = 0, \\ &\frac{d^2}{dR^2}u_i + \frac{1}{R}\frac{d}{dR}u_i - \frac{u_i}{R^2} = \frac{u_{i-1}}{R^2} \qquad \text{for } i \geq 1. \end{aligned} \tag{5.57}$$

We then have that the substitution of $u^{(m)}$, given by (5.55) together with the solutions $u_i(R)$, $i = 0, 1, \ldots, m$, into the differential equation (5.53) yield a residue of order $O(\xi^{m+1})$, which is given by $\xi^{m+1}\, u_m/R^2$.

The approximation $u^{(m)}(R, \xi)$ must also satisfy the boundary condition $\sigma_{rr}(R_e) = -p$, where $\sigma_{rr}(R)$ is given by (5.10a) in the case $n = 2$, and the compatibility condition $u^{(m)}(0, \xi) = 0$. This is achieved by requiring that $u_i(R)$ satisfies, not only (5.57), but also

$$\left(c_{11}\frac{du_i}{dR} + c_{12}\frac{u_i}{R}\right)\bigg|_{R=R_e} = \begin{cases} -p & \text{for } i = 0, \\ 0 & \text{for } i \geq 1, \end{cases} \tag{5.58}$$

and

$$u_i(0) = 0 \quad \text{for } i \geq 0. \tag{5.59}$$

It follows from (5.57a), (5.58a) and (5.59) that $u_0(R)$ is given by

$$u_0(R) = -\bar{p}\, R, \tag{5.60}$$

where $\bar{p} \coloneqq p/\bar{c}$ and $\bar{c} \coloneqq c_{11} + c_{12}$. Clearly, (5.60) is the solution of the isotropic disk problem. Then, we determine $u_i(R)$, for $i = 1, 2, 3$, which is enough for the purpose of this section, by solving (5.57b), together with (5.58b), (5.59) and (5.60), yielding

$$u_1(R) = -\frac{1}{2\,\bar{c}}\,\bar{p}\, R\,[-\bar{c}\,\log R + c_{11}]\,, \tag{5.61}$$

$$u_2(R) = -\frac{1}{8\,\bar{c}^2}\,\bar{p}\, R\left[(\bar{c}\,\log R)^2 - (3c_{11} + c_{12})\bar{c}\,\log R + (3c_{11} + c_{12})\,c_{11}\right], \tag{5.62}$$

$$\begin{aligned} u_3(R) = -\frac{1}{48\,\bar{c}^3}\,\bar{p}\, R\Big[&-(\bar{c}\,\log R)^3 + 3\,(2\,c_{11} + c_{12})(\bar{c}\,\log R)^2 \\ &- 3\,(5\,c_{11}^2 + 4\,c_{12}\,c_{11} + c_{12}^2)\,\bar{c}\,\log R + 3\,(5\,c_{11}^2 + 4\,c_{12}\,c_{11} + c_{12}^2)\,c_{11}\Big]. \end{aligned} \tag{5.63}$$

In Figure 10, we show curves for $u^{(m)}$, given by (5.55), for $m = 0, 1, 2, 3$ and for three different cases corresponding to $\xi = 0.9, 0.5, 0.1$. For comparison purposes, we also show the exact solution of each case, given by (5.28). We present the results in two scales, where the figures on the left-hand side refer to the interval $R \in (0, 1)$ and the figures on the right-hand side refer to the interval $R \in (0, 0.05)$. These curves were obtained by considering $c_{11} = 10^5$, $c_{12} = 10^3$, $p = 500$, $R_e = 1$. Because of (5.29) and (5.52), once we define ξ, the pair of values $\{c_{22}, k\}$ is also defined. The cases $\xi = 0.9$, 0.5, 0.1 correspond to $\{c_{22}, k\} = \{10^4, 0.316\}$, $\{5 \times 10^4, 0.707\}$, $\{9 \times 10^4, 0.949\}$, respectively.

We see from Figure 10 that, in both scales, $u^{(m)}$, $m = 0, 1, 2, 3$, approaches the exact solution as m increases or ξ decreases. In particular, we see from this figure that the curves for $u^{(m)}$ are far from the exact solution in the case $\xi = 0.9$ when compared to the corresponding curves in the other two cases, given by $\xi = 0.5$ and $\xi = 0.1$. In addition, for $\xi = 0.1$, we see that $u^{(1)}$, $u^{(2)}$ and $u^{(3)}$ are very close to the exact solution, with the last two approximate solutions being indistinguishable from the exact solution in both scales.

Figure 10 – Radial displacement u versus radius R for unconstrained disk problem considering the cases $\xi = 0.9, 0.5, 0.1$.

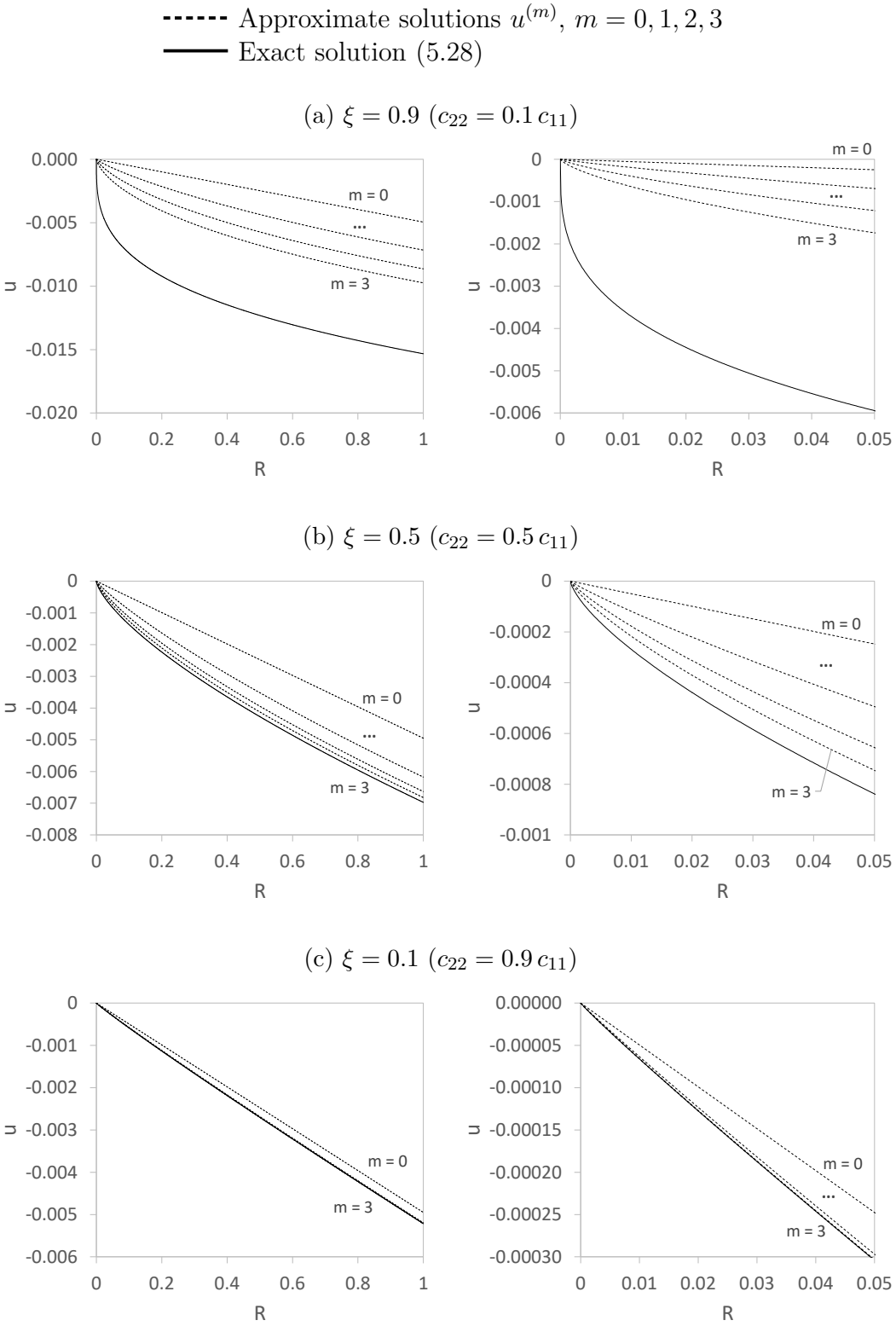

Source: The author.

5.3 Numerical results and discussion

In this section, we reproduce some of the numerical results obtained by Aguiar (2006) and compare them with results obtained from the analytical solutions presented in section 5.2, which are based on the assumption of radial symmetry, with the aim of validating the computational procedure that will be used in Chapter 6 to find solutions that are not radially symmetric.

For the disk problem ($n = 2$), we have chosen the same material and geometric parameters used by Fosdick and Royer-Carfagni (2001), that is, $p = 500$, $c_{11} = 10^5$, $c_{22} = c_{12} = 10^3$, $\varepsilon = 0.1$ and $R_e = 1$, which results in $R_c \approx 0.0058307$ and $k = 0.1$.

For the sphere problem ($n = 3$), we have chosen the same material and geometric parameters used by Aguiar (2006), that is, $p = 1000$, $\eta = 0.5$, $c_{11} = 10^5$, $c_{22} = 5 \times 10^4$, $c_{23} = 5.5 \times 10^3$, $\varepsilon = 0.1$ and $R_e = 1$, yielding $R_c \approx 0.0057913$ and $\kappa = 0.4$.

For both $n = 2$ and $n = 3$, we have chosen the same numerical parameters $\varepsilon_{\mathbf{s}} = 10^{-12}$ in (4.12), $\varepsilon_\alpha = 10^{-12}$ and $N_\alpha = 50$ in (4.18), and the sequence $\{10^{-2}, 10^{-1}, 10^0, 10^1, ..., 10^8\}$ for the penalty parameter δ in (4.7). Our numerical experiments have confirmed that the numerical results do not change significantly for $\delta > 10^8$.

For each n, we considered the same two types of meshes using linear finite elements, which are uniform meshes with N elements and the non-uniform mesh used by Aguiar (2006). The non-uniform mesh is composed of 480 elements distributed in three regions: 300 elements in $0 < R < 0.07\,R_e$, 100 elements in $0.07\,R_e < R < 0.46\,R_e$ and 80 elements in $0.46\,R_e < R < R_e$.

In Figures 11a and 11b we show the displacement field u against the radius $R \in (0, 1)$ for $n = 2$ and $n = 3$, respectively. The solid lines represent the exact solutions given by (5.37) for $n = 2$ and by (5.44) for $n = 3$. The dashed lines represent the numerical solutions obtained from uniform meshes. For both $n = 2$ and $n = 3$, we see from these figures that the numerical solutions converge to the analytical solutions as the mesh is refined. We also see that the numerical solutions obtained from a uniform mesh with 64 elements may already be considered a good approximation, even though no element is completely inside the active zone $(0, R_c)$, since the size of each element is $1/64 = 0.015625$, which is greater than the radius $R_c \approx 0.0058307$ for $n = 2$ and the radius $R_c \approx 0.0057913$ for $n = 3$.

In Figures 12a and 12b we show the base 10 logarithm of the Euclidean norm of the error between the exact solution u and the numerical solution u_h, $\|u - u_h\|_2$, versus the base 10 logarithm of the penalty parameter δ for uniform and the non-uniform meshes. Figures 12a and 12b refer to the exact solutions given by, respectively, (5.37) for $n = 2$ and (5.44) for $n = 3$. We see from the curves of both figures that, in general, the error decreases as δ increases until it reaches a minimum and then it remains nearly constant thereafter.

Figure 11 – Radial displacement u versus radius R for the constrained radially symmetric disk and sphere problems using uniform meshes and for $\delta = 10^8$.

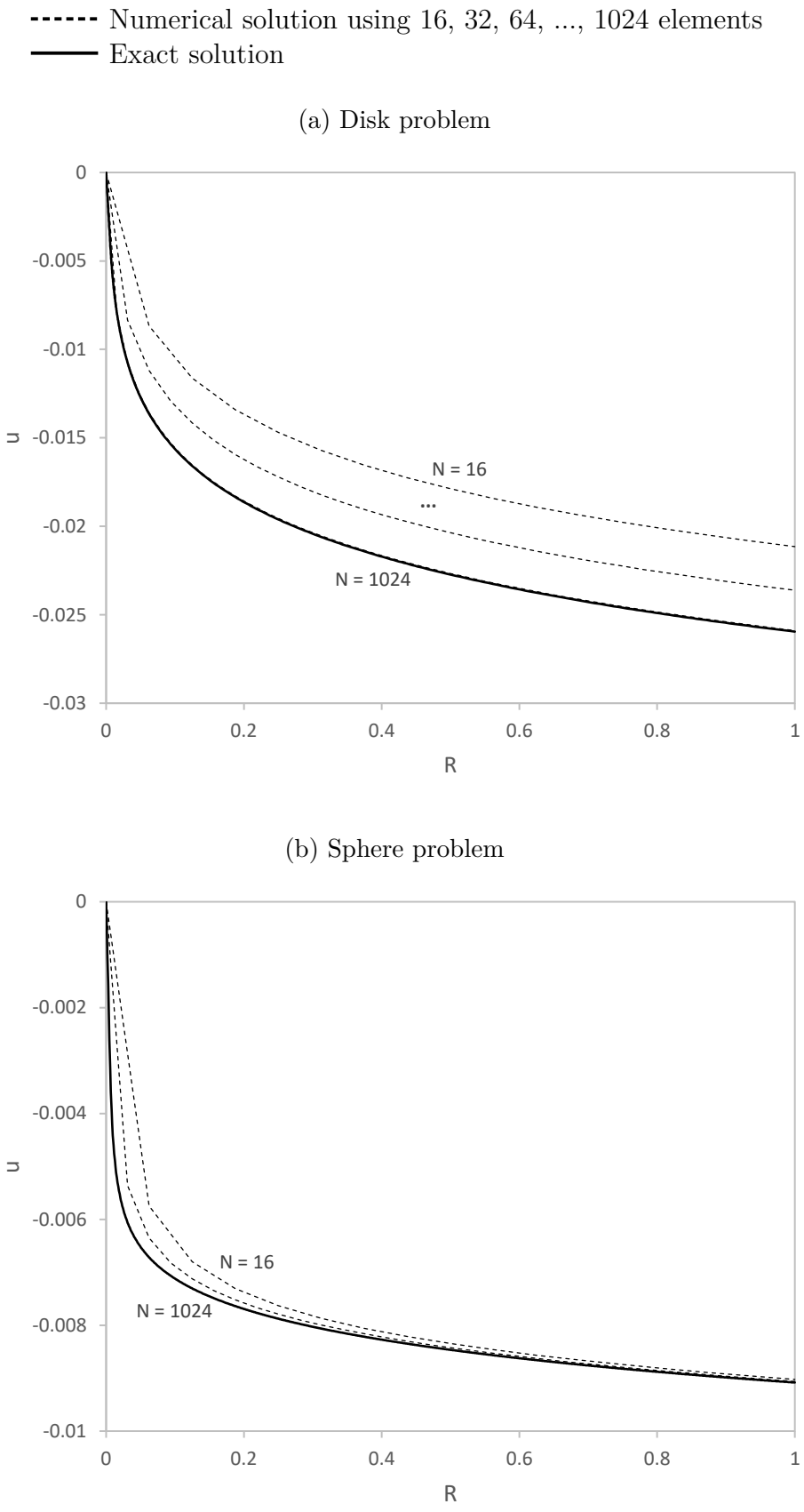

Source: The author.

In the case of the two coarsest meshes, the error increases after $\delta = 1$ for $N = 128$ and $\delta = 10$ for $N = 256$, reaching a constant value for high enough δ. For high values of δ and N and for both values of n, we also see that the error decreases as the uniform meshes are refined and that the non-uniform mesh yields the lowest error, even though it has less elements. In the case of the disk problem, the error for $N = 256$ is larger than the error for $N = 128$. This non monotonic behavior of the error concerning the uniform meshes is also observed by Aguiar (2006) in the case of $n = 3$ between $N = 64$ and $N = 128$. We do not see this behavior in Figure 12b, here, N starts at 128.

In Figure 13a we show dashed lines representing the radial displacement of the disk problem obtained with the non-uniform mesh of 480 elements for different values of the penalty parameter δ. The exact solution given by (5.37) is represented by the solid line. Figure 13b shows analogous results for the sphere problem, where the exact solution is given by (5.44). The graphs of both problems are analogous and show that the numerical solution approaches the exact one as δ increases, as expected from the numerical procedure based on the interior penalty formulation presented in Chapter 4.

In Figures 14a and 14b we show curves for the determinant of the deformation gradient $J \coloneqq \det \nabla \mathbf{f} = \det (\mathbf{1} + \nabla \mathbf{u})$ calculated from both the exact and the numerical solutions. Figure 14a concerns the disk problem and Figure 14b the sphere problem. We see from these figures that the numerical solutions and the exact solutions are indistinguishable. Thus, the determinant obtained numerically is a very good approximation for the exact determinant given by (5.42) in the case of $n = 2$ and given by (5.50) in the case of $n = 3$.

Figures 15a and 15b are a magnification of figures 14a and 14b in $R \in (0, 0.05)$, respectively. Again, we see that the curves that represent the numerical and the exact solution are indistinguishable, which shows that the determinant obtained numerically is also a very good approximation for the exact determinant near the center of the n-sphere.

In Figure 16a we show both the Lagrange multiplier field λ given by (5.41), represented by the solid line, and the approximations λ_δ obtained by (4.4) with $\delta = 10^8$, represented by dashed lines. Figure 16b shows analogous results for the sphere problem, therefore λ is given by (5.49) in this case. We see from both figures that the approximation λ_δ converges to λ as the uniform meshes are refined. Again, we see that the result obtained with the non-uniform mesh, which has more elements in $\mathcal{B}_=$ than the most refined uniform mesh, yields a better approximation of the exact value λ.

The results presented in this chapter are in very good agreement with the literature. Our numerical results for $n = 2$ and $n = 3$ converged to analytical results of Fosdick and Royer-Carfagni (2001) and Aguiar (2006), respectively. In addition, for $n = 3$ we also reproduced computational results of Aguiar (2006), but with a small difference between his Figures 7 and 9 and our Figures 15b and 16b, respectively. We see from his Figure 7 that his curve for the exact solution is sightly smoother than ours and his curve for the

Figure 12 – The logarithm of the error $e \coloneqq ||u - u_h||_2$ versus the logarithm of the penalty parameter δ for the constrained radially symmetric disk and sphere problems.

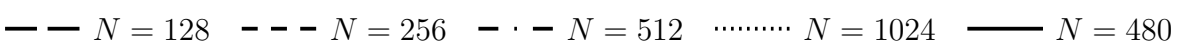

(a) Disk problem

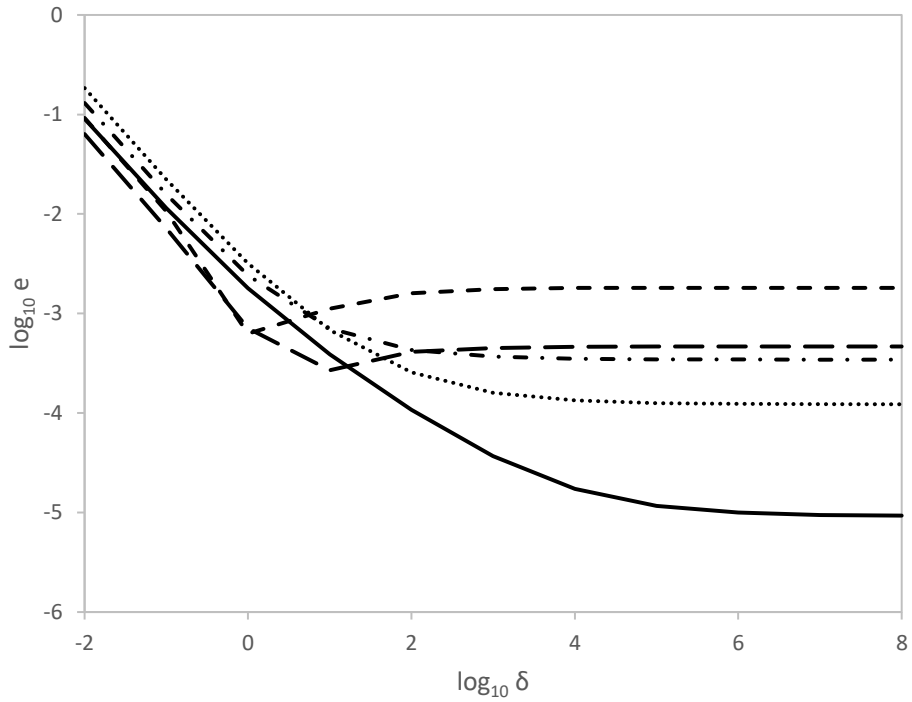

(b) Sphere problem

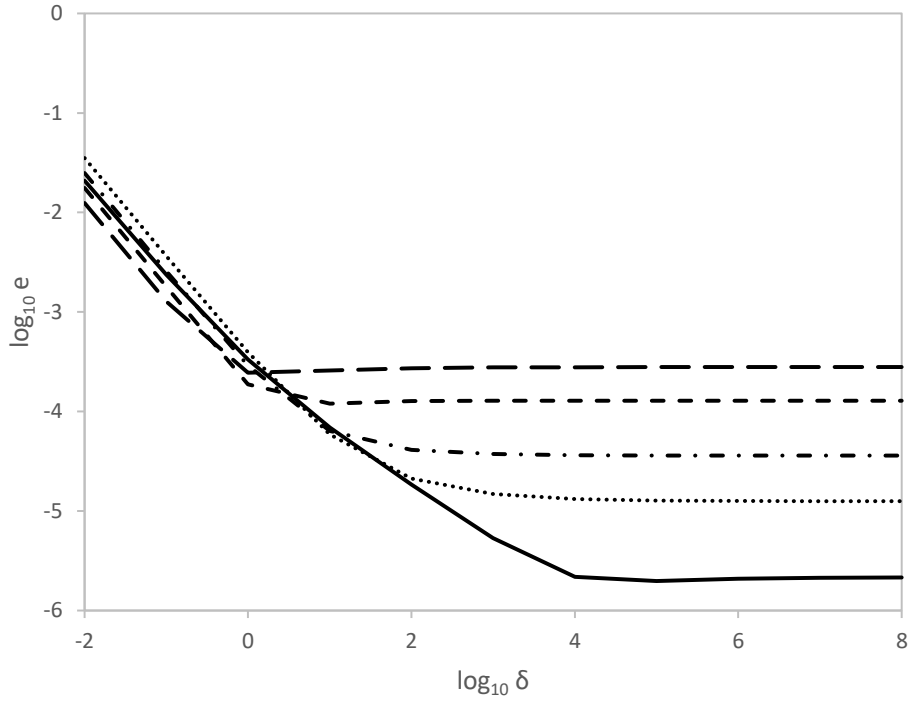

Source: The author.

Figure 13 – Radial displacement u versus radius R for the constrained radially symmetric disk and sphere problems using 480 elements.

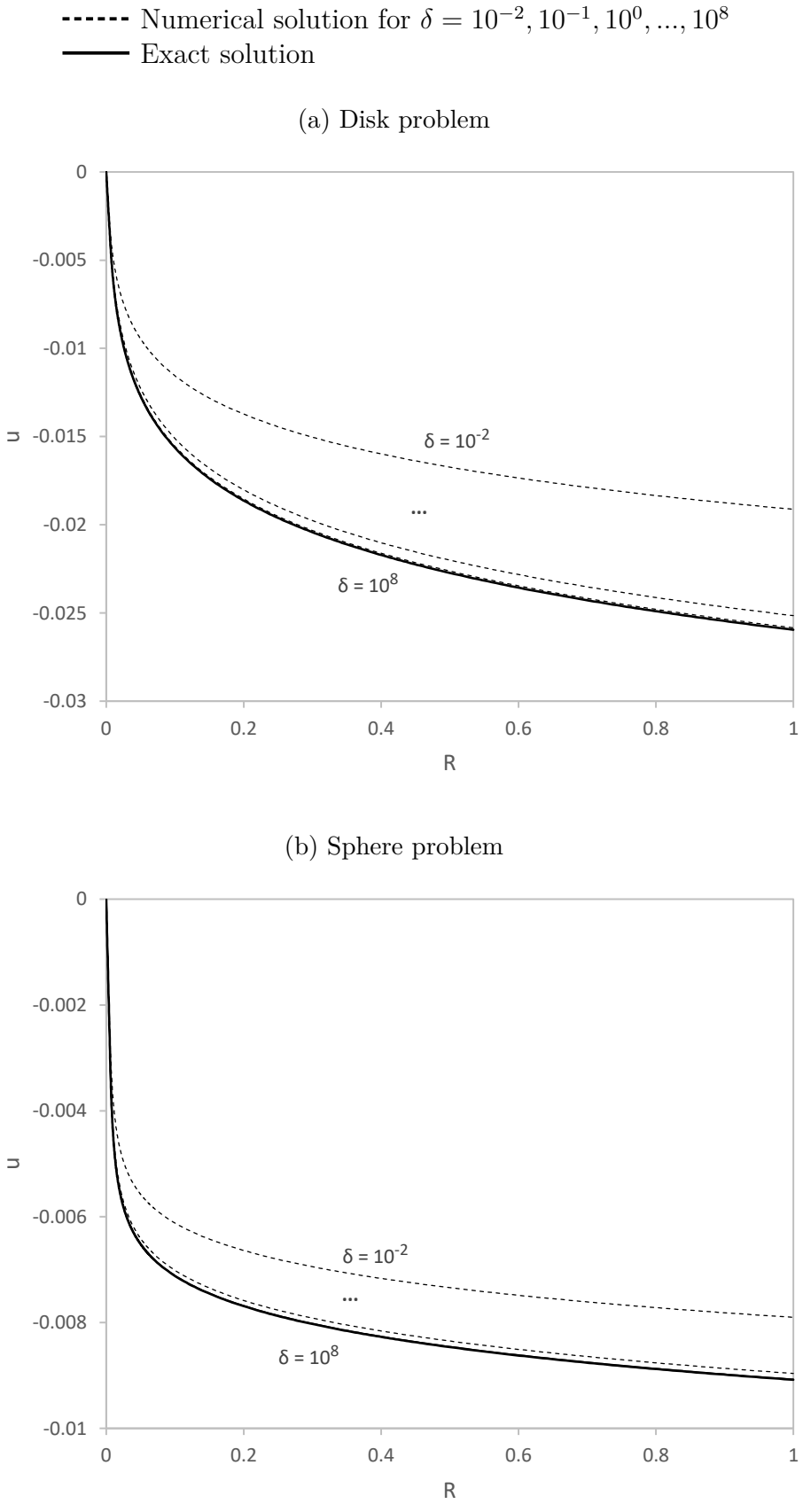

Source: The author.

Figure 14 – Determinant of the deformation gradient J versus radius $R \in (0, 1)$ for the constrained radially symmetric disk and sphere problems using 480 elements and $\delta = 10^8$.

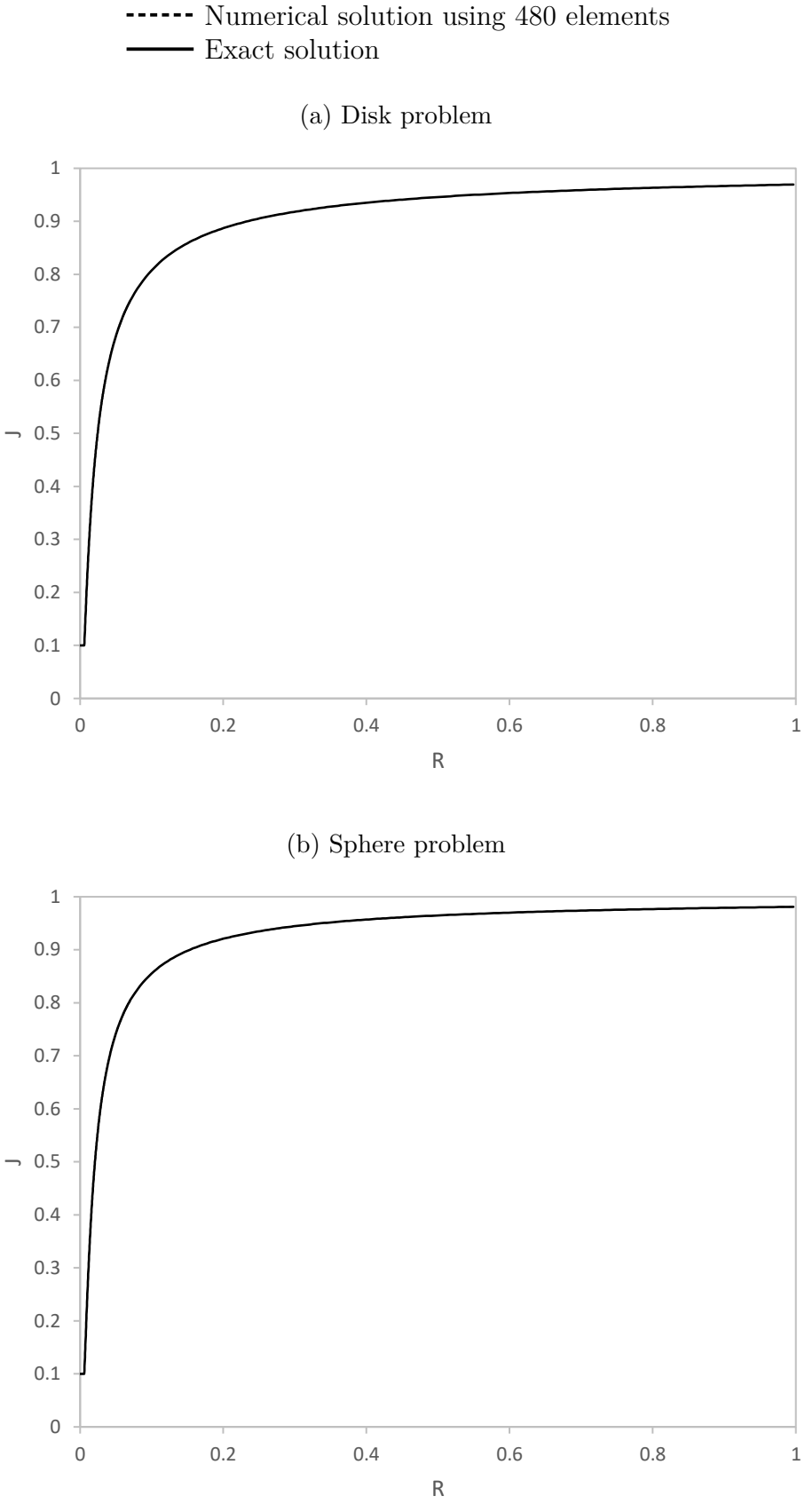

Source: The author.

Figure 15 – Determinant of the deformation gradient J versus radius $R \in (0, 0.05)$ for the constrained radially symmetric disk and sphere problems using 480 elements and $\delta = 10^8$.

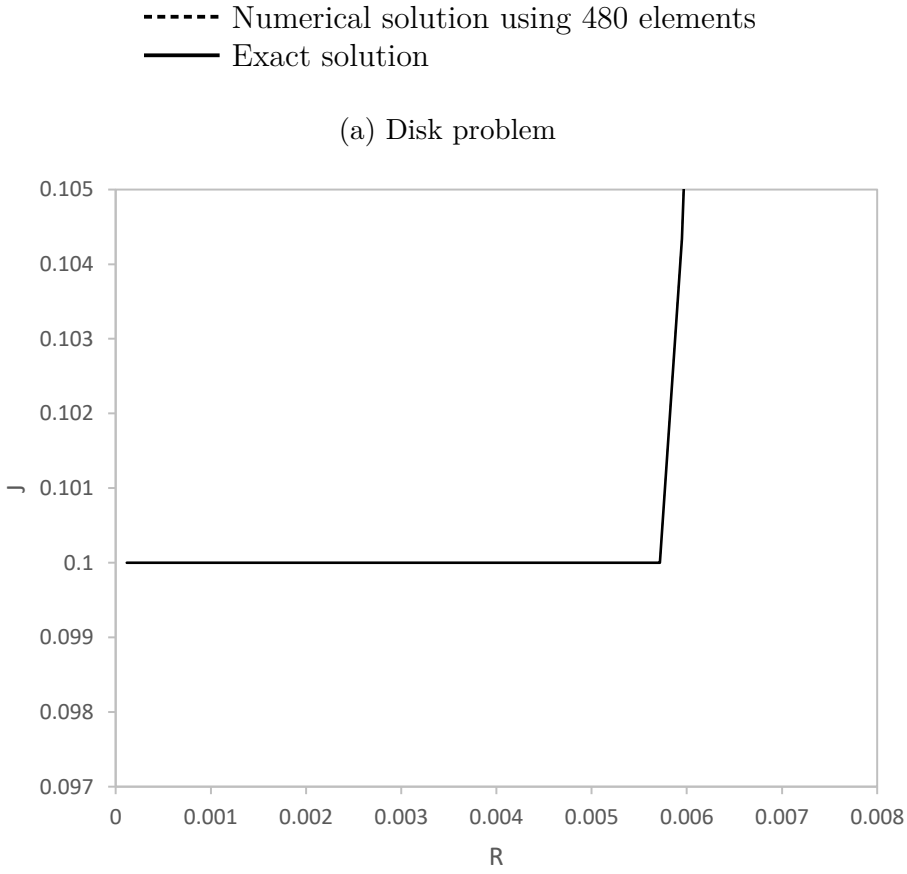

(a) Disk problem

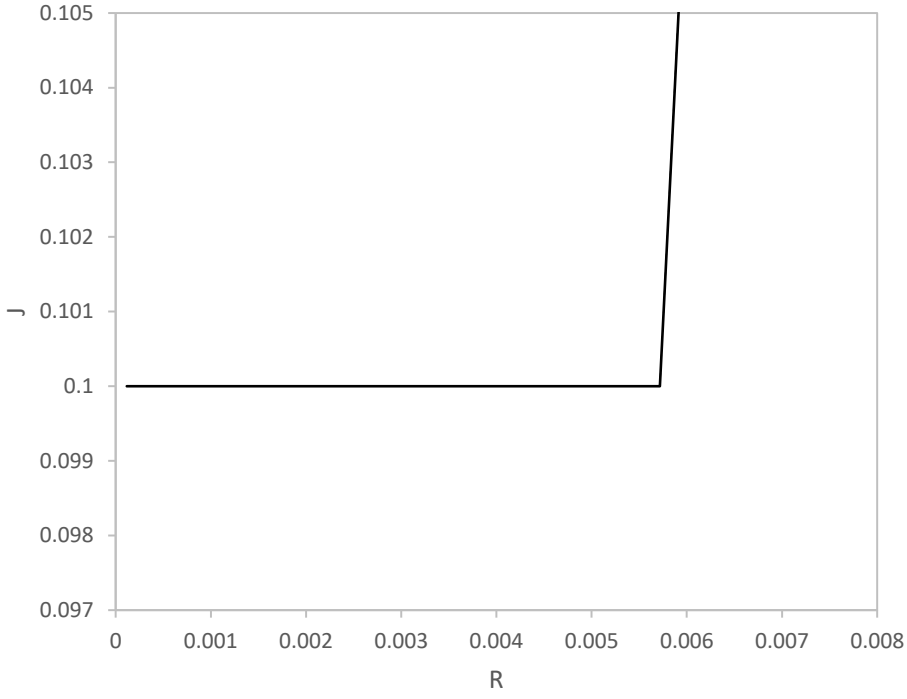

(b) Sphere problem

Source: The author.

numerical solution is slightly translated to the right when compared to ours. In addition, the curves of Aguiar (2006) in his Figure 9 are translated to the right when compared to our curves in Figure 16b. We confirmed numerically that these differences are due to how J is evaluated. In our work, we evaluate J at the center of the finite elements. However, Aguiar (2006) evaluated J at the mesh nodes, where the finite element approximation for u' is discontinuous, which renders J discontinuous as well. To solve this issue, the author calculated J as

$$J(R_i) \coloneqq \det(\mathbf{1} + \nabla \mathbf{u}(R_i\, \mathbf{e}_r)) = \left(1 + u'\left(\frac{R_i + R_{i-1}}{2}\right)\right)\left(1 + \frac{u(R_i)}{R_i}\right)^2, \tag{5.64}$$

where R_{i-1} and $R_i > R_{i-1}$ are the positions of two consecutive nodes belonging to the same finite element. The differences between his Figure 7 and our Figure 16b is also due to how we evaluate J since λ_δ is given by (4.4). We reproduced the same figures of Aguiar (2006) using (5.64), but they are not included in this work.

Figure 16 – Lagrange multiplier λ and its numerical approximations λ_δ versus radius $R \in (0, 0.01)$ obtained with $\delta = 10^8$ for the constrained radially symmetric disk and sphere problems.

------ Numerical approximation λ_δ using 128, 256, 512, 1024, and 480 elements
—— Exact Lagrange multiplier λ

(a) Disk problem

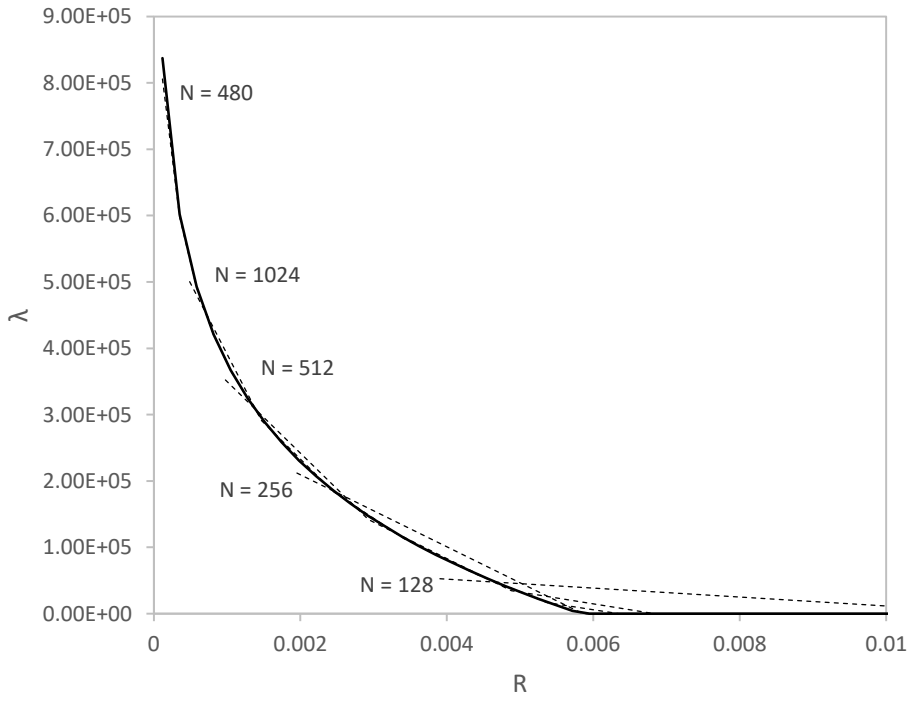

(b) Sphere problem

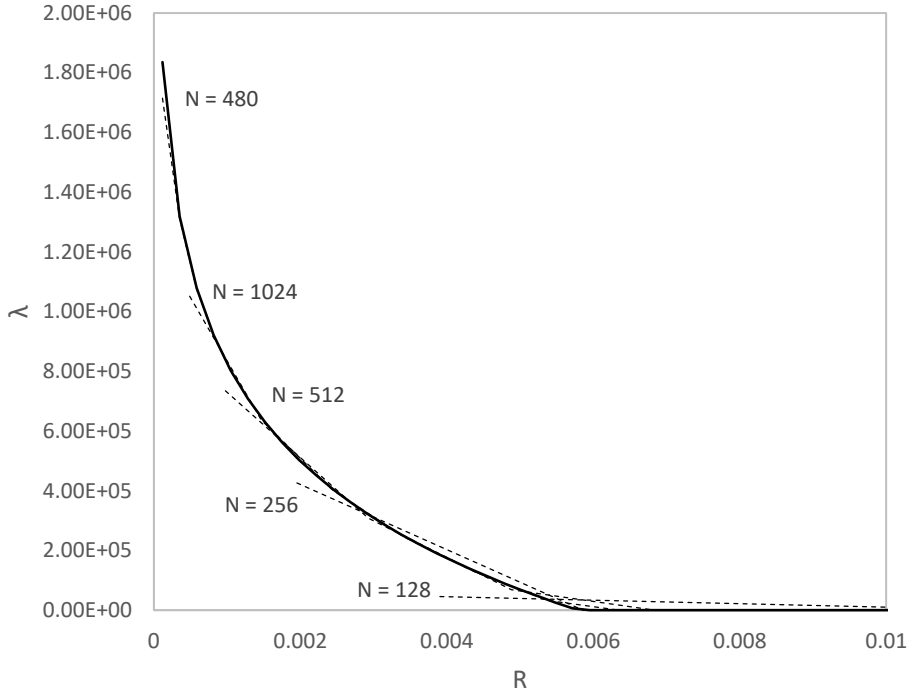

Source: The author.

6 ROTATIONALLY SYMMETRIC DISK PROBLEM

In this chapter we reconsider the constrained disk problem ($n = 2$) of the previous chapter and assume that the displacement field is rotationally symmetric, instead of radially symmetric, which allows us to search for radial and tangential displacements defined on a one-dimensional domain. We then obtain numerical results and compare them with computational results obtained by Fosdick, Freddi and Royer-Carfagni (2008), who also considered radial and tangential displacements, but defined in a two-dimensional domain. Moreover, we verify numerical convergence of approximate solutions and we investigate numerically the conditions for bifurcation from the radially symmetric solution given by (5.37) to the rotationally symmetric one. Finally, we obtain asymmetric solutions and analytical results that confirm this secondary solution.

6.1 Problem formulation

Similarly to Section 5.1, consider the constrained minimization problem defined by (3.62) and (3.63). Here, $\mathcal{B} \in \mathbb{R}^2$ corresponds to the undistorted reference configuration of a circular disk of radius R_e. The disk is in equilibrium with no body force and is subject to an imposed displacement $\bar{\mathbf{u}} = \bar{u}_r\,\mathbf{e}_r + \bar{u}_\theta\,\mathbf{e}_\theta$ on its entire external boundary $\partial\mathcal{B}$. Moreover, the displacement field is null at the center of the disk.

We assume that the displacement field is rotationally symmetric, i.e.,

$$\mathbf{u}(R,\Theta) = u_r(R)\,\mathbf{e}_r + u_\theta(R)\,\mathbf{e}_\theta. \tag{6.1}$$

We then have that the components of the infinitesimal strain tensor

$$\mathbf{E} = \epsilon_{rr}\,\mathbf{e}_r \otimes \mathbf{e}_r + \epsilon_{\theta\theta}\,\mathbf{e}_\theta \otimes \mathbf{e}_\theta + \epsilon_{r\theta}\,(\mathbf{e}_r \otimes \mathbf{e}_\theta + \mathbf{e}_\theta \otimes \mathbf{e}_r) \tag{6.2}$$

are given by

$$\epsilon_{rr} = u_r', \qquad \epsilon_{\theta\theta} = \frac{u_r}{R}, \qquad \epsilon_{r\theta} = \frac{1}{2}\left(u_\theta' - \frac{u_\theta}{R}\right), \tag{6.3}$$

where $(\cdot)' \coloneqq d(\cdot)/dR$. The stress tensor

$$\mathbf{T} = \sigma_{rr}\,\mathbf{e}_r \otimes \mathbf{e}_r + \sigma_{\theta\theta}\,\mathbf{e}_\theta \otimes \mathbf{e}_\theta + \sigma_{r\theta}\,(\mathbf{e}_r \otimes \mathbf{e}_\theta + \mathbf{e}_\theta \otimes \mathbf{e}_r) \tag{6.4}$$

is related to the strain tensor $\mathbf{E}$ by the Generalized Hooke's law in (3.60a), where the matrix representation of $\mathbb{C}$ in Voigt notation is given by (5.1). Thus, the stress components of (6.4) are given by

$$\begin{aligned} \sigma_{rr} &= c_{11}u_r' + c_{12}\frac{u_r}{R}, \\ \sigma_{\theta\theta} &= c_{12}u_r' + c_{22}\frac{u_r}{R}, \\ \sigma_{r\theta} &= c_{66}\left(u_\theta' - \frac{u_\theta}{R}\right). \end{aligned} \tag{6.5}$$

Because of the assumption of rotational symmetry of the displacement field in (6.1), the determinant of the deformation gradient becomes

$$\det(\mathbf{1}+\nabla\mathbf{u}) = (1+u_r')\left(1+\frac{u_r}{R}\right) + u_\theta'\,\frac{u_\theta}{R}. \tag{6.6}$$

Similarly to Section 5.1, it follows from (3.60a), (3.61), (6.2), and (6.4) that

$$\mathcal{E}[\mathbf{u}] = \frac{1}{2}\int_{\mathcal{B}} (\sigma_{rr}\,\epsilon_{rr} + \sigma_{\theta\theta}\,\epsilon_{\theta\theta} + 2\,\sigma_{r\theta}\,\epsilon_{r\theta})\,dV \tag{6.7}$$

and from (4.3) and (6.6) that

$$\mathcal{P}[\mathbf{u}] = \int_{\mathcal{B}} \frac{1}{(1+u_r')(1+u_r/R) + u_\theta'\,u_\theta/R - \varepsilon}\,dV. \tag{6.8}$$

Since $\mathcal{B}\in\mathbb{R}^2$, we have that $dV = R\,dR\,d\Theta$, which together with (6.3) and (6.5) allow us to write

$$\begin{aligned}\mathcal{E}[\mathbf{u}] = \frac{1}{2}\int_0^{2\pi}\int_0^{R_e} \Bigg[& c_{11}\,(u_r')^2 + 2c_{12}\,\frac{u_r}{R}\,u_r' + c_{22}\frac{u_r^2}{R^2} \\ & + c_{66}\,(u_\theta')^2 - 2c_{66}\,\frac{u_\theta}{R}u_\theta' + c_{66}\frac{u_\theta^2}{R^2}\Bigg] R\,dR\,d\Theta\end{aligned} \tag{6.9}$$

and

$$\mathcal{P}[\mathbf{u}] = \int_0^{2\pi}\int_0^{R_e} \frac{1}{(1+u_r')(1+u_r/R) + u_\theta'\,u_\theta/R - \varepsilon}\,R\,dR\,d\Theta. \tag{6.10}$$

After integrating on Θ, the expressions (6.9) and (6.10) become

$$\mathcal{E}[\mathbf{u}] = \pi\int_0^{R_e}\left[c_{11}\,R\,(u_r')^2 + 2c_{12}\,u_r\,u_r' + c_{22}\frac{u_r^2}{R} + c_{66}\,R\,(u_\theta')^2 - 2c_{66}\,u_\theta\,u_\theta' + c_{66}\frac{u_\theta^2}{R}\right] dR \tag{6.11}$$

and

$$\mathcal{P}[\mathbf{u}] = 2\pi\int_0^{R_e} \frac{R}{(1+u_r')\,(1+u_r/R) + u_\theta'\,u_\theta/R - \varepsilon}\,dR \tag{6.12}$$

respectively.

The constrained rotationally symmetric disk problem consists of determining a displacement field $\mathbf{u}$ with the form (6.1) for the constrained minimization problem defined by (3.62) and (3.63), where $\mathcal{E}$ in (3.62) is given by (6.11) and $\bar{\mathbf{u}} = \bar{u}_r\,\mathbf{e}_r + \bar{u}_\theta\,\mathbf{e}_\theta$ in (3.63). In Section 6.2, we use the numerical procedure described in Chapter 4, where the barrier functional $\mathcal{P}$ is given by (6.12), to determine numerical solutions for the constrained rotationally symmetric disk problem. In Section 6.3, we use the Euler-Lagrange equations (3.66) together with numerical solutions, such as those of Section 6.2, to determine an analytical solution for the constrained rotationally symmetric disk problem in $\mathcal{B}_>$.

6.2 Numerical results and discussion

6.2.1 The influence of the mesh and the initial guess

In order to obtain a bifurcation from the radially symmetric solution given by (5.37), Fosdick, Freddi and Royer-Carfagni (2008) used a low shear modulus and a very

refined mesh near the center of the disk. The characteristic size of the elements near the center is not specified, but the authors indicate that it is less than 10^{-7}. Here, we discuss mesh refinement near the center of the disk and leave to Section 6.2.3 a discussion about the influence of the shear modulus on the numerical results.

Recall from Section 2.3 that Fosdick, Freddi and Royer-Carfagni (2008) considered a two-dimensional domain and a circular mesh composed of biquadratic finite elements, whose deformed configuration can be seen in Figure 8. Here, we consider a one-dimensional domain, because of the assumption of rotationally symmetric displacement field in (6.1), and linear finite elements. Thus, in order to investigate the influence of the mesh refinement near the center of the disk, we consider the following assumptions about the mesh:

1. The first element, i.e., the one nearest to the center of the disk, has a length h_0. Below, we consider the sequence $\{10^{-6}, 10^{-7}, 10^{-8}, 10^{-9}, 10^{-10}\}$ for the parameter h_0.

2. The length of the next elements follows a geometric progression with common ratio equals to 2, until the length is greater than 10^{-3}, i.e., $h_{i+1} = 2\,h_i$ until $h_{i+1} > 10^{-3}$.

3. From there on, the mesh becomes uniform and the elements have a length slightly[1] greater than 10^{-3}.

Note from the above assumptions that, as h_0 decreases, the mesh becomes more refined near the center of the disk. In addition, numerical experiments indicate that the value 10^{-3}, used as an upper bound of the geometric progression in Assumption 2 above and as an approximate element size in the region where the mesh is uniform in Assumption 3, represents a good balance between solution precision and computational cost. This value is also not very different from the element size considered by Fosdick, Freddi and Royer-Carfagni (2008) for the elements that are far from the center of the disk.

We have chosen the same material and geometric parameters used by Fosdick, Freddi and Royer-Carfagni (2008) in their investigation of a bifurcation solution from the radially symmetric solution (5.37), that is, $\bar{u}_r \coloneqq \bar{\mathbf{u}} \cdot \mathbf{e}_r = -0.05$, $\bar{u}_\theta \coloneqq \bar{\mathbf{u}} \cdot \mathbf{e}_\theta = 0$, $c_{11} = 10^5$, $c_{22} = 10^4$, $c_{12} = 10^3$, $c_{66} = 10^3$, $\varepsilon = 0.1$, and $R_e = 1$.

For the numerical parameters, we have chosen $\varepsilon_{\mathbf{s}} = 10^{-12}$ in (4.12), $\varepsilon_\alpha = 10^{-12}$ and $N_\alpha = 50$ in (4.18), and the sequence $\{10^{-6}, 10^{-5}, 10^{-4}, 10^{-3}, ..., 10^{8}\}$ for the penalty parameter δ in (4.7). Again, our numerical experiments have confirmed that the numerical results do not change significantly for $\delta > 10^8$.

[1] Consider that the region where the element lengths follow a geometric progression is $0 < R < R_g$. Then, the region $R_g < R < R_e$ is discretized by a uniform mesh of N elements, where N is the integer part of $(R_e - R_g)/0.001$.

The choice of the initial solution used in the numerical procedure is important. First, we consider that this solution is the solution of the Lekhnitskii problem for an isotropic material, for which $k = 1$ and $\mathbf{u} = (R/R_e)\,\bar{\mathbf{u}}$. This solution yields the initial guess $\mathbf{s}_0$ through (4.6), where, here, $m = 2\,M$ with M being the number of mesh nodes. In this respect, the components of $\mathbf{s}_0$ are $s_0^{2\,i-1} \coloneqq \mathbf{u}(R_i) \cdot \mathbf{e}_r$ and $s_0^{2\,i} \coloneqq \mathbf{u}(R_i) \cdot \mathbf{e}_\theta$, where $i = 1, 2, 3, ..., M$ and R_i denotes the position of the i-th node. Using this initial guess, which was also used by Fosdick, Freddi and Royer-Carfagni (2008), we only obtain the radially symmetric solution, regardless of the value of h_0.

To obtain a rotationally symmetric solution, we introduce a perturbation u_θ^0 in the tangential displacement. Specifically, all components of the initial guess $\mathbf{s}_0$ associated to the tangential displacement are set equal to u_θ^0, except for the components associated with the first and last nodes in the interval $(0, R_e)$. We then have that $s_0^{2\,i} = u_\theta^0$, $i = 2, 3, 4, \ldots, M-1$, where $R_1 = 0$ and $R_M = R_e$. To highlight the importance of this perturbation, we considered three different values for u_θ^0, which are 10^{-15}, 10^{-10} and 10^{-5}.

The interior penalty method requires that the initial solution must satisfy the local injectivity constraint. It is not immediately clear, if the perturbed initial solution we use is locally injective. In fact, large values of u_θ^0 can make the initial solution violate the constraint, especially for fine meshes. Therefore, we check for this violation at all quadrature points before we start the search procedure.

For the first value $u_\theta^0 = 10^{-15}$, we obtained again only the radially symmetric solution regardless of the value of h_0. For the second value $u_\theta^0 = 10^{-10}$, we obtained a rotationally symmetric solution for the meshes related to $h_0 = 10^{-8}$, $h_0 = 10^{-9}$, and $h_0 = 10^{-10}$, and the radially symmetric solution for the other values of h_0. For the third and largest value $u_\theta^0 = 10^{-5}$, we obtained a rotationally symmetric solution for all meshes.

Finally, numerical experiments considering intermediate values of u_θ^0 and other values of h_0 indicate that there is a minimum value of u_θ^0, which decreases as the mesh is refined, that yields convergence of the numerical procedure to a rotationally symmetric solution. In addition, greater values of u_θ^0 do not modify the rotationally symmetric solution obtained. In the next section we present the form of this rotationally symmetric solution and results regarding numerical convergence.

6.2.2 Study of numerical convergence

The sequence of meshes considered in Section 6.2.1 was used to discuss the necessity of a very fine mesh near the center of the disk to obtain a secondary solution for the constrained rotationally symmetric disk problem. However, these meshes are very fine, and convergence results would not be visually evident in the graphs. Therefore, to better visualize the numerical convergence of the rotationally symmetric solution mentioned in the previous section, we use a sequence of uniform meshes with N linear finite elements, where

$N \in \{256, 1024, 4096, 16384, 65536\}$, and the same material, geometric and numerical parameters of Section 6.2.1, except for the sequence of penalty parameters, which is now given by the sequence $\{10^{-3}, 10^{-2}, 10^{-1}, 10^{0}, ..., 10^{8}\}$. Again, our numerical experiments have confirmed that the numerical results do not change significantly for $\delta > 10^8$. Observe that, here, the initial penalty parameter $\delta_0 = 10^{-3}$ is considerably larger than the value used in Section 6.2.1, which is 10^{-6}. This is because, in the process of obtaining the results of Section 6.2.1, the numerical procedure has had convergence difficulties for larger values of δ_0 after the introduction of the perturbation u_θ^0. In Section 6.2.6, we discuss more about these difficulties.

Recall from Section 6.2.1 that a perturbation u_θ^0 in the tangential displacement of the initial displacement field was necessary to obtain the rotationally symmetric solution, for otherwise only the radially symmetric solution would be obtained. Here, we use $u_\theta^0 = 10^{-5}$, because it was the minimum perturbation necessary to obtain the rotationally symmetric solution for the mesh with 256 elements. This value could be reduced for the other more refined meshes.

In Figure 17 we show curves for the radial displacement u_r obtained from each one of the five meshes for a fixed large penalty parameter δ. Figure 17a refers to the entire interval $(0, R_e)$ and Figure 17b refers to a vicinity of the origin. We see from these figures that the sequence of approximate solutions converge to a limit function. In the next figure we show that this function is very close to the unconstrained solution given by (5.28).

In Figure 18 we show the radial displacement of the numerical solution obtained with $N = 65536$, the unconstrained solution given by (5.28), and the radially symmetric solution given by (5.37). Similarly as before, Figure 18a refers to the entire interval $(0, R_e)$, where we recall from above that $R_e = 1$, and Figure 18b refers to a vicinity of the origin. We see from these figures that the numerical solution is very close to the unconstrained solution. We will see bellow that, as c_{66} increases, the numerical solution approaches the constrained radially symmetric solution.

In Figure 19 we show the field $r(R) - R$, where

$$r(R) \coloneqq \sqrt{(R + u_r)^2 + u_\theta^2}, \tag{6.13}$$

of the numerical solution obtained with $N = 65536$ (solid line), the unconstrained solution given by (5.28) (dash-dotted line), and the radially symmetric solution given by (5.37) (dashed line). Since $u_\theta = 0$ in the last two cases, we see from (6.13) that $r(R) - R \equiv u_r(R)$. Again, we present this result in two scales, so that, Figure 19a refers to the entire interval $(0, R_e)$ and Figure 19b refers only to a neighborhood of the origin. We see from Figure 19a that, away from the origin, the field $r(R) - R$ of the rotationally symmetric solution is very close to the unconstrained solution. We will see in Section 6.2.3, that this field approaches the radially symmetric solution as c_{66} increases. In Figure 19b, we see that, as

Figure 17 – Radial displacement u_r versus radius R in (a) $(0, 1)$ and (b) $(0, 0.05)$ for the rotationally symmetric solution using uniform meshes with 256, 1024, ..., 65536 elements and for $\delta = 10^8$.

(a) Entire interval

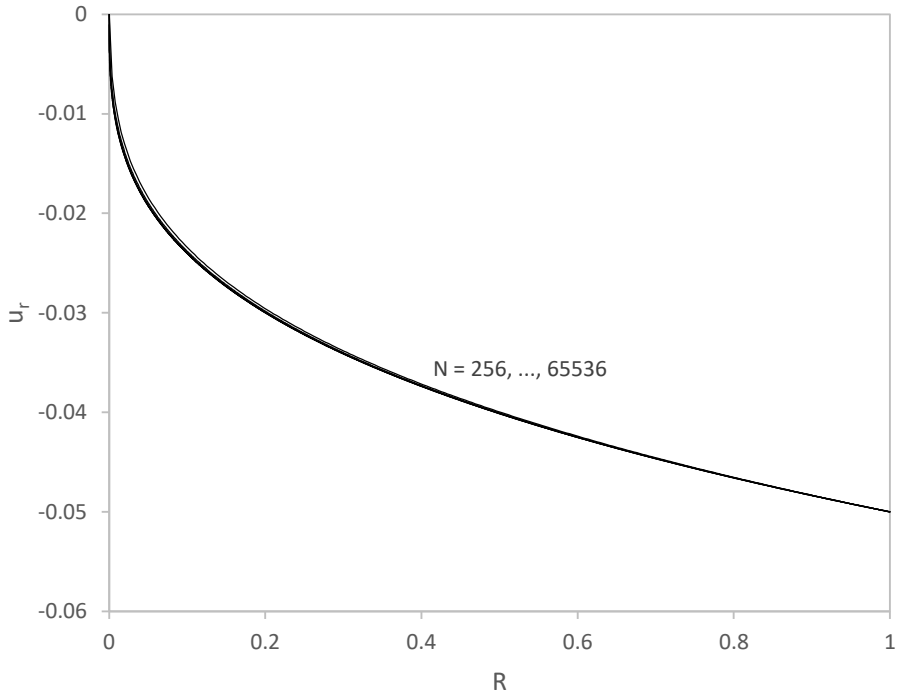

(b) Neighborhood of the origin

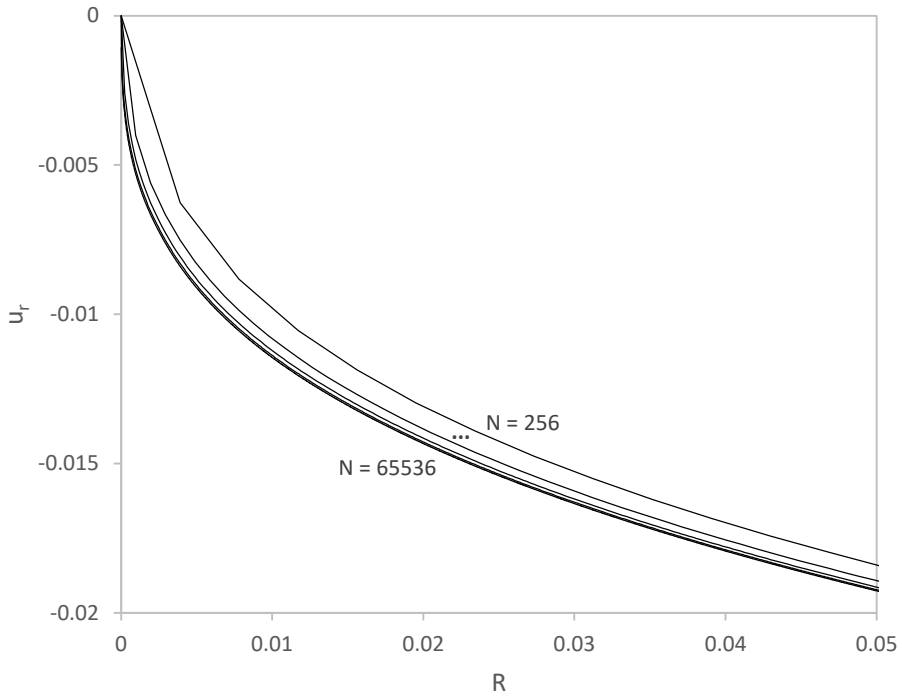

Source: The author.

Figure 18 – Radial displacement u_r versus radius R in (a) $(0, 1)$ and (b) $(0, 0.05)$ for ...

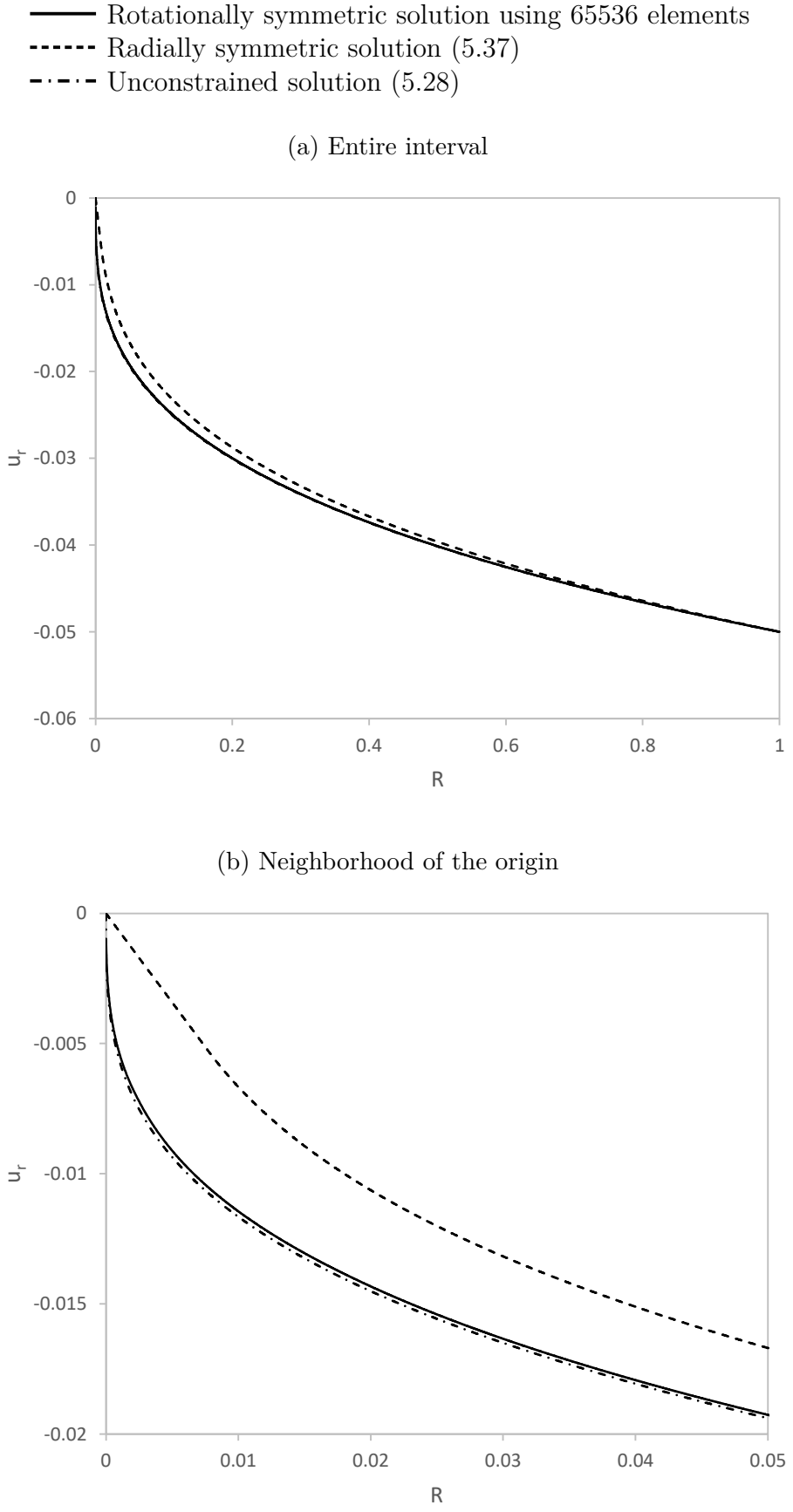

Source: The author.

R increases, the field $r(R) - R$ increases, reaching a positive maximum value, and then decreases monotonically, with its curve lying between the curves of the unconstrained and the radially symmetric solutions.

Comparing our Figure 19b with Figure 3b of Fosdick, Freddi and Royer-Carfagni (2008), we see that, away from the origin, the field $r(R) - R$ of their asymmetric solution is closer to the radially symmetric solution and has a maximum positive value that is lower than ours. In our case, this maximum value is about 0.0034 and, in their case, it is about 0.0015. In both cases these values seem to be reached at the same radius.

In Figure 20 we show curves for the tangential displacement u_θ obtained from the five uniform meshes and a fixed large penalty parameter δ. The results are presented in two scales, so that Figure 20a refers to the entire interval $(0, R_e)$ and Figure 20b refers to a vicinity of the origin. We see from Figure 20b that the numerical approximations of u_θ converge to a limit function as the number of elements N increases and that this limit function is linear near the center of the disk, increases nonlinearly as R increases, reaches a maximum value at approximately $R = 0.015$, and then decreases monotonically for larger values of R. In the region where the limit function is linear we have used 144 elements for the most refined mesh of 65536 elements. In Section 6.3 we find analytical expressions that confirm this linear behavior near the origin.

The above results are qualitatively similar to the corresponding results presented by Fosdick, Freddi and Royer-Carfagni (2008) in their Figure 9. We see, however, that the maximum value of u_θ is approximately 0.0065 in Figure 20 and 0.0036 in their Figure 9. Also, it is not clear from their figure that u_θ behaves linearly in a vicinity of the center of the disk. In fact, u_θ seems to be negative very close to this center.

In Figure 21 we show curves for the angle of rotation φ of a material particle $\mathbf{X}$ from its original position $\mathbf{X} = R\,\mathbf{e}_r$ to its final position $\mathbf{x} = (R + u_r)\,\mathbf{e}_r + u_\theta\,\mathbf{e}_\theta$, as illustrated in Figure 22. We then have that

$$\varphi = \arctan\left(\frac{u_\theta}{R + u_r}\right) . \tag{6.14}$$

Similarly as before, Figure 21a refers to the entire interval $(0, R_e)$ and Figure 21b refers to a vicinity of the origin. We see from the graphs of Figure 21 that the numerical approximations of φ converge to a limit function as the number of elements N increases and that this limit function tends to π as $R \to 0$. This result is somewhat different from the results found by Fosdick, Freddi and Royer-Carfagni (2008). In the analysis of their Figure 10 they observe that "the angle of rotation of a core of small radius is nominally π". As Figure 21 seems to suggest, this angle is π only at the center of the disk and then decreases as the radius R increases.

In Figure 23 we show the determinant of the deformation gradient $J := \det(\mathbf{1} + \nabla\mathbf{u})$ for a fixed large penalty parameter and the entire interval $(0, R_e)$. The solid lines refer

Figure 19 – Field $r(R) - R$ versus radius R in (a) $(0, 1)$ and (b) $(0, 0.05)$ for ...

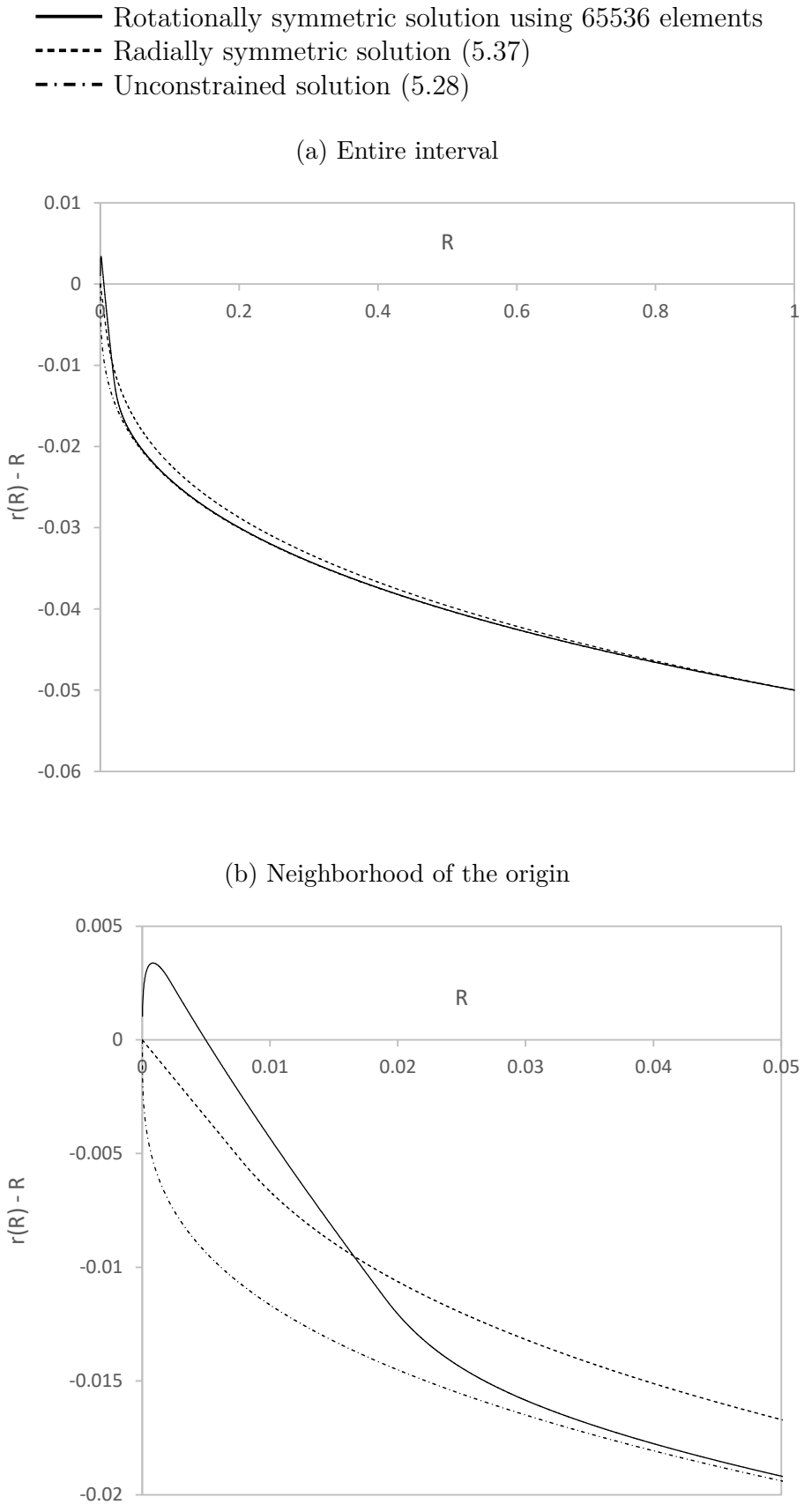

Source: The author.

Figure 20 – Tangential displacement u_θ for the rotationally symmetric solution obtained numerically using $256, 1024, ..., 65536$ elements and for $\delta = 10^8$.

(a) Entire interval

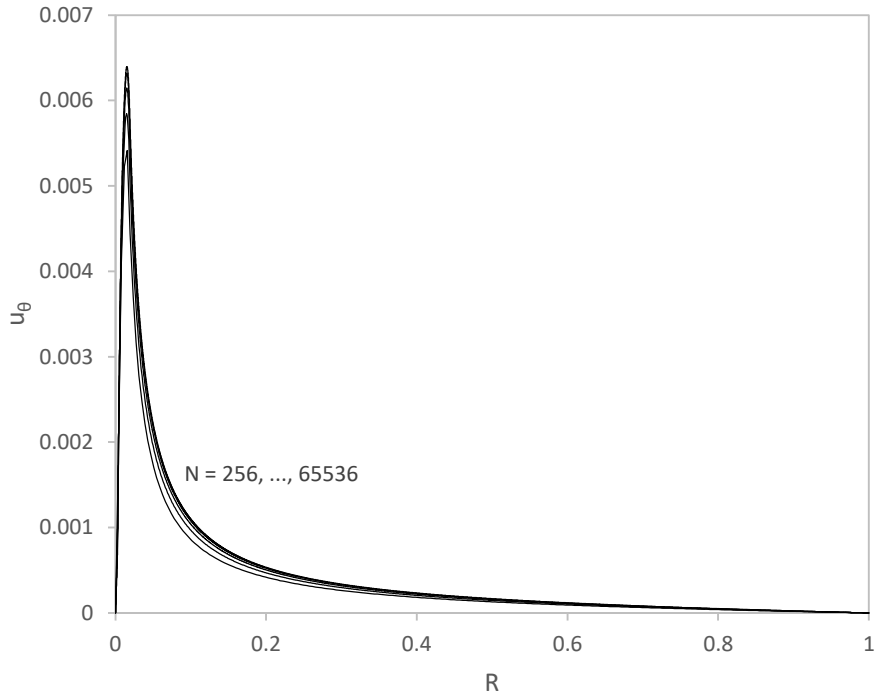

(b) Neighborhood of the origin

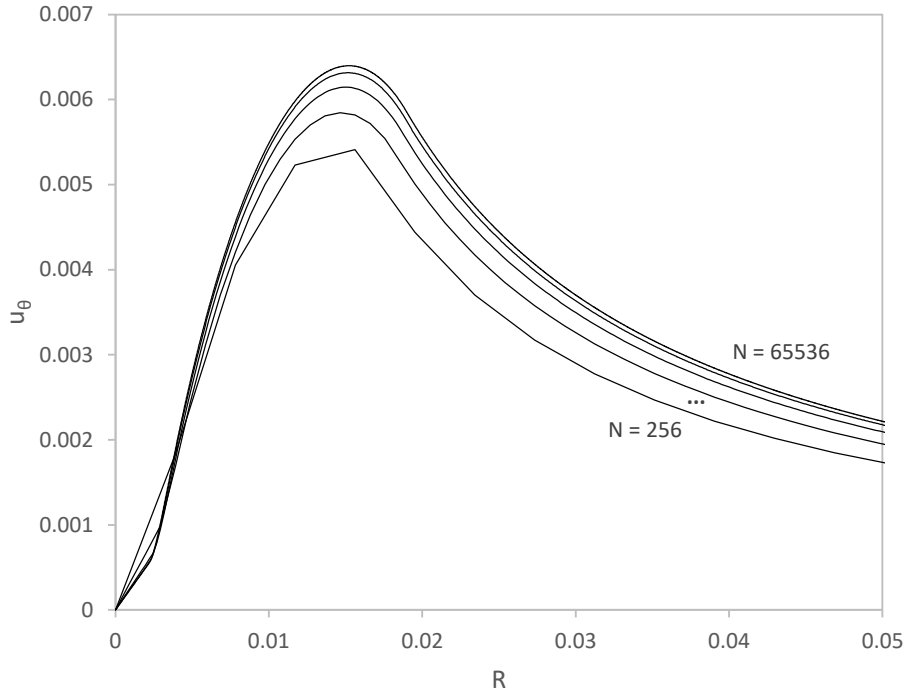

Source: The author.

Figure 21 – Angle of rotation φ for the rotationally symmetric solution obtained numerically using $256, 1024, ..., 65536$ elements and $\delta = 10^8$.

(a) Entire interval

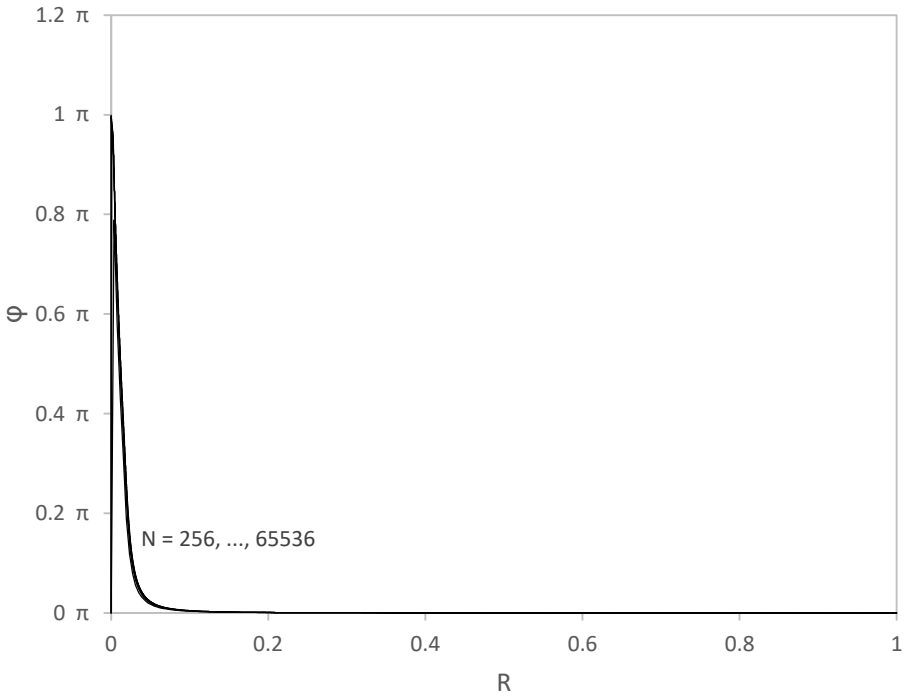

(b) Neighborhood of the origin

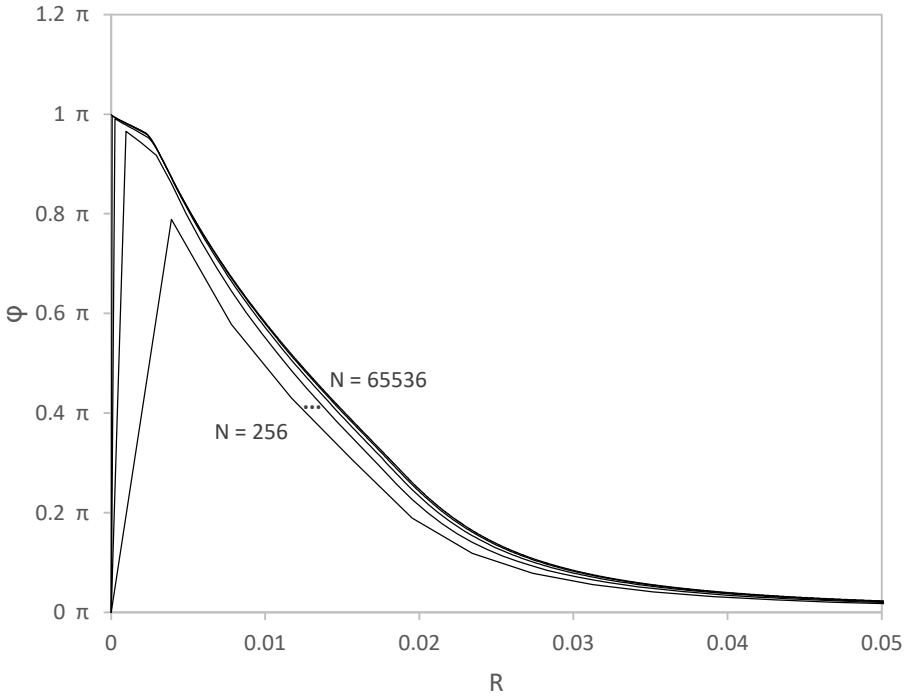

Source: The author.

Figure 22 – Displacement components and angle of rotation

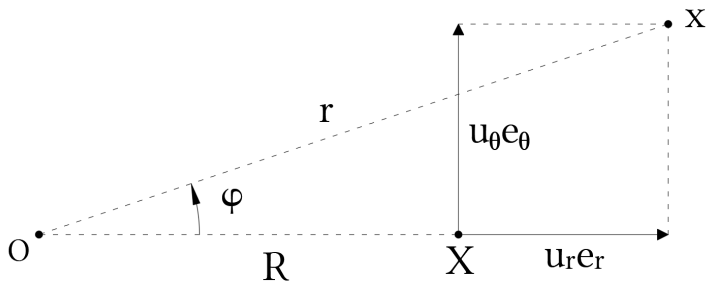

Source: The author.

Figure 23 – Determinant of the deformation gradient J for the rotationally symmetric solution with $\delta = 10^8$ and for the radially symmetric solution in $(0, 1)$.

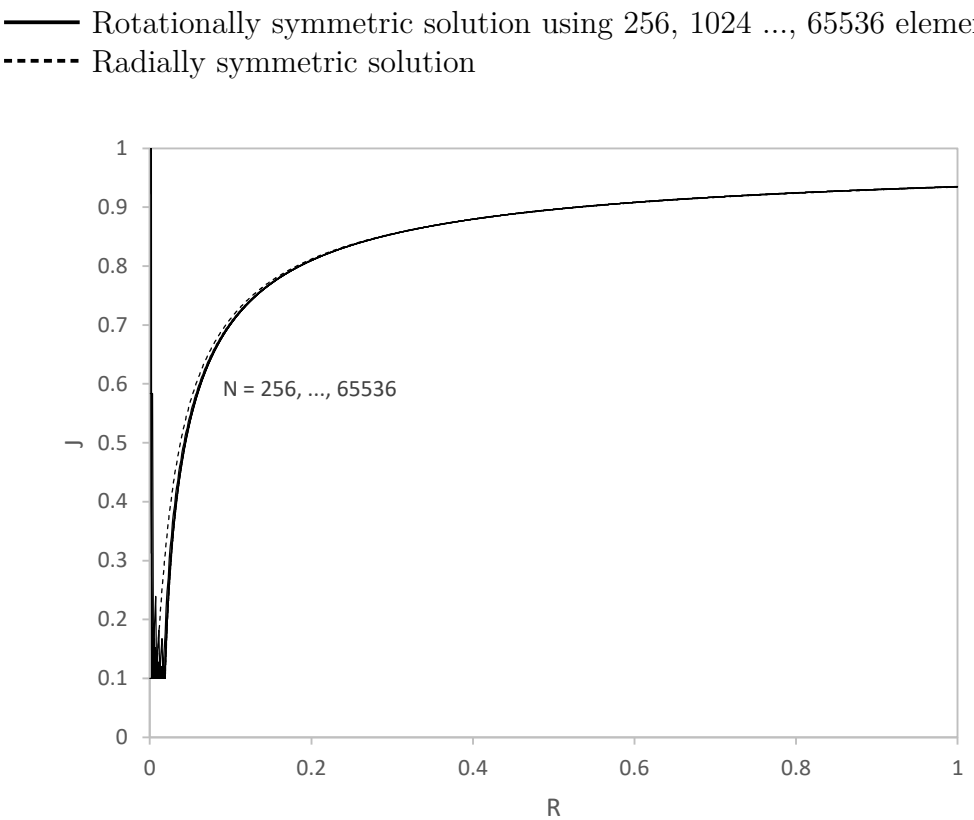

Source: The author.

to the numerical solutions and the dashed line refers to the expression (5.42), which is calculated from the radially symmetric solution given by (5.37). We see from this figure that the curves become indistinguishable as we move away from the origin.

To investigate the behavior of J near the center of the disk, we show in Figure 24 a sequence of graphs of J versus $R \in (0, 0.05)$ obtained from numerical solutions for

Figure 24 – Determinant of the deformation gradient J for the rotationally symmetric solution with $\delta = 10^8$ and for the radially symmetric solution in $(0, 0.05)$.

(a) 256 elements

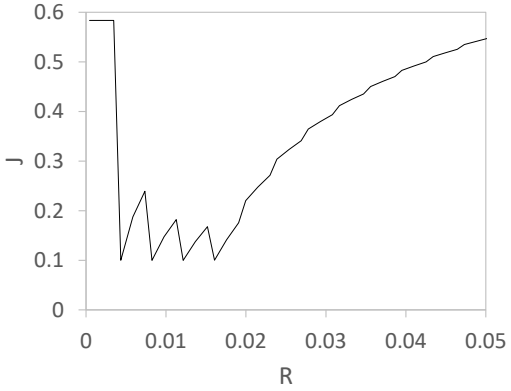

(b) 1024 elements

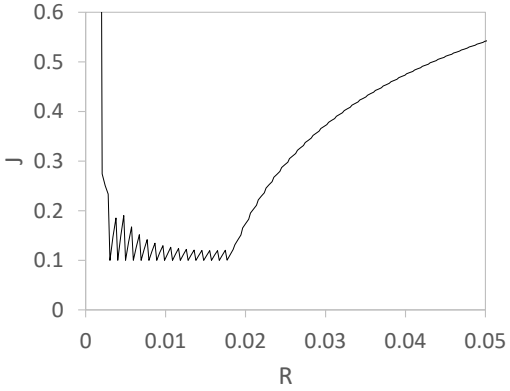

(c) 4096 elements

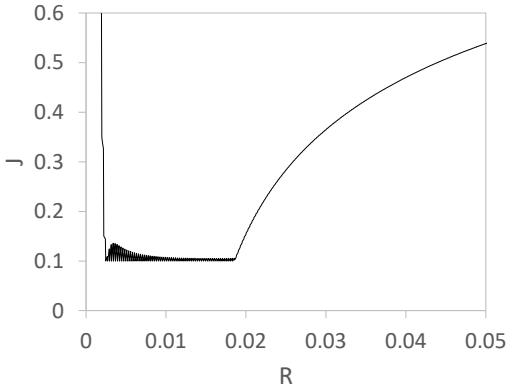

(d) 16384 elements

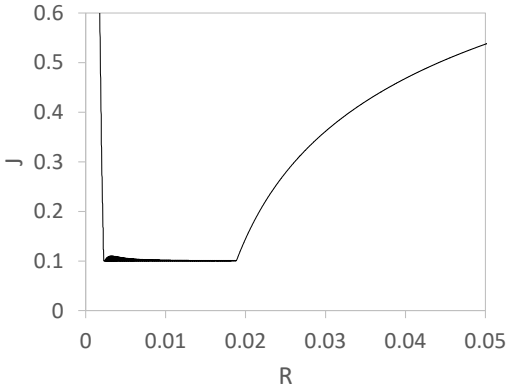

(e) 65536 elements

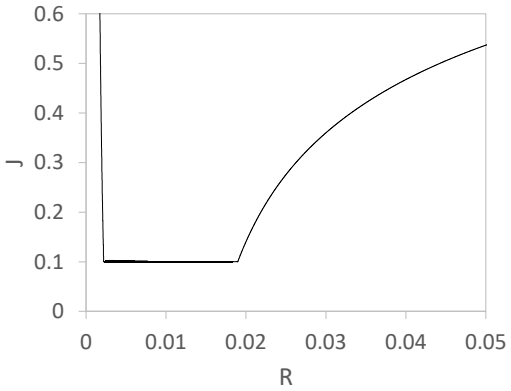

(f) Radially symmetric solution

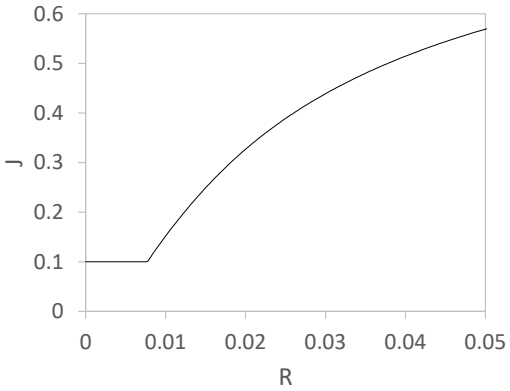

Source: The author.

increasing values of N, which corresponds to Figures 24a-e, and from the radially symmetric solution, which corresponds to Figure 24f. To construct these curves, we evaluated the determinant at all quadrature points used in the numerical integrations, which, recall from Section 4.2, are three in each mesh element. We see from Figures 24a-e that, as we approach the center of the disk, J decreases, oscillates above 0.1 in the interval $(0.0022, 0.0190)$, and increases sharply for $R \leq 0.0022$, which indicates that it is singular at $R = 0$. As N increases, the amplitudes of the oscillations decrease and J becomes $\varepsilon = 0.1$. These oscillations are due to the facts that J is evaluated at the integration points inside each element and that the fields u_r and u_θ in (6.6) are approximated by linear functions, which have discontinuous derivatives across the boundaries of the elements.

We also see from Figures 24a-e that the active zone of the rotationally symmetric solution, where $J = \varepsilon$, corresponds to an annular region of the disk with inner radius $R_a \approx 0.0022$ and outer radius $R_b \approx 0.0190$, as opposed to the central core of radius $R_c \approx 0.0077$ predicted by the radially symmetric solution shown in Figure 24f. In addition, R_a coincides with the radius below which u_θ is linear in Figure 20. In Section 6.3, we show that, if the active zone is an annular region, then u_θ must be linear inside the circular region of radius R_a.

It is clear from (4.4) and Figure 24 that oscillations of $J \coloneqq \det(\mathbf{1} + \nabla \mathbf{u})$ generate oscillations in the approximation λ_δ of the Lagrange multiplier, which are amplified by the factor $1/\delta$. On the other hand, we have verified that, in the active zone, the determinant calculated at the first quadrature point of each element is the closest to 0.1 when compared to its value at the second and third quadrature points. Using the previous two observations, we have calculated λ_δ using (4.4) together with the value of J at the first quadrature point of each finite element. In Figure 25 we show λ_δ versus $R \in (0, 0.05)$ for large penalty parameter δ and different values of N. We see from this figure that λ_δ converges to a limit function as N increases, takes large, but finite values inside the active region, where $J = \varepsilon$, and vanishes outside this region, as expected.

The above results are in good qualitative agreement with results shown in Figure 18 of Fosdick, Freddi and Royer-Carfagni (2008). Quantitatively, the results are of the same order of magnitude, with the maximum value of λ_δ in Figure 25 being close to 10600 for the most refined mesh and close to 9000 in Figure 18 of Fosdick, Freddi and Royer-Carfagni (2008). A possible explanation for this difference may be inferred from the analysis of Figure 25, where we see that the maximum values of λ_δ vary considerably with N.

6.2.3 The influence of shear stiffness c_{66}

The exposition above is focused on the convergence of the numerical scheme with respect to mesh refinement keeping all the other parameters fixed. Now, we vary the

Figure 25 – Approximation λ_δ of the Lagrange multiplier for the rotationally symmetric solution using $256, 1024, ..., 65536$ elements and $\delta = 10^8$.

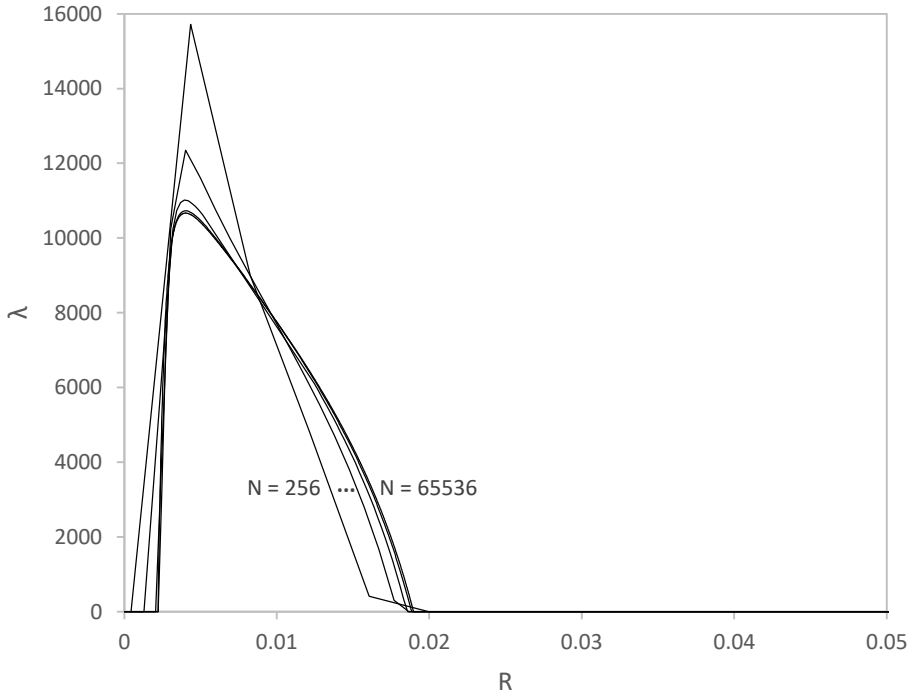

Source: The author.

values of the elastic constant c_{66} and hold fixed the values of all the other parameters, including the number of finite elements. We consider that c_{66} takes a value in the sequence $\{10^3, 5 \times 10^3, 10^4, 5 \times 10^4, 10^5\}$. Regarding the mesh, to reduce the computational cost of the study, we do not use uniform meshes, but a non-uniform mesh composed of $600\,q$ elements distributed in three intervals: $375\,q$ elements in $0 < R < 0.07\,R_e$, $125\,q$ elements in $0.07\,R_e < R < 0.46\,R_e$ and $100\,q$ elements in $0.46\,R_e < R < R_e$. For now, we consider $q = 16$, which yields a total of 9600 elements.

Except for c_{66}, we have chosen the same material, geometric and numerical parameters used in Section 6.2.2. We also consider the same perturbation $u_\theta^0 = 10^{-5}$, because it is the minimum perturbation necessary to obtain the rotationally symmetric solution for $c_{66} = 10^5$. Recall from Section 6.2.1 that smaller values of u_θ^0 yield radially symmetric solutions only and larger values do not modify the rotationally symmetric solutions provided that the initial candidate for minimizer is locally injective.

In Figures 26 and 27 we show the numerical approximations of, respectively, the radial, u_r, and the tangential, u_θ, displacements in two scales for different values of c_{66}. For comparison, we also present the radially symmetric and the unconstrained solutions in Figure 26, which have null tangential displacements. We see from Figure 26 that the

numerical approximation of u_r for $c_{66} = 10^3$ is very close to the unconstrained solution. As this stiffness increases, the numerical approximation of u_r tends to the radially symmetric solution, being very close to this solution, when we consider the case $c_{66} = 10^5$. Observe from Figure 26b the abrupt change of behavior in the curves as we go from $c_{66} = 10^4$ to $c_{66} = 5 \times 10^4$. In spite of this behavior, numerical experiments have shown nothing special about the behavior of the solution for $c_{66} \in (10^4, 5 \times 10^4)$.

In Figure 27 we observe the influence of the shear elastic modulus c_{66} on the tangential displacement u_θ and, in particular, on its maximum value. We see from both Figure 27a and Figure 27b that the larger the value of c_{66} the smaller the maximum value of u_θ. This observation combined with previous observations about Figure 26 indicate that a large value of c_{66} hinders the rotation of the disk core and, as a consequence, the rotationally symmetric field (6.1), obtained numerically, tends to the radially symmetric field $u\,\mathbf{e}_r$, with u obtained analytically and given by (5.37). As in Figure 26, here again, we observe an abrupt change between the curves corresponding to $c_{66} = 10^4$ and $c_{66} = 5 \times 10^4$.

Fosdick, Freddi and Royer-Carfagni (2008) present in their Figure 19 the field $u_\theta(R)$ obtained with different values of c_{66} between 1 and 2×10^4. They notice that their "numerical experiments have shown that the threshold value of c_{66} that marks the transition from the symmetric to the asymmetric solution is approximately 2×10^4". Based on the exposition above, our numerical experiments show, however, that u_θ is still nonzero for $c_{66} > 2 \times 10^4$. In the end of the present section, we discuss this threshold value.

In Figure 28 we show the field $r(R) - R$, where $r(R)$ is given by (6.13), of the numerical solution obtained with different values of c_{66}, the unconstrained solution given by (5.28) and the radially symmetric solution given by (5.37). As before, we present this result in two scales. We see from this figure that, far from the origin, the field $r(R) - R$ of the rotationally symmetric solution obtained with $c_{66} = 10^3$ is very close to the unconstrained solution and, as c_{66} increases, it approaches the radially symmetric solution. Next to the origin, the maximum positive value of the field $r(R) - R$ increases as c_{66} decreases. Again, we see the abrupt change between the curves of $c_{66} = 10^4$ and $c_{66} = 5 \times 10^4$.

In Figure 29 we show the angle of rotation φ, defined in (6.14), for increasing values of c_{66}. We see from both Figure 29a and Figure 29b that φ starts at π and becomes monotonically decreasing for increasing values of R keeping c_{66} fixed and for increasing values of c_{66} keeping R fixed. As in previous figures, again, there is a sharp transition in the curves for c_{66} between 10^4 and 5×10^4.

In Figure 30 we show the determinant of the deformation gradient, $J \coloneqq \det(\mathbf{1}+\nabla\mathbf{u})$, plotted against $R \in (0, 1)$ for increasing values of c_{66}. Similar to the discussion about oscillatory behavior of the graphs shown in Figure 24, here, we also evaluate J at all the quadrature points. Given the scale of the graph and the mesh refinement, we see no oscillatory behavior in this figure. Except for the oscillatory behavior of J in Figure

Figure 26 – Radial displacement u_r for the rotationally symmetric solution for increasing values of c_{66} and for $\delta = 10^8$.

——— Rotationally symmetric solution for $c_{66} = 10^3, 5 \times 10^3, 10^4, 5 \times 10^4, 10^5$
------ Radially symmetric solution (5.37)
-·-·- Unconstrained solution (5.28)

(a) Entire interval

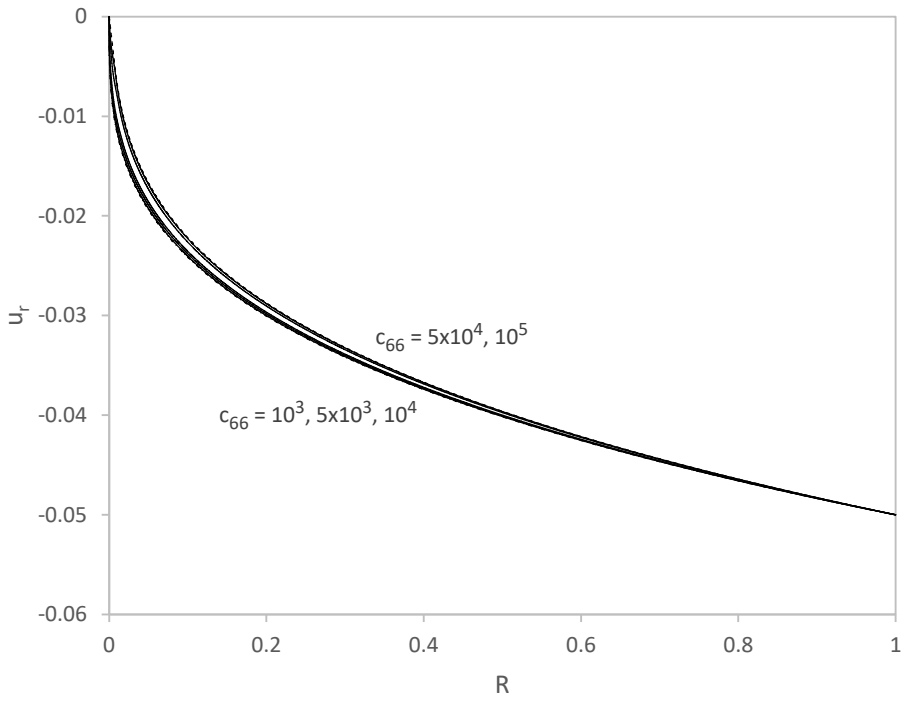

(b) Neighborhood of the origin

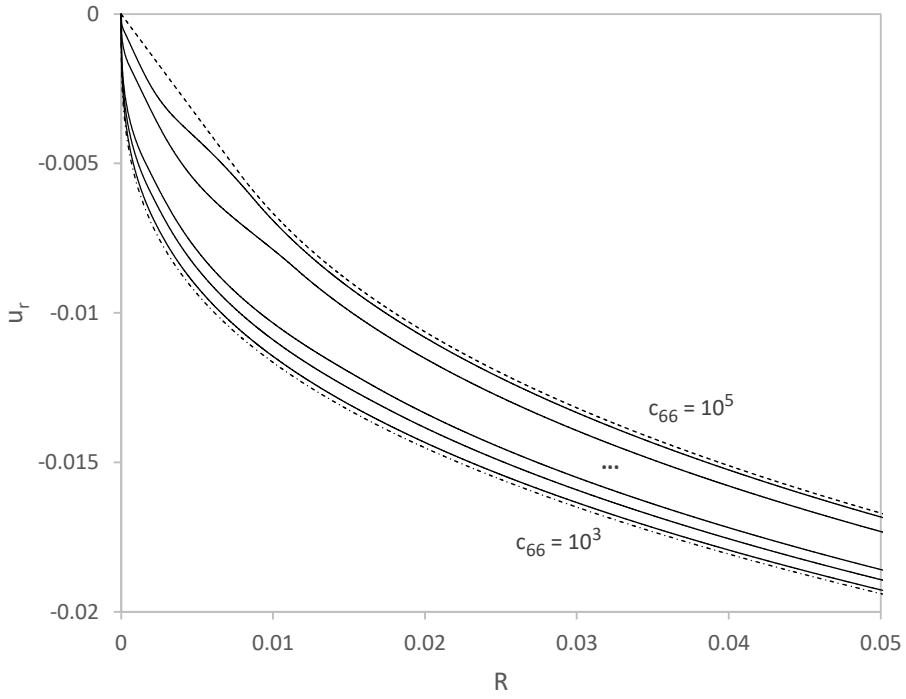

Source: The author.

Figure 27 – Tangential displacement u_θ for the rotationally symmetric solution for increasing values of c_{66} and for $\delta = 10^8$.

(a) Entire interval

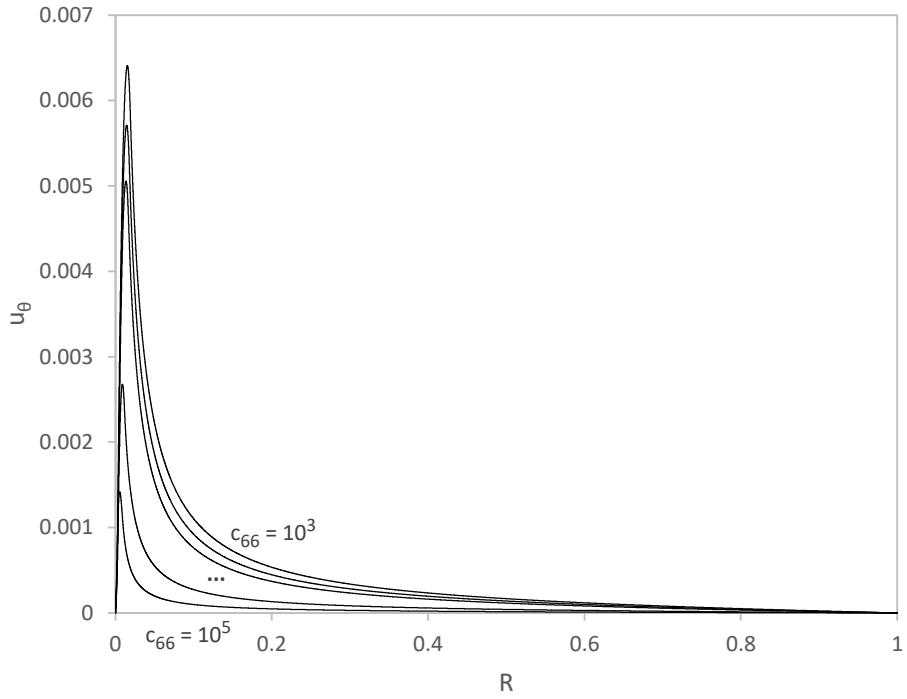

(b) Neighborhood of the origin

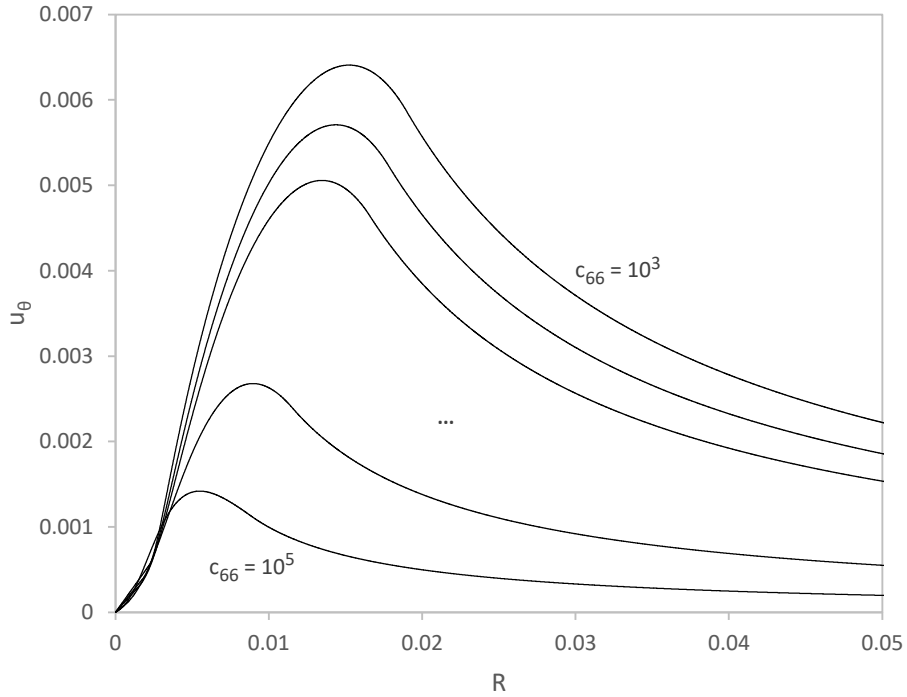

Source: The author.

Figure 28 – Field $r(R) - R$ versus radius R in (a) $(0, 1)$ and (b) $(0, 0.05)$ for ...

——— Rotationally symmetric solution for $c_{66} = 10^3, 5 \times 10^3, 10^4, 5 \times 10^4, 10^5$
------ Radially symmetric solution (5.37)
-·-·- Unconstrained solution (5.28)

(a) Entire interval

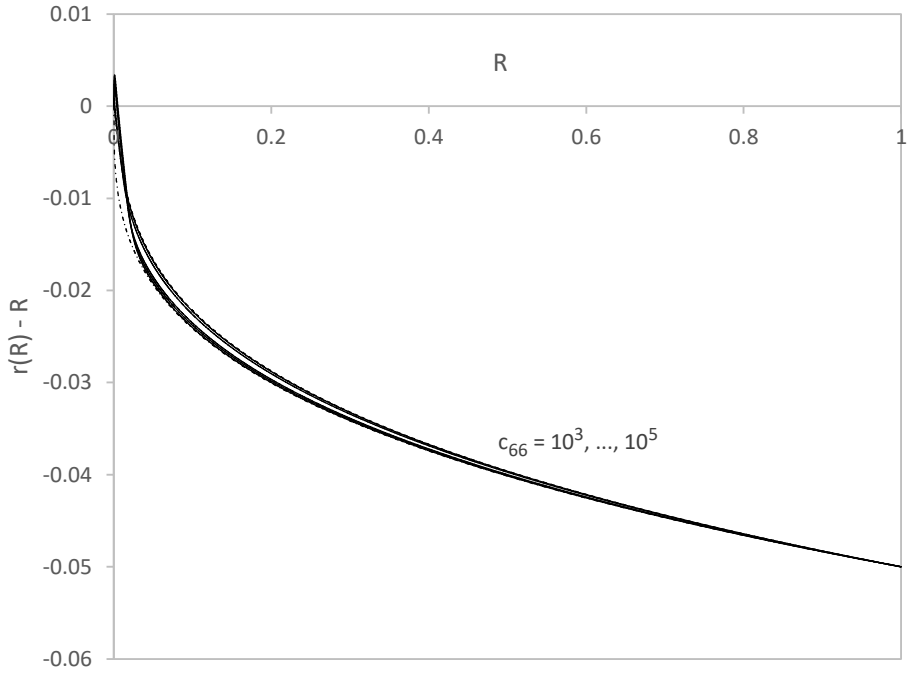

(b) Neighborhood of the origin

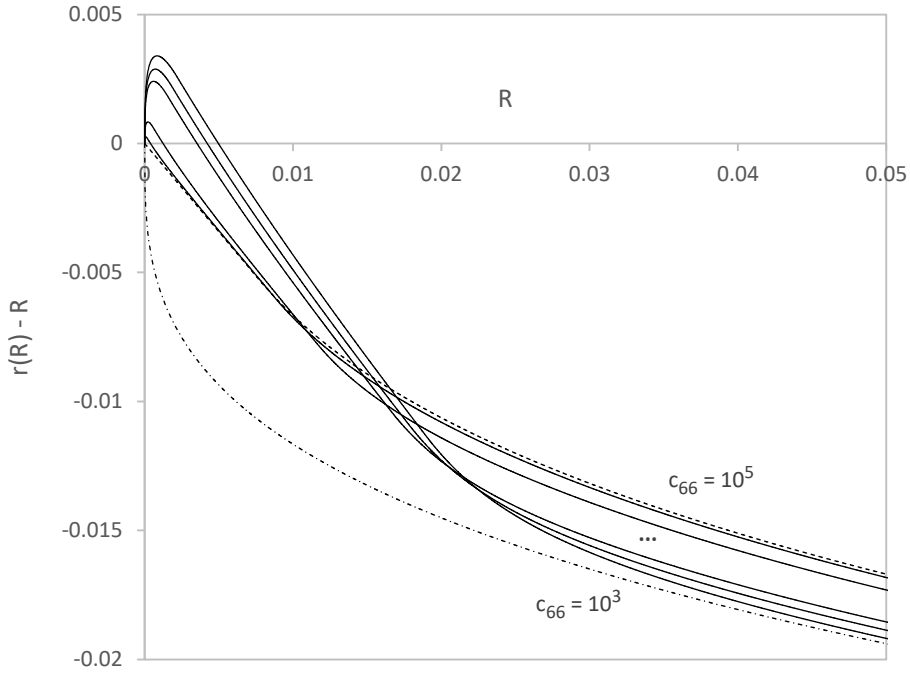

Source: The author.

Figure 29 – Angle of rotation φ obtained from the rotationally symmetric solution for increasing values of c_{66} and for $\delta = 10^8$.

(a) Entire interval

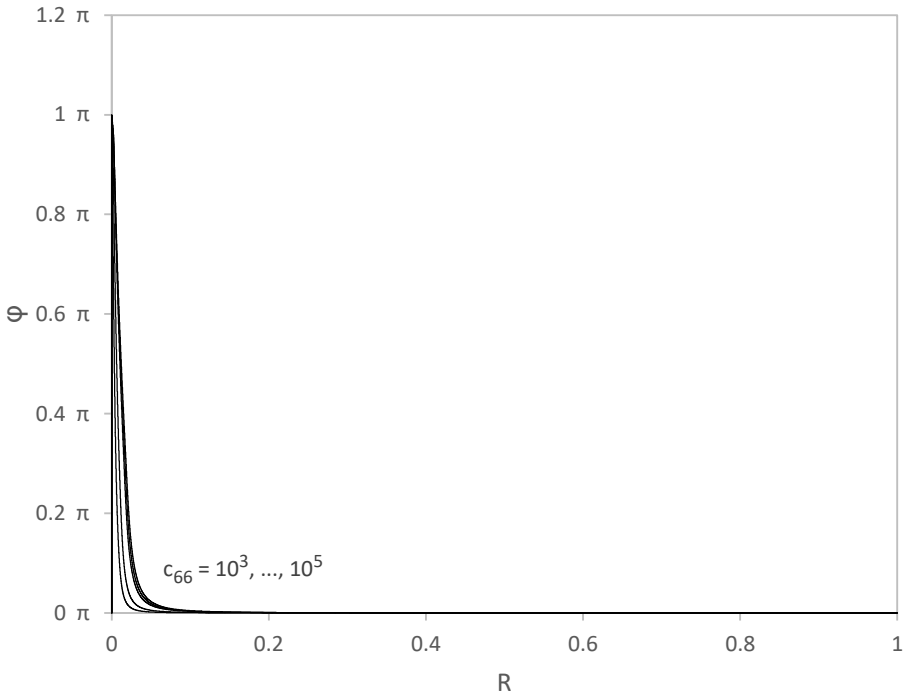

(b) Neighborhood of the origin

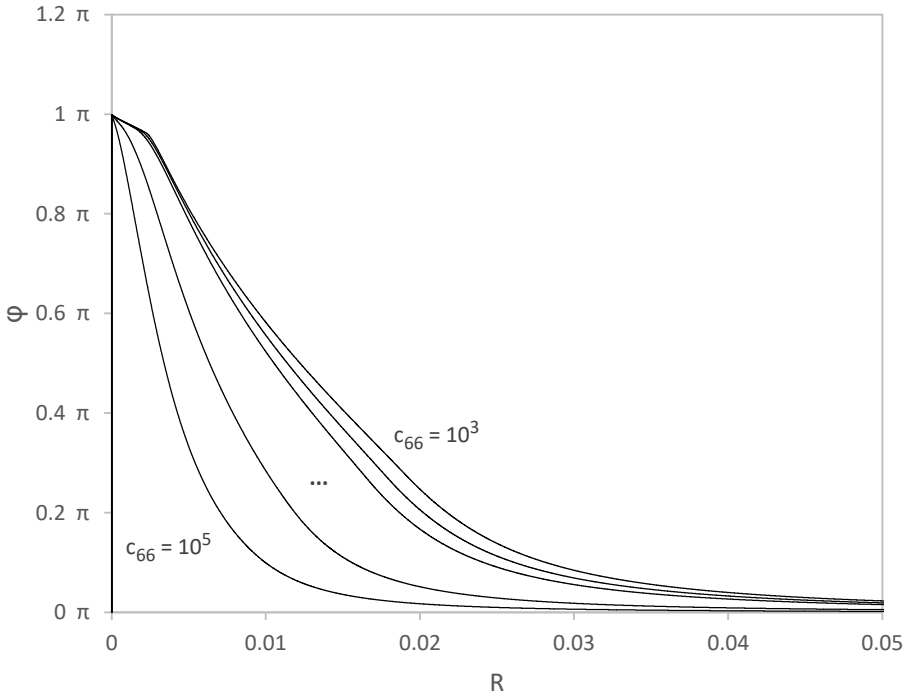

Source: The author.

Figure 30 – Determinant of the deformation gradient J obtained from the rotationally symmetric solution using both increasing values of c_{66} and $\delta = 10^8$ in the interval $(0, 1)$.

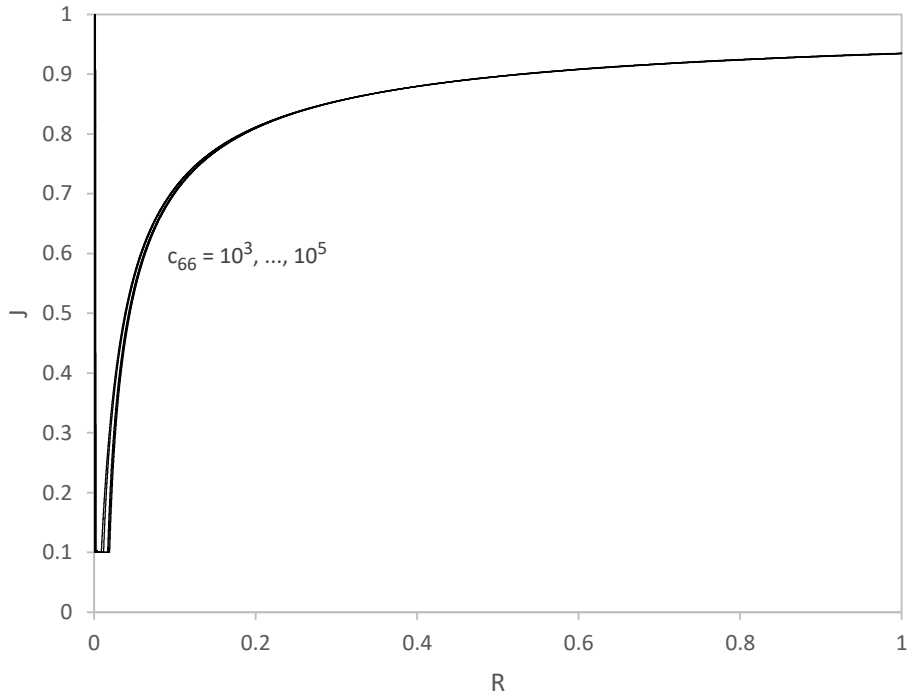

Source: The author.

23, the curves in Figure 30 are similar to the curves shown in Figure 23 and become indistinguishable as we move away from the origin.

To investigate the behavior of J near the center of the disk, we show in Figure 31 a sequence of graphs of J versus $R \in (0, 0.03)$ obtained from numerical solutions using increasing values of c_{66}, shown in Figure 31a-e, and from the radially symmetric solution, shown in Figure 31f. Again, we evaluate J at all the quadrature points and, because of mesh refinement, the oscillatory behavior is not visible at this scale. We see from this figure that, although the active zone, for which $J = \varepsilon$, of the rotationally symmetric solution is an annular region for all the considered values of c_{66}, both its inner and outer radii decrease as c_{66} increases, making the annular region to become the active zone of the radially symmetric solution, which is a central core of the disk. In addition, observe from Figure 31c and Figure 31d that there is a sharp change in values of both the inner and outer radii as c_{66} goes from 10^4 to 5×10^4.

In Table 1 we show values of the total potential energy $\mathcal{E}[\mathbf{u}_h]$, given by (6.11), which were calculated using the numerical solution obtained from the non-uniform mesh with 9600 elements and exact solutions from both the classical linear elasticity theory, given by (5.28), and the constrained theory, given by (5.37). We also include the energy

Figure 31 – Determinant of the deformation gradient J obtained from the rotationally symmetric solution using both increasing values of c_{66} and $\delta = 10^8$ in the interval $(0, 0.03)$.

(a) Rotationally symmetric $c_{66} = 10^3$

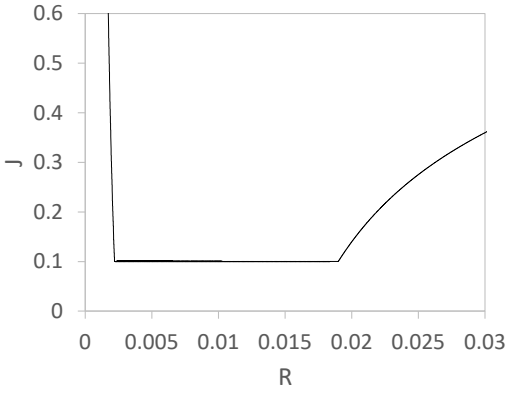

(b) Rotationally symmetric $c_{66} = 5 \times 10^3$

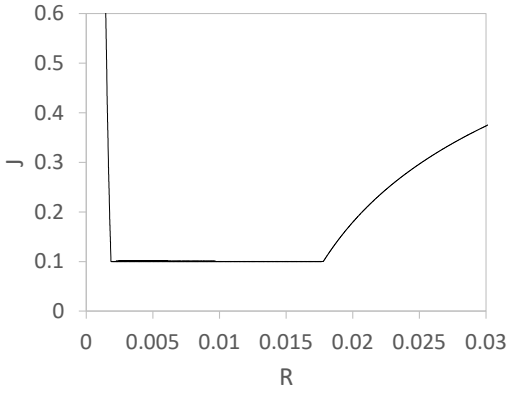

(c) Rotationally symmetric $c_{66} = 10^4$

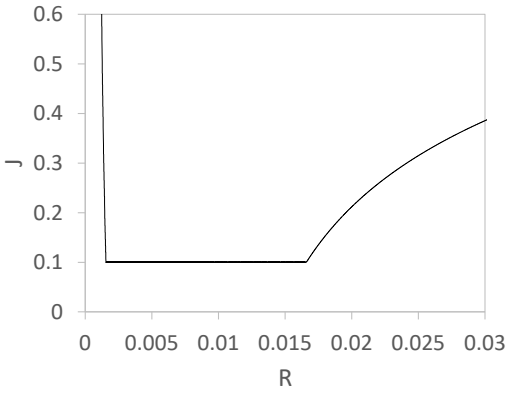

(d) Rotationally symmetric $c_{66} = 5 \times 10^4$

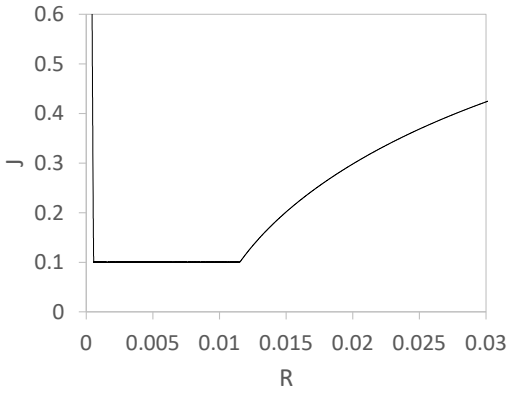

(e) Rotationally symmetric $c_{66} = 10^5$

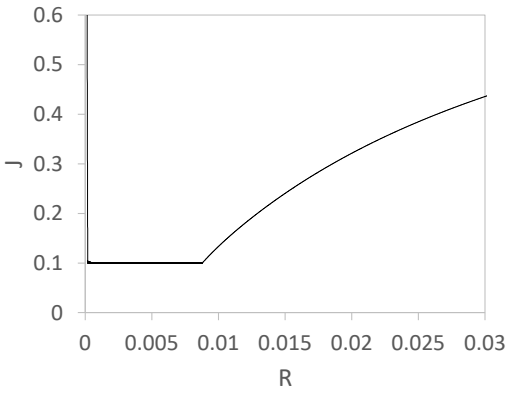

(f) Radially symmetric

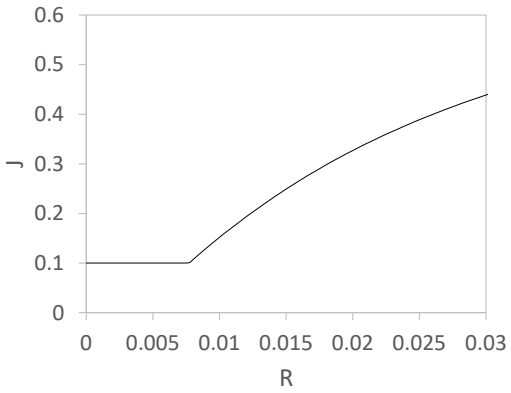

Source: The author.

Table 1 – Total potential energy functional $\mathcal{E}[\mathbf{u}_h]$.

Solutions	$\mathcal{E}[\mathbf{u}_h]$
Unconstrained	256.2187
Rotationally symmetric $c_{66} = 10^3$	256.6323
Rotationally symmetric $c_{66} = 5 \times 10^3$	257.6901
Rotationally symmetric $c_{66} = 10^4$	258.7256
Rotationally symmetric $c_{66} = 5 \times 10^4$	262.6071
Rotationally symmetric $c_{66} = 10^5$	264.0836
Rotationally symmetric $c_{66} = 1.72 \times 10^5$	264.4764
Radially symmetric	264.4763

Source: The author.

calculated from the rotationally symmetric displacement field obtained with shear stiffness $c_{66} = 1.72 \times 10^5$, which was not shown in the previous figures. This value represents the threshold beyond which we could not obtain the rotationally symmetric solution with the non-uniform mesh of 9600 elements, and it was obtained using different values of u_θ^0 and δ. We comment more about these numerical parameters below. We see from Table 1 that the total potential energy of the rotationally symmetric solution increases as c_{66} increases and that this energy is lower than that from the radially symmetric solution for the considered values of c_{66}, except for $c_{66} = 1.72 \times 10^5$. For this value, the total potential energy calculated with the rotationally symmetric solution is slightly greater than its radially symmetric counterpart. However, we have verified that this is due to the level of mesh refinement used. If we further refine the mesh, the energy calculated from the radially symmetric solution becomes the largest.

Defining c_{66}^{max} as the maximum value of the shear modulus from which we obtain only the radially symmetric solution, we say that $c_{66}^{max} = 1.72 \times 10^5$ for the considered mesh of 9600 elements. We also investigate c_{66}^{max} for other meshes. Recall from the beginning of this section that we are using a non-uniform mesh of $600\,q$ elements, where we have used $q = 16$ to obtain the results shown above. In Table 2, we show c_{66}^{max} for meshes parameterized by different values of q, and, in Figure 32, we plot the values of Table 2 in a graph of c_{66}^{max} versus base 10 logarithm of q. Differently from the above results regarding the rotationally symmetric solution for different values of c_{66}, where we used the numerical parameters $\delta \in \{10^{-3}, 10^{-2}, 10^{-1}, ..., 10^8\}$ and $u_\theta^0 = 10^{-5}$; to obtain the values c_{66}^{max} presented in Table 2, we use the sequence $\{10^{-1}, 10^0, 10^1, ..., 10^8\}$ for the penalty parameter δ and the perturbation $u_\theta^0 = 10^{-3}$. Numerical experiments have shown that these numerical parameters yield higher values of c_{66}^{max}. In other words, given a mesh, with these numerical parameters, we have obtained a higher threshold value of c_{66}, from which

Table 2 – Values of c_{66}^{max} for non-uniform meshes with $600\,q$ elements.

q	c_{66}^{max}
1	1.41×10^5
2	1.51×10^5
4	1.60×10^5
8	1.67×10^5
16	1.72×10^5
32	1.76×10^5
64	1.79×10^5
128	1.81×10^5
256	1.83×10^5
512	1.84×10^5
1024	1.85×10^5
2048	1.86×10^5

Source: The author.

we obtain only the radially symmetric solution.

We see from Table 2 and Figure 32 that c_{66}^{max} increases monotonically, but at a lower rate as the mesh is refined. It seems that we would need a extremely refined mesh to obtain the rotationally symmetric solution for c_{66} much greater than 1.86×10^5. It is also not clear if c_{66}^{max} is finite for $q \to \infty$. In fact, we have seen from Figures 26, 27 and 28 that the rotationally symmetric solution approaches the radially symmetric solution as c_{66} increases. This might indicate that the rotationally symmetric solution tends to the radially symmetric one in the limit case $c_{66} \to \infty$, and thus, there would be no threshold value of c_{66} beyond which the rotationally symmetric solution does not exist.

6.2.4 The influence of the loading

In the previous section, we presented the maximum value c_{66}^{max} of shear modulus for which we were able to obtain a rotationally symmetric solution; for larger values, we obtain only the radially symmetric solution. This value was obtained for a given mesh holding all the other parameters fixed, including the displacement $\bar{\mathbf{u}}$ imposed on the contour. We now investigate how a change of $\bar{\mathbf{u}}$ affects the existence of the rotationally symmetric solution.

For that, we use the same mesh described in Section 6.2.3 and the parameters: $\bar{u}_\theta := \bar{\mathbf{u}} \cdot \mathbf{e}_\theta = 0$, $c_{11} = 10^5$, $c_{22} = 10^4$, $c_{12} = 10^3$, $\varepsilon = 0.1$, $R_e = 1$, $\varepsilon_{\mathbf{s}} = \varepsilon_\alpha = 10^{-12}$, $N_\alpha = 50$, $\delta \in \{10^{-1}, 10^0, 10^1, ..., 10^8\}$ and $u_\theta^0 = 10^{-3}$. These parameters were also used in

Figure 32 – Values of c_{66}^{max} versus the base 10 logarithm of q.

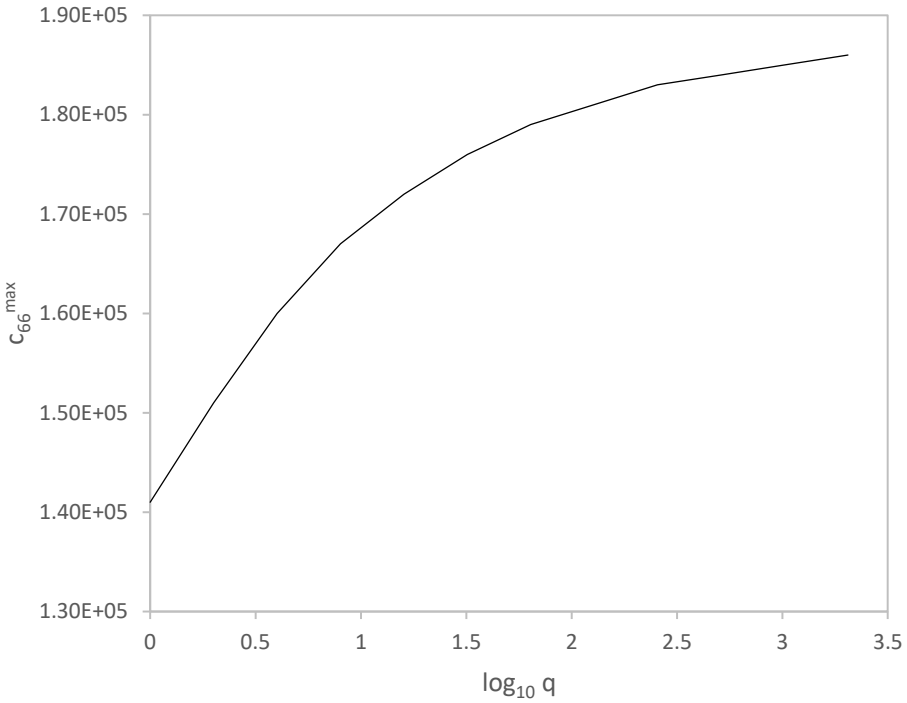

Source: The author.

the search of the values c_{66}^{max} in the previous section. The mesh parameter q, the shear modulus c_{66}, and the imposed radial displacement $\bar{u}_r := \bar{\mathbf{u}} \cdot \mathbf{e}_r < 0$ are specified next for each case studied.

In Figure 33, we hold $c_{66} = 1.72 \times 10^5$ fixed and present the maximum value u_θ^{max}, in modulus, of the tangential displacement for different values of $|\bar{u}_r|$. Recall from Table 2 that this value of c_{66} is c_{66}^{max} for $q = 16$. The results are presented for five different meshes parameterized by $q = 16, 32, 64, 128, 256$. We see from Figure 33 that, for a given q, u_θ^{max} is zero for $|\bar{u}_r|$ in the interval $(0, \bar{u}_r^{min})$, where $\bar{u}_r^{min}$ is the minimum value of $|\bar{u}_r|$ above which u_θ^{max} is not zero. Above $\bar{u}_r^{min}$, the corresponding u_θ^{max} increases monotonically. Thus, the graphs in Figure 33 can be interpreted as equilibrium diagrams, where the $\bar{u}_r^{min}$ represents the critical load below which only the radially symmetric solution given by (5.37) exists. Above this critical load, a secondary solution may also exist, which is given by the rotationally symmetric solution obtained numerically. At the critical load, the two solutions exist and have the same total potential energy $\mathcal{E}[\mathbf{u}_h]$. In this respect, observe from Table 1 that both the rotationally symmetric and the radially symmetric solutions have almost the same value of $\mathcal{E}[\mathbf{u}_h]$ for $q = 16$. Above the critical load, we have verified that the total potential energy of the rotationally symmetric solution is lower than its counterpart of the radially symmetric solution. We also see from Figure 33 that, $\bar{u}_r^{min}$ decreases as the mesh is refined, which seems to indicate that, as $q \to \infty$, its limit value is

Figure 33 – Modulus of the imposed radial displacement $|\bar{u}_r|$ versus the maximum tangential displacement u_θ^{max} for $c_{66} = 1.72 \times 10^5$ and different meshes parameterized by $q = 16, 32, 64, 128, 256$.

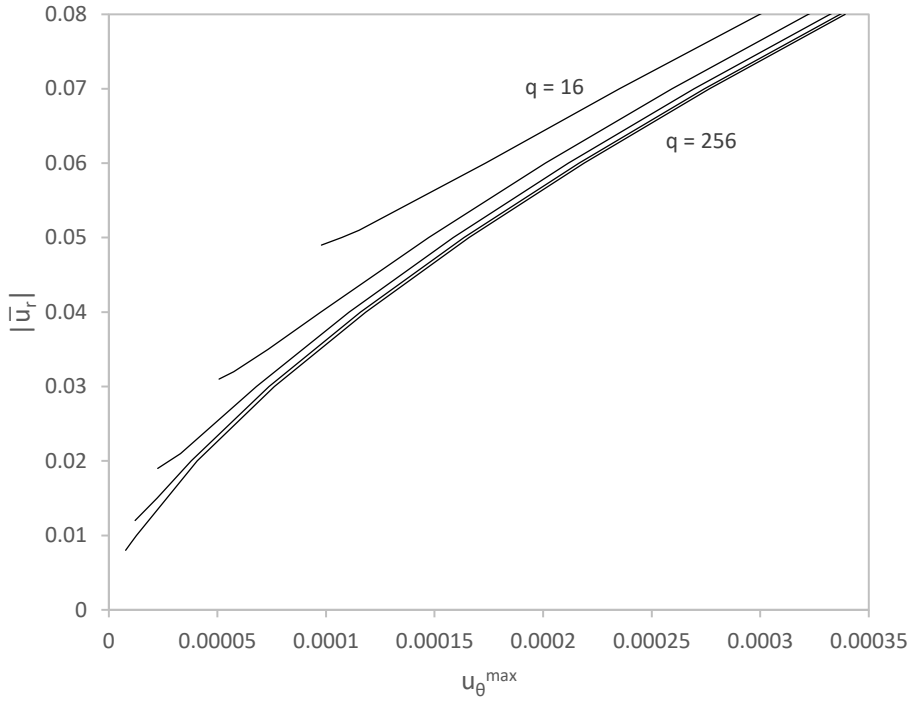

Source: The author.

zero. This being the case, we have that, for $c_{66} = 1.72 \times 10^5$, the rotationally symmetric solution exists for any value of $|\bar{u}_r|$.

Figure 34 is analogous to Figure 33, but for a higher shear modulus $c_{66} = 1.83 \times 10^5$ and $q = 64, 128, 256$. Recall from Table 2 that this value of c_{66} is c_{66}^{max} for $q = 256$. Because of the computational cost required to obtain Figure 34, we have limited ourselves to $q = 64, 128, 256$ and $c_{66} = 1.83 \times 10^5$.

The graphs of Figure 34 display a similar behavior of the graphs in Figure 33, with $\bar{u}_r^{min}$ decreasing with the refinement of the mesh. Again, this behavior suggests that, as $q \to \infty$, $\bar{u}_r^{min} \to 0$ and, therefore, the rotationally symmetric solution might exist for any value of $|\bar{u}_r|$.

Even though the results of Section 6.2.3 were not conclusive about the existence of a limit value for c_{66}^{max} above which no rotationally symmetric solution exists, it is physically plausible to assume that this solution does not exist for $c_{66} \gg c_{66}^{max}$. This being the case, a limit value for c_{66}^{max} should exist based on this physical argument. We call this value c_{66}^{phys}.

On the other hand, the results of Section 6.2.4 indicate the possibility of $\bar{u}_r^{min}$ tending to zero as $q \to \infty$ for a given c_{66}. In view of the previous paragraph, it is not clear

Figure 34 – Modulus of the imposed radial displacement $|\bar{u}_r|$ versus the maximum tangential displacement u_θ^{max} for $c_{66} = 1.83 \times 10^5$ and different meshes parameterized by $q = 64, 128, 256$.

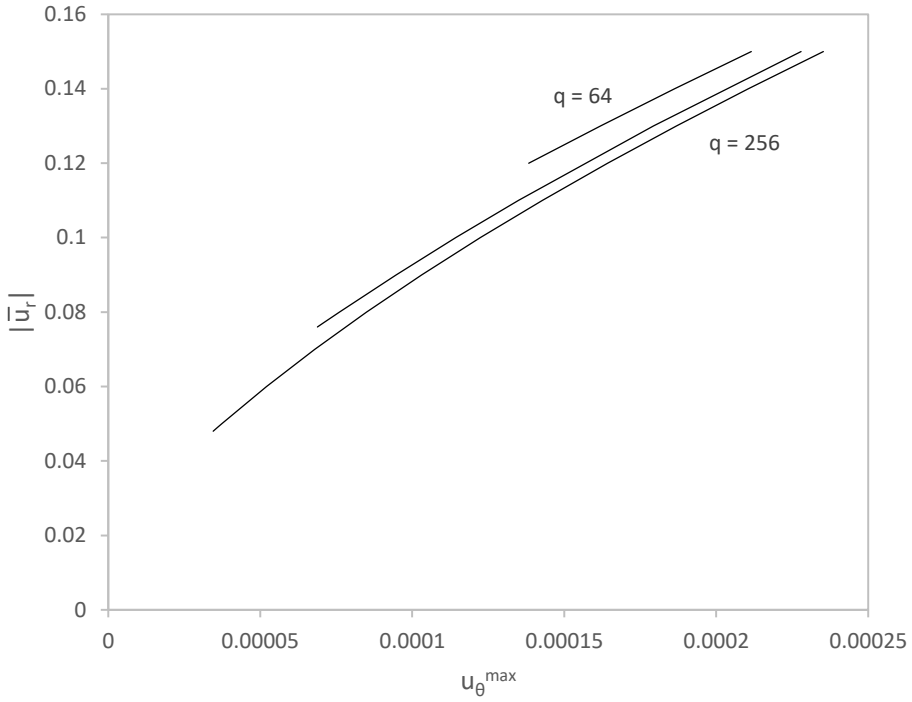

Source: The author.

whether the limit value of $\bar{u}_r^{min}$ would be zero for $c_{66} = c_{66}^{phys}$. These aspects of the research remain open.

6.2.5 Asymmetric displacement field

The results presented above were obtained by assuming that the displacement field is rotationally symmetric. Here, to validate these results, we consider the more general case of an asymmetric displacement field, in which we determine radial and tangential displacements in a two-dimensional domain. For that, we consider two different formulations, which will be explained next. Both formulations confirmed the rotationally symmetric solution presented previously.

Recall from Section 4.1 that we solve a sequence of minimization problems of the form (4.2), where $\mathcal{E}_\delta$ is given by (4.1). Observe from (4.1) that $\mathcal{E}$, given by (3.61), and $\mathcal{P}$, given by (4.3), are integrals evaluated over the domain $\mathcal{B} \in \mathbb{R}^2$, which was introduced in Section 6.1 as the region occupied by the disk in the reference configuration. Until now, our assumption of the radial or rotational symmetry of the displacement field allowed us to integrate not on $\mathcal{B}$, but on the interval $(0, R_e)$. By considering an asymmetric displacement field, we perform integrations on $\mathcal{B}$ using either polar or Cartesian coordinates, as explained

below.

First, we write the integrals that appear in both (3.61) and (4.3) in terms of polar coordinates (R, Θ) defined in the domain $(0, R_e) \times (0, 2\pi)$. This is the same approach used in Section 6.1 to obtain the integrals in both (6.9) and (6.10). There, however, the assumption of rotationally symmetric displacement field introduced through (6.1) lead to the integrals in both (6.11) and (6.12), which are defined in $(0, R_e)$ only.

Here, we make no assumptions on the plane displacement field, which means that it is asymmetric and given by

$$\mathbf{u}(R, \Theta) = u_r(R, \Theta)\, \mathbf{e}_r + u_\theta(R, \Theta)\, \mathbf{e}_\theta. \tag{6.15}$$

We then have that the strain components in (6.2) are given by

$$\epsilon_{rr} = u_{r,R}, \qquad \epsilon_{\theta\theta} = \frac{u_r}{R} + \frac{u_{\theta,\Theta}}{R}, \qquad \epsilon_{r\theta} = \frac{1}{2}\left(\frac{u_{r,\Theta}}{R} + u_{\theta,R} - \frac{u_\theta}{R}\right), \tag{6.16}$$

where $(\cdot)_{,A} \coloneqq \partial(\cdot)/\partial A$. It follows from the generalized Hooke's Law (3.60a) that the stress components are related to the strain components by

$$\begin{aligned} \sigma_{rr} &= c_{11}\epsilon_{rr} + c_{12}\epsilon_{\theta\theta}, \\ \sigma_{\theta\theta} &= c_{12}\epsilon_{rr} + c_{22}\epsilon_{\theta\theta}, \\ \sigma_{r\theta} &= 2c_{66}\epsilon_{r\theta}. \end{aligned} \tag{6.17}$$

Using (6.7), (6.16), (6.17), and $dV = R\, dR\, d\Theta$, we obtain from (3.61) that the total potential energy functional $\mathcal{E}$ can be written as

$$\begin{aligned} \mathcal{E}[\mathbf{u}] = \int_0^{2\pi} \int_0^{R_e} \Bigg[& \frac{c_{11}\, R\, u_{r,R}^2}{2} + c_{12}\, u_r\, u_{r,R} + c_{12}\, u_{r,R}\, u_{\theta,\Theta} + \frac{c_{22}\, u_r^2}{2R} \\ & + \frac{c_{22}\, u_r\, u_{\theta,\Theta}}{R} + \frac{c_{22}\, u_{\theta,\Theta}^2}{2R} + \frac{c_{66}\, R\, u_{\theta,R}^2}{2} - c_{66}\, u_\theta\, u_{\theta,R} \\ & + c_{66}\, u_{r,\Theta}\, u_{\theta,R} + \frac{c_{66}\, u_\theta^2}{2R} - \frac{c_{66}\, u_\theta\, u_{r,\Theta}}{R} + \frac{c_{66}\, u_{r,\Theta}^2}{2R} \Bigg] dR\, d\Theta, \end{aligned} \tag{6.18}$$

where we recall from Section 6.1 that $\mathbf{b}_0 = \bar{\mathbf{t}} = \mathbf{0}$.

The determinant of the deformation gradient for the case of an asymmetric displacement field is given by

$$\det(\mathbf{1} + \nabla\mathbf{u}) = (1 + u_{r,R})\left(1 + \frac{u_r}{R} + \frac{u_{\theta,\Theta}}{R}\right) - u_{\theta,R}\left(\frac{u_{r,\Theta}}{R} - \frac{u_\theta}{R}\right). \tag{6.19}$$

Using (6.19), we obtain from (4.3) that the barrier functional $\mathcal{P}$ can be written as

$$\mathcal{P}[\mathbf{u}] = \int_0^{2\pi} \int_0^{R_e} \frac{1}{(1 + u_{r,R})\,(1 + u_r/R + u_{\theta,\Theta}/R) - u_{\theta,R}\,(u_{r,\Theta}/R - u_\theta/R) - \varepsilon}\, R\, dR\, d\Theta. \tag{6.20}$$

Next, we discretize the region $(0, R_e) \times (0, 2\pi)$ with a sequence of meshes composed of bilinear finite elements. To reduce the computational costs, we do not employ uniform meshes, but three meshes parameterized by $q \in \{1, 4, 16\}$, where the interval $(0, R_e)$ is discretized by $600\,q$ elements as following: $375\,q$ elements in $0 < R < 0.07\,R_e$, $125\,q$ elements in $0.07\,R_e < R < 0.46\,R_e$ and $100\,q$ elements in $0.46\,R_e < R < R_e$. The interval $(0, 2\pi)$ is discretized uniformly by 64 elements for all values of q. Thus, the discretized domains are rectangles with dimensions R_e by 2π and are the union of $64 \times 600\,q$ rectangular elements.

Substituting the finite element approximation (4.6) into both (6.18) and (6.20) and recalling from Section 4.2 that $\mathcal{E}_h(\mathbf{s}) := \mathcal{E}[\mathbf{u}_h]$ and $\mathcal{P}_h(\mathbf{s}) := \mathcal{P}[\mathbf{u}_h]$, where $\mathbf{s}$ is the vector of degrees of freedom given by $\mathbf{s} \coloneqq (s^1, s^2, ..., s^m)$, we obtain the associated discrete minimization problem given by (4.8), where $\mathcal{F}_\delta$ is given by (4.7). In view of the expressions (6.18) and (6.20), we call this formulation the polar formulation.

In this formulation, which is analogous to the rotationally symmetric case, the degrees of freedom s^{2i-1} and s^{2i} from (4.6), where $i = 1, 2, 3, ..., M$ and M is the number of mesh nodes, represent the radial and tangential displacements of the i-th node, respectively. Thus, $s^{2i-1} = \mathbf{u}_h(R_i, \Theta_i) \cdot \mathbf{e}_r$ and $s^{2i} = \mathbf{u}_h(R_i, \Theta_i) \cdot \mathbf{e}_\theta$, where (R_i, Θ_i) are the polar coordinates of the i-th node.

Similar to Section 6.2.2, we consider that the initial guess $\mathbf{s}_0$ is based on both the solution of the disk problem for an isotropic material and a small perturbation u_θ^0, which, in this section, is given by $u_\theta^0 = 10^{-2}$. From our experience gained in the rotationally symmetric case, the use of large values of u_θ^0, such as $u_\theta^0 = 10^{-2}$, reduces the total number of iterations of the numerical procedure, which reduces the computational cost. Except when specified otherwise, all the material, geometric, and numerical parameters are the same parameters used in Section 6.2.2.

In Figure 35, the solid lines represent the tangential displacement u_θ obtained from the three meshes discussed above and a fixed large penalty parameter $\delta = 10^8$. The dashed line represents u_θ of the rotationally symmetric solution obtained with the mesh composed of 65534 elements of Section 6.2.2. The results are presented for the interval $(0, 0.05)$. We see from this figure that approximations of u_θ from the asymmetric solution converge to u_θ from the rotationally symmetric solution as the mesh is refined. In particular, the dashed line is very close to the solid line corresponding to $q = 16$.

In Figure 36, we plot $r(R) - R$, defined by (6.13), versus R in the interval $(0, 0.05)$, where the solid lines represent u_r obtained numerically using the three meshes parameterized by $q = 1, 4, 16$ for a fixed large penalty parameter $\delta = 10^8$. We also show the radially symmetric solution, given by (5.37) and represented by the dashed line, and the unconstrained solution, given by (5.28) and represented by the dash-dotted line. We see from this figure that, as the mesh is refined, the numerical asymmetric solutions converge to a limit function that is very close to the unconstrained solution, instead of the radially

Figure 35 – Tangential displacement u_θ of the asymmetric solution obtained using the polar formulation and of the rotationally symmetric solution.

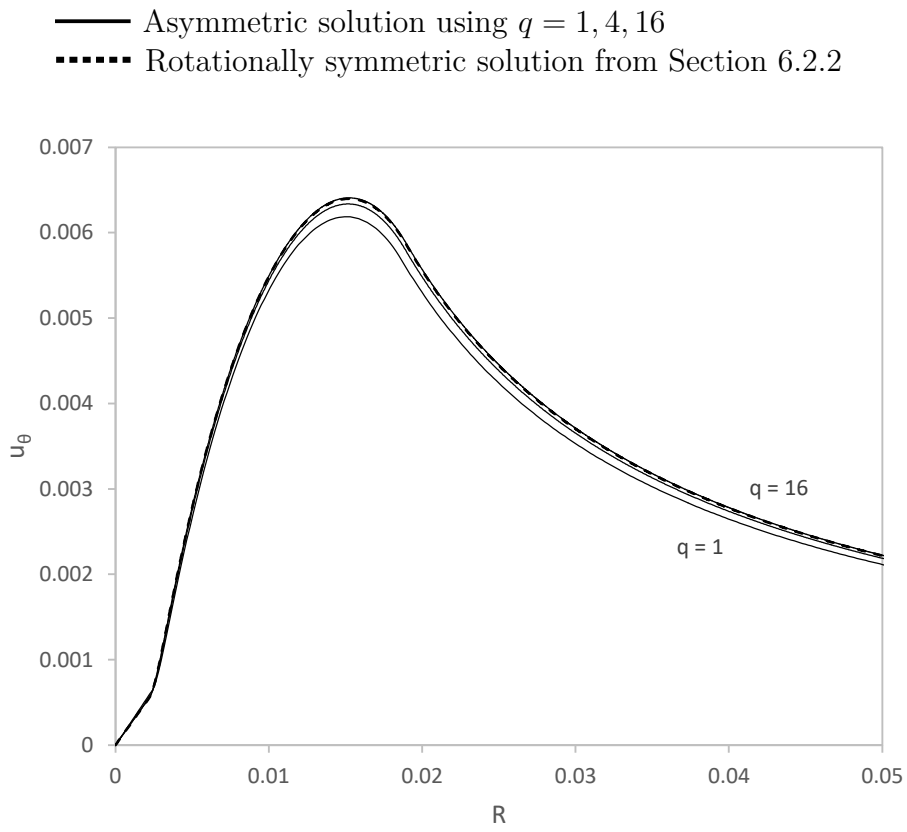

Source: The author.

symmetric solution of the constrained theory. The results presented in Figures 35 and 36 are in very good agreement with the results presented in Section 6.2.2. In particular, observe the strong similarity between the graphs in Figure 19b and Figure 36.

The polar formulation used above takes advantage of the geometry of the disk, which is circular, the uniform radial distribution of the load on the boundary, and the material symmetry of the solid, which is cylindrically anisotropic. Since one objective of this work is to compare our results with results obtained by Fosdick, Freddi and Royer-Carfagni (2008), who have discretized the circular disk, we introduce below a Cartesian formulation, which uses Cartesian, rather than polar, coordinates to represent all the variables. As a consequence, our domain of discretization is an approximation of the circular disk, rather than the rectangular domain $(0, R_e) \times (0, 2\,\pi)$ used previously in the polar formulation.

In a Cartesian coordinate system, the displacement field at a material point $\mathbf{X} = X_1\,\mathbf{e}_1 + X_2\,\mathbf{e}_2$ can be written as

$$\mathbf{u}(\mathbf{X}) = u_1(X_1, X_2)\,\mathbf{e}_1 + u_2(X_1, X_2)\,\mathbf{e}_2, \tag{6.21}$$

where $(\mathbf{e}_1, \mathbf{e}_2)$ is the associated orthonormal basis. Recall from Section 6.1 that, there is

Figure 36 – Field $r(R)-R$ for the asymmetric solution obtained using the polar formulation, the radially symmetric solution and the unconstrained solution.

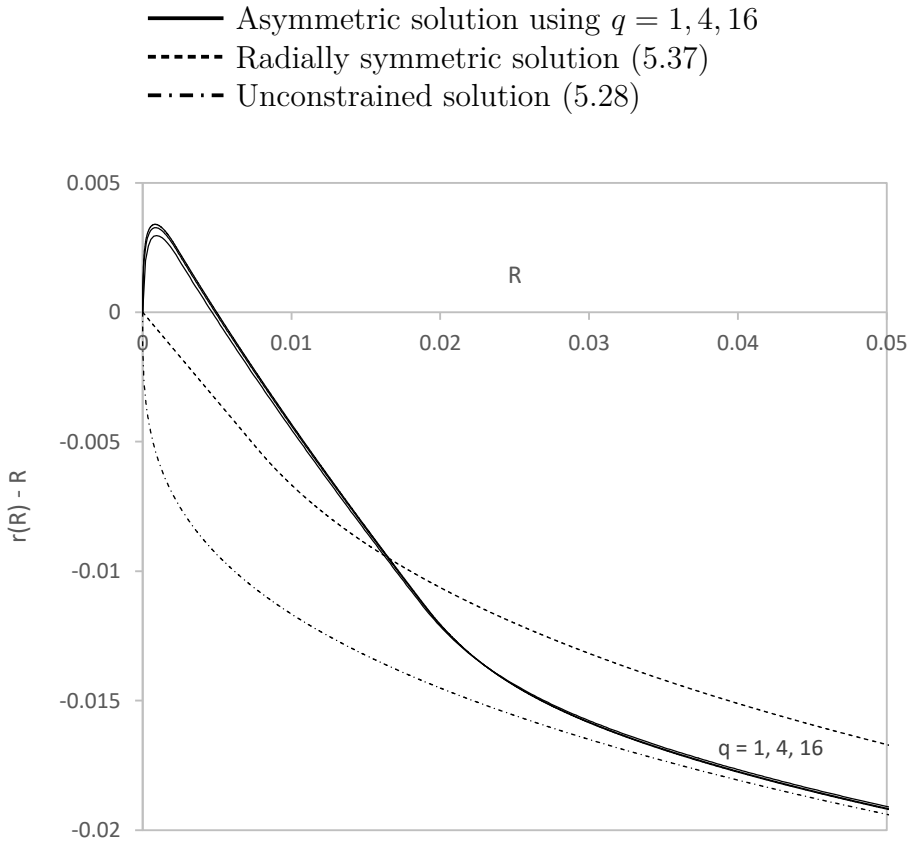

Source: The author.

neither body force nor prescribed traction on the boundary of disk. We then rewrite (3.61) as

$$\mathcal{E}[\mathbf{u}] = \frac{1}{2}\int_{\mathcal{B}} \mathbb{C}[\mathbf{E}] \cdot \mathbf{E}\, dV. \tag{6.22}$$

The polar formulation previously discussed represents the tensors $\mathbb{C} = c_{ijkl}\, \mathbf{e}_i \otimes \mathbf{e}_j \otimes \mathbf{e}_k \otimes \mathbf{e}_l$ and $\mathbf{E} = \epsilon_{ij}\, \mathbf{e}_i \otimes \mathbf{e}_j$ in (6.22) in terms of the polar orthonormal basis $(\mathbf{e}_r, \mathbf{e}_\theta)$. Here, we introduce the Cartesian formulation, which represents these tensors in terms of the Cartesian orthonormal basis $(\mathbf{e}_1, \mathbf{e}_2)$.

Before we express the relation between the components of $\mathbb{C}$ represented in either the polar or the Cartesian basis, we clarify on the notation used for the components of a fourth-order tensor. Because of the minor symmetry of the elasticity tensor $\mathbb{C}$, the four indices of its components c_{ijkl}, $i, j, k, l = 1, 2$, are usually abbreviated to two indices $a, b = 1, 2, 6$ using the rule

$$11 \to 1 \qquad 22 \to 2 \qquad 12 \to 6. \tag{6.23}$$

So that expression (5.1), for the matrix representation of $\mathbb{C}$ in polar coordinates and Voigt

notation, is equivalent to

$$\mathbf{C} = \begin{bmatrix} c_{1111} & c_{1122} & 0 \\ c_{1122} & c_{2222} & 0 \\ 0 & 0 & c_{1212} \end{bmatrix}. \tag{6.24}$$

Similarly, the matrix representation of $\mathbb{C}$ in Cartesian coordinates and Voigt notation is given by

$$\mathbf{C}^c = \begin{bmatrix} c^c_{1111}(\mathbf{X}) & c^c_{1122}(\mathbf{X}) & c^c_{1112}(\mathbf{X}) \\ c^c_{1122}(\mathbf{X}) & c^c_{2222}(\mathbf{X}) & c^c_{2212}(\mathbf{X}) \\ c^c_{1112}(\mathbf{X}) & c^c_{2212}(\mathbf{X}) & c^c_{1212}(\mathbf{X}) \end{bmatrix}. \tag{6.25}$$

The components c^c_{ijkl} in (6.25) depends on the material point $\mathbf{X}$ because c_{ijkl} and c^c_{ijkl} are related to each other by a change of basis using the transformation matrix $\mathbf{Q}$, given by

$$\mathbf{Q} = [Q_{ij}] = \begin{bmatrix} \cos\Theta & \sin\Theta \\ -\sin\Theta & \cos\Theta \end{bmatrix}, \tag{6.26}$$

where Θ is the polar angle of the material point $\mathbf{X}$. This change of basis correspond to the following relation between c_{ijkl} and c^c_{ijkl}

$$c^c_{ijkl}(\mathbf{X}) = Q_{mi}\, Q_{nj}\, Q_{ok}\, Q_{pl}\, c_{mnop}, \tag{6.27}$$

where $i, j, k, l, m, n, o, p = 1, 2$.

In terms of the Cartesian orthonormal basis $(\mathbf{e}_1, \mathbf{e}_2)$, the strain tensor

$$\mathbf{E} = \epsilon_{11}\, \mathbf{e}_1 \otimes \mathbf{e}_1 + \epsilon_{22}\, \mathbf{e}_2 \otimes \mathbf{e}_2 + \epsilon_{12}\, (\mathbf{e}_1 \otimes \mathbf{e}_2 + \mathbf{e}_2 \otimes \mathbf{e}_1), \tag{6.28}$$

with components given by

$$\epsilon_{11} = u_{1,1} \qquad \epsilon_{22} = u_{2,2} \qquad \epsilon_{12} = \frac{1}{2}(u_{1,2} + u_{2,1}), \tag{6.29}$$

is related to the stress tensor

$$\mathbf{T} = \sigma_{11}\, \mathbf{e}_1 \otimes \mathbf{e}_1 + \sigma_{22}\, \mathbf{e}_2 \otimes \mathbf{e}_2 + \sigma_{12}\, (\mathbf{e}_1 \otimes \mathbf{e}_2 + \mathbf{e}_2 \otimes \mathbf{e}_1), \tag{6.30}$$

by the Generalized Hooke's law in (3.60a).

The stress-strain law (3.60a) can be written in the alternative form

$$\mathbf{t}^c = \mathbf{C}^c\, \mathbf{e}^c \tag{6.31}$$

where the vectors $\mathbf{t}^c$ and $\mathbf{e}^c$ are defined by

$$\mathbf{t}^c := \begin{Bmatrix} \sigma_{11} \\ \sigma_{22} \\ \sigma_{12} \end{Bmatrix} \qquad \mathbf{e}^c := \begin{Bmatrix} \epsilon_{11} \\ \epsilon_{22} \\ 2\,\epsilon_{12} \end{Bmatrix}. \tag{6.32}$$

It follows from (6.31), (6.32) and (6.25) that

$$\begin{aligned}
\sigma_{11} &= c^c_{1111}(\mathbf{X})\,\epsilon_{11} + c^c_{1122}(\mathbf{X})\,\epsilon_{22} + 2c^c_{1112}(\mathbf{X})\,\epsilon_{12},\\
\sigma_{22} &= c^c_{1122}(\mathbf{X})\,\epsilon_{11} + c^c_{2222}(\mathbf{X})\,\epsilon_{22} + 2c^c_{2212}(\mathbf{X})\,\epsilon_{12},\\
\sigma_{12} &= c^c_{1112}(\mathbf{X})\,\epsilon_{11} + c^c_{2212}(\mathbf{X})\,\epsilon_{22} + 2c^c_{1212}(\mathbf{X})\,\epsilon_{12},
\end{aligned} \tag{6.33}$$

or, by using the abbreviation of indexes from (6.23), that

$$\begin{aligned}
\sigma_{11} &= c^c_{11}(\mathbf{X})\,\epsilon_{11} + c^c_{12}(\mathbf{X})\,\epsilon_{22} + 2c^c_{16}(\mathbf{X})\,\epsilon_{12},\\
\sigma_{22} &= c^c_{12}(\mathbf{X})\,\epsilon_{11} + c^c_{22}(\mathbf{X})\,\epsilon_{22} + 2c^c_{26}(\mathbf{X})\,\epsilon_{12},\\
\sigma_{12} &= c^c_{16}(\mathbf{X})\,\epsilon_{11} + c^c_{26}(\mathbf{X})\,\epsilon_{22} + 2c^c_{66}(\mathbf{X})\,\epsilon_{12}.
\end{aligned} \tag{6.34}$$

Similarly to Section 6.1, it follows from (6.22) and (3.60a) together with (6.28) and (6.30) that

$$\mathcal{E}[\mathbf{u}] = \frac{1}{2}\int_{\mathcal{B}} (\sigma_{11}\,\epsilon_{11} + \sigma_{22}\,\epsilon_{22} + 2\,\sigma_{12}\,\epsilon_{12})\,dV. \tag{6.35}$$

Then, from (6.35), (6.29) and (6.34), we have that the total potential energy functional $\mathcal{E}$ can be written as

$$\begin{aligned}
\mathcal{E}[\mathbf{u}] = \int_{\mathcal{B}} \Bigg(&\frac{c^c_{11}\,u^2_{1,1}}{2} + c^c_{12}\,u_{1,1}\,u_{2,2} + c^c_{16}\,u_{1,1}\,u_{1,2} + c^c_{16}\,u_{1,1}\,u_{2,1} + \frac{c^c_{22}\,u^2_{2,2}}{2}\\
&+ c^c_{26}\,u_{1,2}\,u_{2,2} + c^c_{26}\,u_{2,1}\,u_{2,2} + c^c_{66}\frac{u^2_{1,2}}{2} + c^c_{66}\,u_{1,2}\,u_{2,1} + \frac{c^c_{66}\,u^2_{2,1}}{2}\Bigg) dV.
\end{aligned} \tag{6.36}$$

where the dependence of c^c_{ij}, $i,j = 1,2,6$, on $\mathbf{X}$ has been dropped.

Relative to the Cartesian orthonormal basis, the determinant of the deformation gradient is given by

$$\det(\mathbf{1} + \nabla\mathbf{u}) = (1 + u_{1,1})(1 + u_{2,2}) - u_{1,2}\,u_{2,1}. \tag{6.37}$$

It then follows from (4.3) that

$$\mathcal{P}[\mathbf{u}] = \int_{\mathcal{B}} \frac{1}{(1 + u_{1,1})(1 + u_{2,2}) - u_{1,2}\,u_{2,1} - \varepsilon}\,dV. \tag{6.38}$$

Similarly to the polar formulation, by substituting the finite element approximation (4.6) into both (6.36) and (6.38), and recalling from Section 4.2 that $\mathcal{E}_h(\mathbf{s}) := \mathcal{E}[\mathbf{u}_h]$ and $\mathcal{P}_h(\mathbf{s}) := \mathcal{P}[\mathbf{u}_h]$, where $\mathbf{s}$ is the vector of degrees of freedom given by $\mathbf{s} := (s^1, s^2, ..., s^m)$, we obtain the associated discrete minimization problem given by (4.8), where $\mathcal{F}_\delta$ is given by (4.7). In view of the expressions (6.36) and (6.38), we call this formulation the Cartesian formulation.

The integrals in (6.36) and (6.38) are evaluated over the original domain $\mathcal{B}$ of the problem, which is a disk of radius R_e. We discretize $\mathcal{B}$ with a sequence of three meshes

shown in Figure 37. On the left-hand side of this figure, we see discretizations of the whole domain and, on the right-hand side, we see discretizations of a neighborhood of the center of the disk. Each mesh has N isoparametric and bilinear finite elements, where $N = 22448, 31288, 39574$, and the characteristic size of the element in the center of the disk is 10^{-4}, 10^{-5}, 10^{-6}, respectively. In all the meshes, the contour of the disk is approximated by 256 segments of straight lines.

To obtain a numerical approximation of the asymmetric solution, Fosdick, Freddi and Royer-Carfagni (2008) used a mesh of 54912 isoparametric and biquadratic finite elements. Therefore, their discretization yields a better approximation than ours in the sense of:

- It yields a better p-approximation of the solution, where p is the degree of the basis functions of the finite element method; since they used biquadratic finite elements, instead of the bilinear finite elements used in our work.

- It better approximates the contour of the disk; since they used 256 segments generated by quadratic functions, instead of the linear functions used in our work.

- It uses finite elements with a smaller characteristic length near the origin. Even though this value is not informed, the authors indicate that it is smaller than 10^{-7}. Our most refined mesh uses finite elements with a characteristic length equals to 10^{-6} next to the origin.

In this work, we have limited ourselves to a mesh composed of 39574 isoparametric and bilinear finite elements because of the computational costs required to run the mesh of Fosdick, Freddi and Royer-Carfagni (2008).

In Cartesian formulation, the degrees of freedom s^{2i-1} and s^{2i} from (4.6), where $i = 1, 2, 3, ..., M$, with M being the number of mesh nodes, represent the horizontal and vertical displacements of the i-th node, respectively. Thus, $s^{2i-1} = \mathbf{u}_h(X_1^i, X_2^i) \cdot \mathbf{e}_1$ and $s^{2i} = \mathbf{u}_h(X_1^i, X_2^i) \cdot \mathbf{e}_2$ where (X_1^i, X_2^i) are the Cartesian coordinates of the i-th node.

Next, we show convergent results that confirm the rotationally symmetric displacement field of Section 6.2.2, even though we do not perturb the tangential displacement of the initial guess. We believe that this is due to the approximation of the contour by 256 segments. Since these segments do not form a perfect circle, they introduce a tangential displacement that is large enough to act as the perturbation u_θ^0 used in Section 6.2.2. Except when specified otherwise, all the material, geometric, and numerical parameters are the same parameters used in Section 6.2.2. Below we consider $X_2 = 0$, which corresponds to $\Theta = 0$, and plot graphs of $u_\theta(R)$ and $r(R) - R$ versus R, where, here, $R = X_1 \in (0, R_e)$, $u_\theta(R) = u_2(X_1, 0)$, $r(R) = \sqrt{(R + u_1(R, 0))^2 + u_2(R, 0)^2}$. These graphs are shown in Fig-

Figure 37 – Meshes composed of $N \in \{22448, 31288, 39574\}$ elements.

(a) $N = 22448$

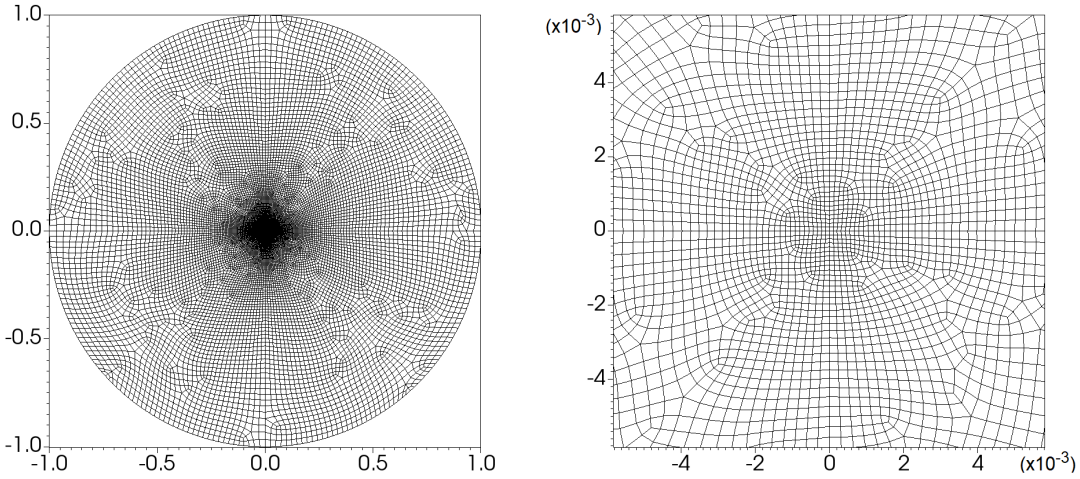

(b) $N = 31288$

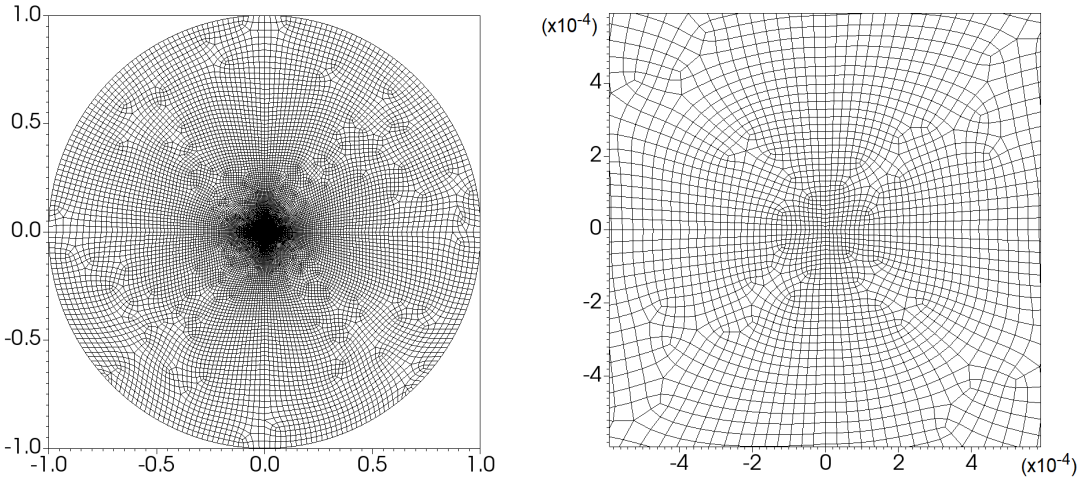

(c) $N = 39574$

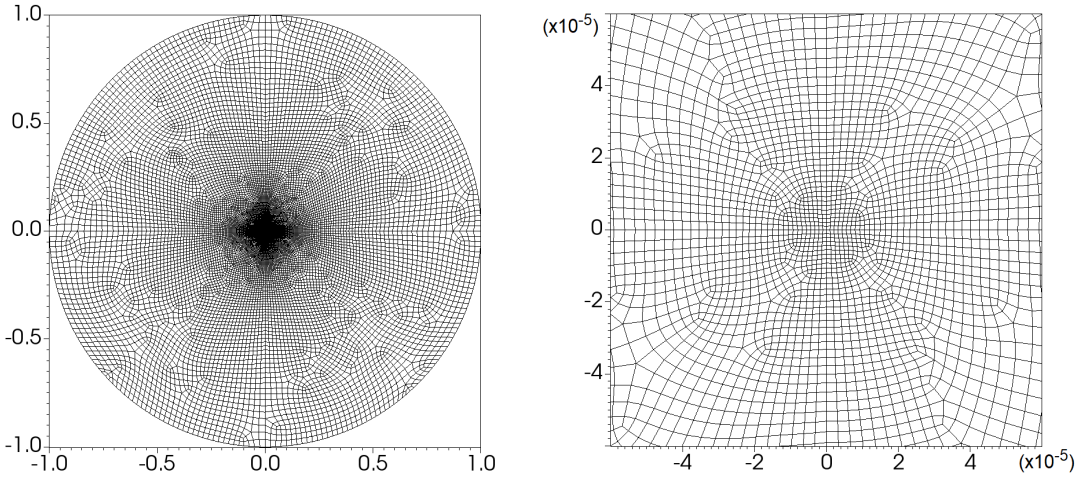

Source: The author.

Figure 38 – Tangential displacement u_θ of the asymmetric solution obtained using the Cartesian formulation and of the rotationally symmetric solution obtained with 65536 elements.

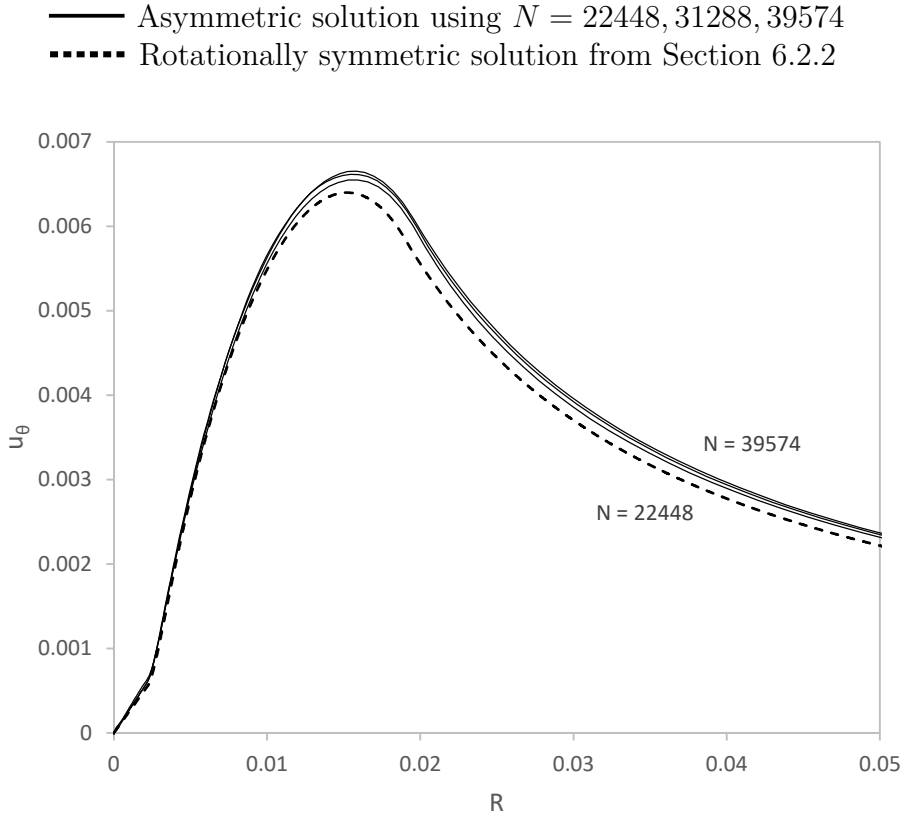

Source: The author.

ures 38 and 39, respectively, and correspond to Figures 35 and 36, which were obtained with the polar formulation.

We see from Figure 38 that the numerical approximations of u_θ converge to a limit function as the mesh is refined. Near the origin, this limit function is linear with respect to R. This linear behavior is similar to the linear behaviors observed in Figures 20b and 35. As we move away from the origin, we see that this limit function remains close to the rotationally symmetric solution.

In Figure 39 we see that the numerical approximations converge to a limit function that is very close to the unconstrained solution, given by (5.28), away from the origin and is very similar to the numerical approximations presented in Figures 19b and 36. Thus, the results of Figures 38 and 39 are in very good agreement with the results presented in section 6.2.2 for the rotationally symmetric solution, which indicates the validity of the numerical approximation of both the rotationally symmetric and the asymmetric solutions.

In summary, by using both the polar and the Cartesian formulations, the numerical

Figure 39 – Field $r(R) - R$ for the asymmetric solution obtained using the Cartesian formulation, the radially symmetric solution and the unconstrained solution.

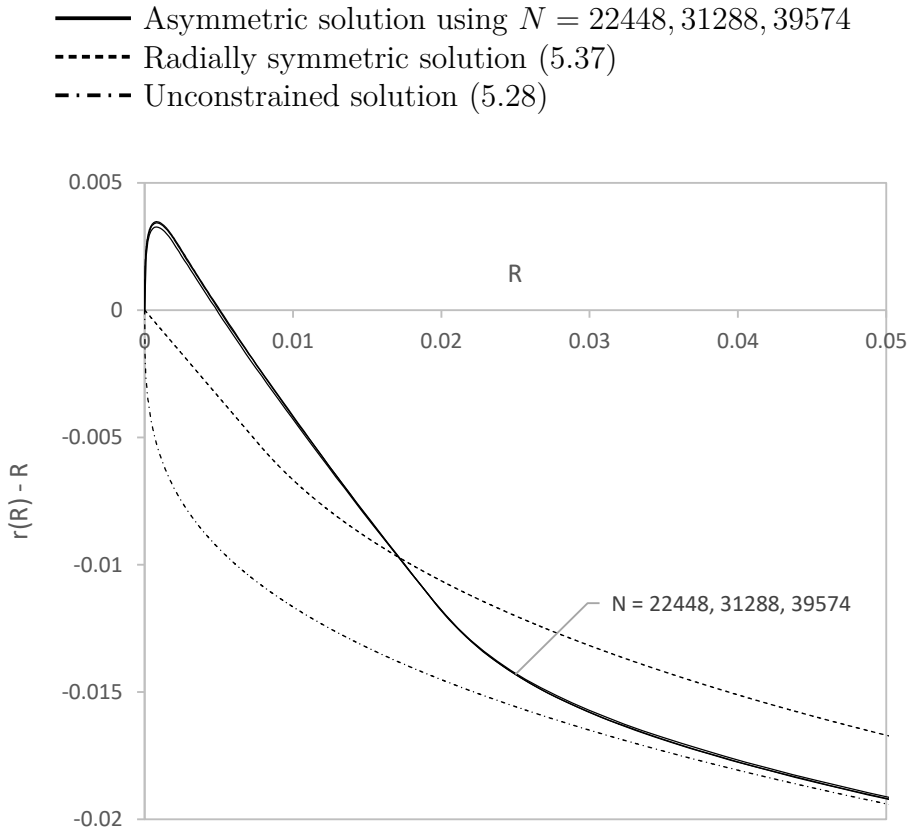

Source: The author.

approximations of the asymmetric solution having the form (6.15) do not seem to depend on the polar angle Θ. In addition, there is no evidence of the existence of a third solution, which could, for instance, depend on the angle Θ.

6.2.6 Numerical remarks

The exposition of Section 6.2.5 is focused on determining asymmetric minimizers for the constrained minimization problem (3.62) and on confirming the numerical results of Section 6.2.2, which were obtained based on the assumption that a minimizer of the constrained minimization problem (3.62) is rotationally symmetric. We continue this analysis by discussing the influence of initial parameters, such as the initial penalty parameter δ_0 and the initial guess $\mathbf{s}_0$, and by presenting the case of convergence difficulties mentioned in Section 6.2.2.

Concerning the initial guess $\mathbf{s}_0$, recall from Section 6.2.1 that $\mathbf{s}_0$ obtained from the solution of the isotropic disk problem, for which $u_\theta^0 = 0$, yields the radially symmetric solution of the constrained minimization problem, regardless of the mesh refinement.

By considering small, but still large enough perturbations u_θ^0, we are able to find the rotationally symmetric solution. These perturbations depend on the mesh refinement and the shear stiffness c_{66}, so that the minimum perturbation that is necessary to find the rotationally symmetric solution decreases as the mesh is refined or c_{66} decreases. In particular, the combination of a very fine mesh and a low value of c_{66} yields convergence of the numerical procedure to the rotationally symmetric solution for very small perturbations u_θ^0.

In fact, we believe that Fosdick, Freddi and Royer-Carfagni (2008) introduced this perturbation when they approximated the circular boundary of the domain with quadratic polynomials from their isoparametric finite element discretization of the minimization problem using elements $\mathcal{Q}_2$. Thus, a very fine mesh and a low value of c_{66} was needed to find their asymmetric solution. On the other hand, a coarser mesh and a higher value of c_{66} gave them the radially symmetric solution. We believe that the same argument applies for our asymmetric results regarding the Cartesian formulation shown in Figures 38 and 39, where we use $u_\theta^0 = 0$. The approximation of the circular contour of the disk by 256 segments of straight lines introduced a perturbation that is analogous to $u_\theta^0 \neq 0$. In addition, because we can control these perturbations, we are able to find rotationally symmetric solutions with a coarse mesh of 256 elements, as shown in Figure 20, and higher values of c_{66}, which was verified but not shown in this work.

Recall from Section 4.1 that we solve a sequence of minimization problems parameterized by the penalty parameter δ, which must be taken from an increasing sequence of values. We have observed that the initial penalty parameter δ_0 also influences the minimum perturbation required for the convergence to the rotationally symmetric solution. For instance, consider the results presented in Section 6.2.2 for $N = 256$. There, we used $\delta_0 = 10^{-3}$ and we had that $u_\theta^0 = 10^{-5}$ was the minimum perturbation necessary to obtain the rotationally symmetric solution. However, we have verified that if we take $\delta_0 = 10^{-4}$, then the minimum perturbation necessary increases to $u_\theta^0 = 10^{-4}$. In fact, by changing δ_0, we change the functional to be minimized in the first minimization problem, which then can lead the numerical procedure to converge to another minimum.

Although the tangential displacements presented in the previous sections were always positive, tangential displacements with opposite signs are also possible and correspond to the same total potential energy. It is possible to obtain either case by changing the value of the perturbation u_θ^0. A positive value of u_θ^0 will, in general, lead to convergence to a positive tangential displacement u_θ. We have observed, however, that it may also lead to convergence to a negative value of u_θ. In this case, since the total potential energy is the same, we have inverted the sign of u_θ for better visualization of results.

Finally, we present a case of convergence difficulty mentioned in Section 6.2.2. For that, consider the mesh parameterized by $h_0 = 10^{-10}$ introduced in Section 6.2.1. In that

section, the combination of $\delta_0 = 10^{-6}$ and $u_\theta^0 = 10^{-10}$ led the numerical procedure to converge to the rotationally symmetric solution. However, for some particular combinations of δ_0 and u_θ^0, the numerical procedure can converge to a displacement field that, in a small region next to the origin, is very close to the radially symmetric solution given by (5.37) and, in the rest of the domain, approaches the rotationally symmetric solution from Section 6.2.2. We argue that this displacement field is an artifact of the numerical procedure and not the approximation of a minimizer, because it is not obtained from a converging sequence of results. The artifact we present below is for the particular case obtained by considering $\delta_0 = 10^{-3}$, instead of $\delta_0 = 10^{-6}$ in the example above. Other combinations of parameters may also yield numerical artifacts in the sense explained above and are, therefore, disregarded in this work.

In Figure 40 we show the radial displacement of a numerical artifact (solid line), the unconstrained solution given by (5.28) (dash-dotted line) and the radially symmetric solution given by (5.37) (dashed line). Figure 40a refers to the entire interval $(0, R_e)$ and Figure 40b refers to the interval $(0, 0.00005)$. We see from Figure 40a that the radial displacement is very close to the unconstrained solution, being similar to what is shown Figure 18a. In Figure 40b, we see that there is a small region close to the origin where u_r of the numerical artifact is very close to the radially symmetric solution. Then, as we move away from the origin, the numerical artifact approaches the unconstrained solution.

In Figure 41 we show the tangential displacement of the artifact of the numerical procedure. Similarly as before, Figure 41a refers to the entire interval $(0, R_e)$ and Figure 41b refers to the interval $(0, 0.00005)$. We see from Figure 41a that the graph of the tangential displacement is similar to the graph of the rotationally symmetric solution presented in Figure 20a. Similarly to Figure 40b, in Figure 41b, we also identify a small region next to the origin where the numerical artifact is very close to the radially symmetric solution. In this case, u_θ is null in this region. Then, as we move away from the origin u_θ of the numerical artifact assumes positive values. Comparing Figures 40b and 41b, we see that the region next to the origin mentioned above coincides in both figures. For this particular example, this region was discretized by 15 finite elements.

6.3 Analytical results and discussion

In Section 6.2 we used a numerical procedure to find approximate minimizers of the problem (3.62) together with (3.61) and (3.63) for the case of an anisotropic disk subjected to an imposed displacement on its boundary. The numerical results indicate that the minimizers are, at most, rotationally symmetric, having the form (6.1). Radially symmetric minimizers, which have the form (5.3) and for which $u_\theta \equiv 0$, are, clearly, particular cases of (6.1). They also indicate that there exists a subregion $\mathcal{B}_>$, defined in (3.65a), composed of an inner circle of radius R_a and an outer annulus with both inner radius $R_b > R_a$ and

Figure 40 – Radial displacement u_r in (a) $(0, 1)$ and (b) $(0, 0.00005)$ for ...

Artifact of the numerical procedure
Radially symmetric solution (5.37)
Unconstrained solution (5.28)

(a) Entire interval

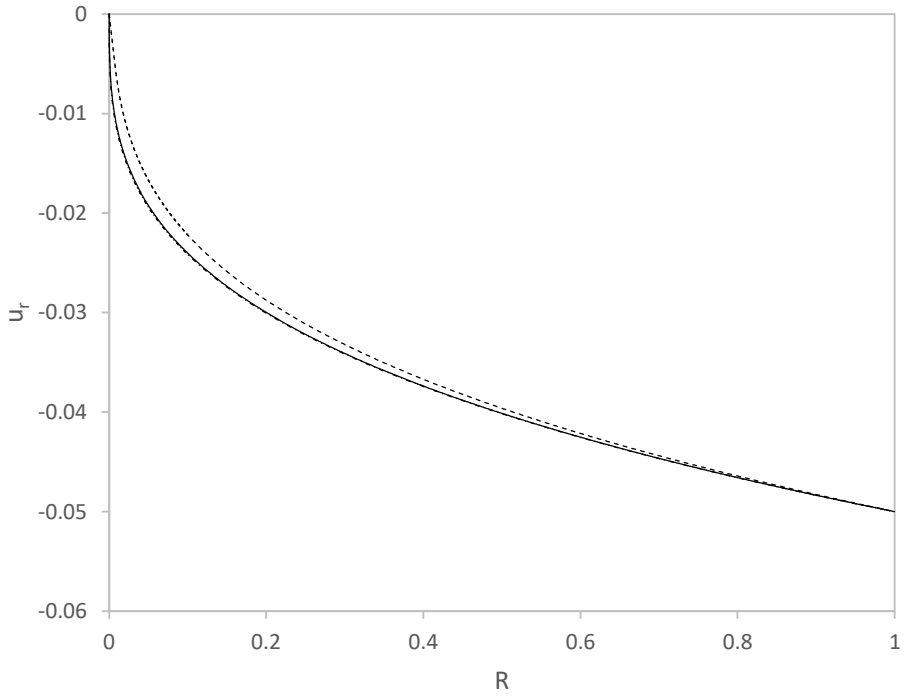

(b) Neighborhood of the origin

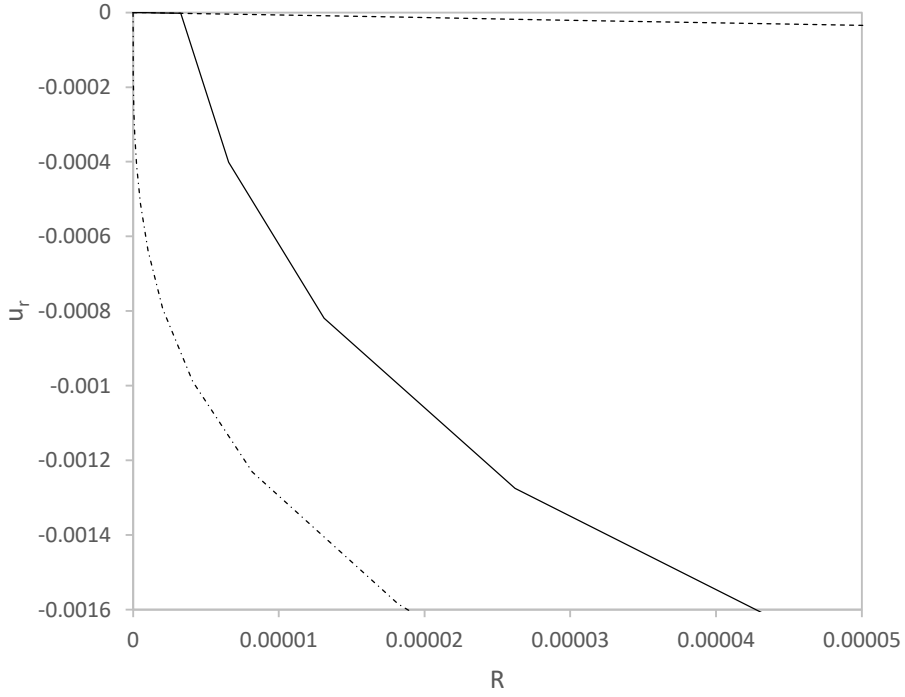

Source: The author.

Figure 41 – Tangential displacement u_θ of the artifact of the numerical procedure.

(a) Entire interval

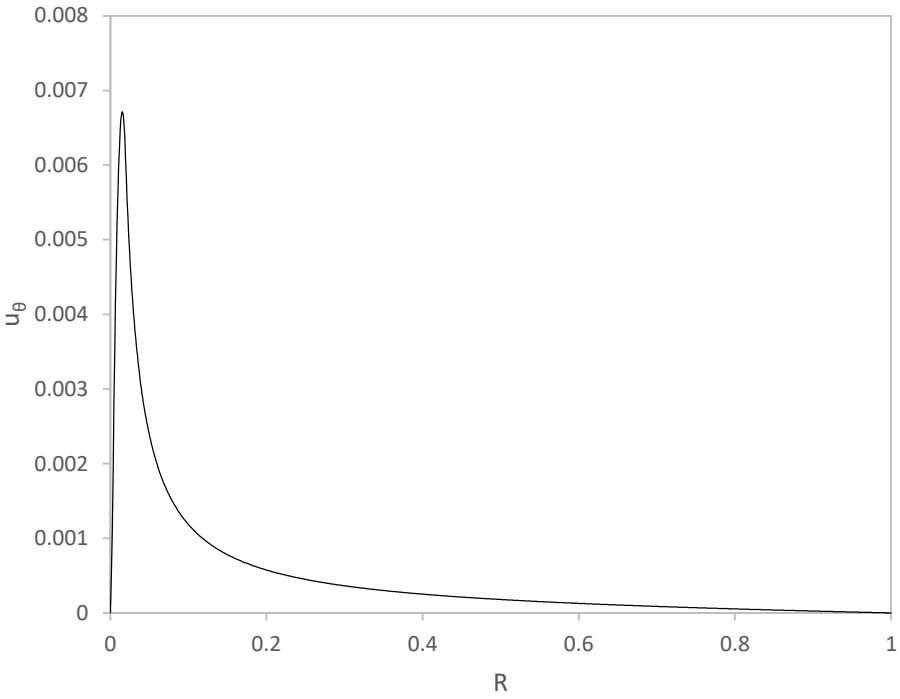

(b) Neighborhood of the origin

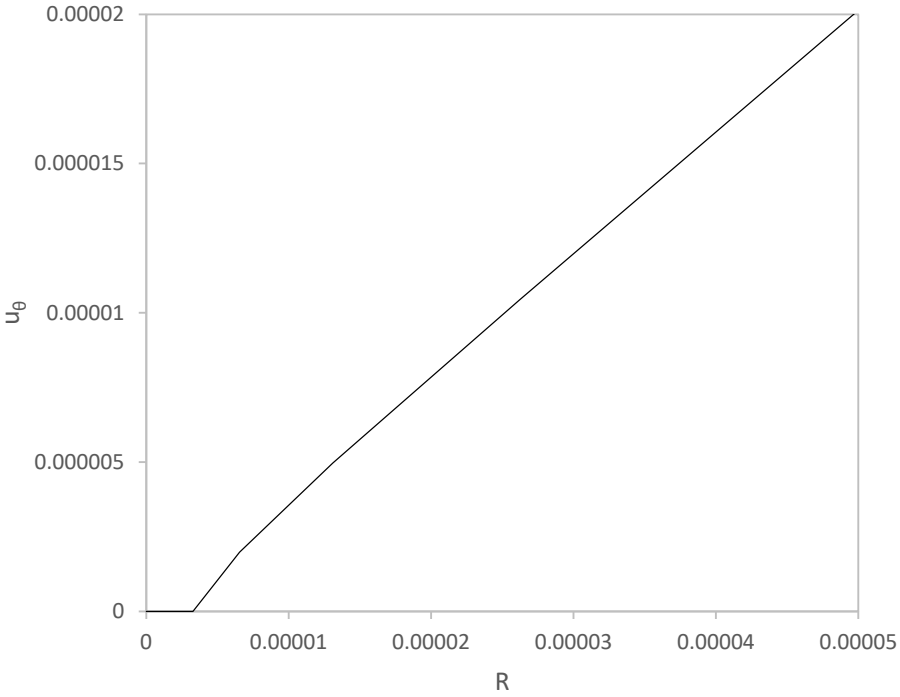

Source: The author.

outer radius R_e. In between the inner circle and the outer annulus there exists a subregion $\mathcal{B}_=$, defined in (3.65b), in the form of an annulus.

In this section we use a semi-analytical method to verify these findings. The method consists of, first, assuming that there exists a displacement field $\mathbf{u}^*$ having the form (6.1). We then substitute $\mathbf{u}^*$ into (3.64), where the components of $\mathbb{C}$ are given in (5.1), and the resulting expressions into (3.66). The equation (3.66a) yields linear ordinary differential equations of second-order that can be easily solved to obtain expressions for u_r and u_θ that depend on integration constants, some of which can be determined from the imposition of the kinematic condition $\mathbf{u}^*(\mathbf{0}) = \mathbf{0}$ and the displacement condition on the boundary of the disk. The other integration constants are, in principle, determined from the jump condition (3.68), which depends on the solution of the equation (3.66b) for the determination of $\mathbf{u}^*$ in the subregion $\mathcal{B}_=$. The resulting equation, however, has no known solution. Instead, we determine the integration constants by using numerical approximations of u_r and u_θ in $\mathcal{B}_>$. In addition, we use the injectivity constraint $\det(\mathbf{1} + \nabla\mathbf{u}^*) = \varepsilon$ to obtain two equations from which we can determine the values of R_a and R_b. These values are then compared to corresponding values obtained numerically. Below we present details of the semi-analytical method outlined above.

Recall from Section 3.6.2 that the Euler-Lagrange equations of the constrained minimization problem (3.62) - (3.63) are given by (3.66) together with the boundary and jump conditions given by (3.67) and (3.68), respectively.

In polar coordinates, the divergence of a second-order tensor field

$$\mathbf{A} = A_{rr}\,\mathbf{e}_r \otimes \mathbf{e}_r + A_{\theta\theta}\,\mathbf{e}_\theta \otimes \mathbf{e}_\theta + A_{r\theta}\,\mathbf{e}_r \otimes \mathbf{e}_\theta + A_{\theta r}\,\mathbf{e}_\theta \otimes \mathbf{e}_r \tag{6.39}$$

is given by

$$\operatorname{Div}\mathbf{A} = \left[A_{rr,R} + \frac{1}{R}\left(A_{r\theta,\Theta} + A_{rr} - A_{\theta\theta}\right)\right]\mathbf{e}_r + \left[A_{r\theta,R} + \frac{1}{R}\left(A_{\theta\theta,\Theta} + A_{r\theta} + A_{\theta r}\right)\right]\mathbf{e}_\theta. \tag{6.40}$$

Using (6.40), assuming rotational symmetry of the displacement field in the form (6.1), and using the generalized Hooke's Law (3.60a), where $\mathbb{C}$ has a matrix representation given by (5.1) in Voight notation and $\mathbf{E}$ is given by (6.2) and (6.3), the vector equations (3.66) can be written as the scalar equations

$$\begin{cases} c_{11}\,u_r'' + c_{11}\,\dfrac{u_r'}{R} - c_{22}\,\dfrac{u_r}{R^2} = 0 \\ u_\theta'' + \dfrac{u_\theta'}{R} - \dfrac{u_\theta}{R^2} = 0 \end{cases} \qquad \text{in } \mathcal{B}_> \tag{6.41}$$

and

$$\begin{cases} c_{11}\,u_r'' + c_{11}\,\dfrac{u_r'}{R} - c_{22}\,\dfrac{u_r}{R^2} - \lambda'\left(1 + \dfrac{u_r}{R}\right) = 0 \\ u_\theta'' + \dfrac{u_\theta'}{R} - \dfrac{u_\theta}{R^2} + \dfrac{\lambda'}{c_{66} + \lambda}u_\theta' = 0 \end{cases} \qquad \text{in } \mathcal{B}_=. \tag{6.42}$$

Based on the results of Figure 24, we assume that the local injectivity constraint is active in

$$\mathcal{B}_{=} = \{\mathbf{X} = R\,\mathbf{e}_r \in \mathcal{B} \mid R_a < R < R_b\} \tag{6.43}$$

and inactive in $\mathcal{B}_{>} = \mathcal{B}^a_{>} \cup \mathcal{B}^b_{>}$, where

$$\mathcal{B}^a_{>} = \{\mathbf{X} = R\,\mathbf{e}_r \in \mathcal{B} \mid 0 < R < R_a\}\,, \qquad \mathcal{B}^b_{>} = \{\mathbf{X} = R\,\mathbf{e}_r \in \mathcal{B} \mid R_b < R < R_e\}\,, \tag{6.44}$$

for some values of R_a and $R_b > R_a$ in $(0, R_e)$, which are not yet determined.

The solution of (6.41) is given by

$$\begin{cases} u_r(R) = C_1\,R^k \\ u_\theta(R) = C_2\,R \end{cases} \qquad \text{in } \mathcal{B}^a_{>}, \tag{6.45}$$

where the kinematic conditions $u_r(0) = u_\theta(0) = 0$ have been imposed, and

$$\begin{cases} u_r(R) = C_3\,R^k + C_4\,R^{-k} \\ u_\theta(R) = C_5\,R + \dfrac{C_6}{R} \end{cases} \qquad \text{in } \mathcal{B}^b_{>}, \tag{6.46}$$

where C_i, $i = 1, 2, 3, ..., 6$ are constants of integration that still need to be determined. We observe from (6.45b) that the tangential displacement is a linear function of R in the vicinity of the origin, as predicted by our numerical solution presented in Section 6.2. By applying the boundary conditions $u_r(R_e) = \bar{u}_r$ and $u_\theta(R_e) = \bar{u}_\theta$, we can express C_4 and C_6 in terms of C_3 and C_5, respectively. Then, (6.46) can be rewritten as

$$\begin{cases} u_r(R) = C_3\,R^k + (\bar{u}_r\,R_e^k - C_3\,R_e^{2k})\,R^{-k} \\ u_\theta(R) = C_5\,R + \dfrac{\bar{u}_\theta\,R_e - C_5\,R_e^2}{R} \end{cases} \qquad \text{in } \mathcal{B}^b_{>}. \tag{6.47}$$

Since $\det(\mathbf{1} + \nabla\mathbf{u}) = \varepsilon$ in $\mathcal{B}_{=}$, it follows from (6.6) that

$$(1 + u_r')\left(1 + \frac{u_r}{R}\right) + u_\theta'\,\frac{u_\theta}{R} = \frac{1}{2R}\,\frac{d}{dR}\left[(R + u_r)^2 + u_\theta^2\right] = \varepsilon. \tag{6.48}$$

The second equality in (6.48) can be rewritten as

$$\frac{1}{2}\,g' + \frac{1}{2R}\,g = \varepsilon, \qquad g \coloneqq \frac{1}{R}\left[(R + u_r)^2 + u_\theta^2\right]. \tag{6.49}$$

The general solution of (6.49) is given by

$$g(R) = \varepsilon R + \frac{C_7}{R}, \tag{6.50}$$

where C_7 is a constant of integration. From the definition of $g(R)$, in (6.49b), it follows from (6.50) that

$$(R + u_r)^2 + u_\theta^2 = \varepsilon R^2 + C_7 \qquad \text{in } \mathcal{B}_{=}. \tag{6.51}$$

To obtain a closed-form solution in $\mathcal{B}_=$, one must solve the nonlinear system of differential equations given by (6.42) and (6.51) for $u_r(R)$, $u_\theta(R)$ and $\lambda(R)$. In this work, we do not solve this system. Instead, we use the above results together with the numerical results presented in Section 6.2 to obtain approximate values for the constants of integration C_i, $i = 1, 2, 3, 5, 7$ and the radii R_a and R_b. For that, first, we isolate the constants of integration in (6.45), (6.47) and (6.51), yielding

$$C_1 = u_r/R^k \qquad \text{in } \mathcal{B}^a_>, \tag{6.52a}$$

$$C_2 = u_\theta/R \qquad \text{in } \mathcal{B}^a_>, \tag{6.52b}$$

$$C_3 = \frac{u_r - \bar{u}_r\,(R_e/R)^k}{R^k - (R_e^2/R)^k} \qquad \text{in } \mathcal{B}^b_>, \tag{6.52c}$$

$$C_5 = \frac{u_\theta - \bar{u}_\theta\,R_e/R}{R - R_e^2/R} \qquad \text{in } \mathcal{B}^b_>, \tag{6.52d}$$

$$C_7 = (R + u_r)^2 + u_\theta^2 - \varepsilon R^2 \qquad \text{in } \mathcal{B}_=. \tag{6.52e}$$

Next, we use the finite element approximations of u_r and u_θ presented in Section 6.2 to evaluate approximations of C_i, which we call $\hat{C}_i^N(R)$, $i = 1, 2, 3, 5, 7$, where N is the number of finite elements in a given mesh. We then expect that $\hat{C}_i^N(R)$ approaches C_i as N increases.

In Figure 42 we show curves of $\hat{C}_i^N(R)$, $i = 1, 2, 3, 5, 7$, obtained from (6.52a-e) by considering finite element approximations of both u_r and u_θ. Similar to the finite element discretization discussed in Section 6.2.3, we have used non-uniform meshes of $N = 600\,q$ linear finite elements, where, here, $q \in \{4, 16, 64, 256, 1024\}$, distributed in three regions: $375\,q$ elements in $0 < R < 0.07\,R_e$, $125\,q$ elements in $0.07\,R_e < R < 0.46\,R_e$ and $100\,q$ elements in $0.46\,R_e < R < R_e$. We also consider the same geometrical and material parameters of Section 6.2.2, which are given by $c_{11} = 10^5$, $c_{22} = 10^4$, $c_{12} = 10^3$, $c_{66} = 10^3$, $\bar{u}_r = -0.05$, $\bar{u}_\theta = 0$, $R_e = 1$ and $\varepsilon = 0.1$.

Now, recall from the discussion of Figure 24 that the radii R_a and R_b have the approximate values of 0.0022 and 0.0190, respectively. We use this information in Figure 42 to define the upper values of R in the graphs. Thus, in Figures 42a and 42b we show $\hat{C}_1^N(R)$ and $\hat{C}_2^N(R)$, respectively, versus R in the interval $(0, 0.003)$. In Figures 42c and 42d we show $\hat{C}_3^N(R)$ and $\hat{C}_5^N(R)$, respectively, versus R in the interval $(0, 1)$, and in Figure 42e we show $\hat{C}_7^N(R)$ versus R in the interval $(0, 0.02)$. We see from these figures that, in the intervals where the expressions (6.52a-e) are defined, the functions $\hat{C}_i^N(R)$ converge to limit constant functions as q and, consequently, N increases. In the particular case of Figure 42a, we see that $\hat{C}_1^N(R)$ is nearly constant outside a small neighborhood of the origin and that the size of this neighborhood tends to zero as N increases. This is due to the singular behavior of the radial displacement (6.45a) at the origin, since $k < 1$. The convergence results observed in Figure 42 indicate that there is very good agreement

between analytical and numerical results, allowing us to use the numerical results to determine the approximate values of the constants of integration.

For that, we first determine numerical approximations of the radii R_a and R_b, which we call R_a^N and R_b^N, respectively, where we recall from above that N is the number of finite elements.

Recall from the discussion of the Figure 24 in Section 6.2.2 that, as we move away from the origin, the determinant of the deformation gradient of the numerical solution, $J(R)$, decreases, oscillates above $\varepsilon = 0.1$ in the approximate interval $(0.0022, 0.0190)$ and then increases, reaching a value close to the unit at $R = R_e$. The values 0.0022 and 0.0190 are, therefore, approximate values of R_a and R_b, respectively. Below we present a criterion to evaluate these approximations as limits of a sequence of values of R_a^N and R_b^N as N tends to infinity.

Let R_i, $i = 1, 2, 3, ..., N_Q$, denote the position of the i-th quadrature point used in the numerical integrations, where N_Q is the total number of quadrature points distributed along the mesh. Then, based on the behavior of J in Figure 24, we define R_a^N as the smallest value of R_i for which the sequence $\{J(R_{i-1}), J(R_i), J(R_{i+1})\}$ is not strictly increasing or strictly decreasing. Similarly, we define R_b^N as the largest value of R_i for which the sequence $\{J(R_{i-1}), J(R_i), J(R_{i+1})\}$ is not strictly increasing or strictly decreasing. In this way, R_a^N and R_b^N are the starting and ending points, respectively, of the interval where J oscillates, which, as Figure 24 shows, corresponds to the region where the constraint is active.

In Table 3 we show the values of R_a^N and R_b^N obtained for each one of the five meshes using the above criterion. We see from this table that the change in value of both R_a^N and R_b^N is small and decreases as we refine the mesh.

Using the values of R_a^N and R_b^N presented in Table 3 and the expressions in (6.52), we now use numerical approximations for the displacement field to define numerical approximations for the constants of integration C_i, $i = 1, 2, 3, 5, 7$, which we denote as C_i^N.

We define C_i^N as the mean value of the approximation $\hat{C}_i^N(R)$ evaluated at certain mesh nodes. Recall from above that $\hat{C}_i^N(R)$ is evaluated from (6.52) by using numerical

Table 3 – Radii R_a^N and R_b^N for each mesh parameter q.

	$q = 4$	$q = 16$	$q = 64$	$q = 256$	$q = 1024$
R_a^N	0.002292	0.002215	0.002184	0.002174	0.002171
R_b^N	0.018859	0.018983	0.019037	0.019057	0.019066

Source: The author.

Figure 42 – $\hat{C}_i^N(R)$, $i = 1, 2, 3, 5, 7$, versus radius using the numerical solution obtained with the meshes parameterized by $q = 4, 16, 64, 256, 1024$.

(a) $\hat{C}_1^N(R) \times R \in (0, 0.003)$

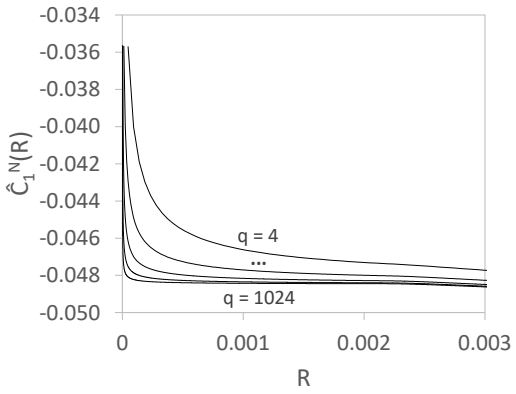

(b) $\hat{C}_2^N(R) \times R \in (0, 0.003)$

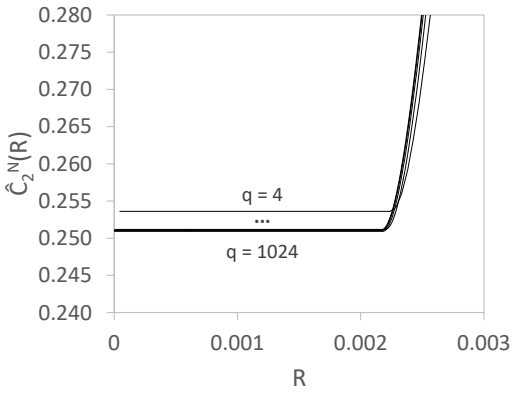

(c) $\hat{C}_3^N(R) \times R \in (0, 1)$

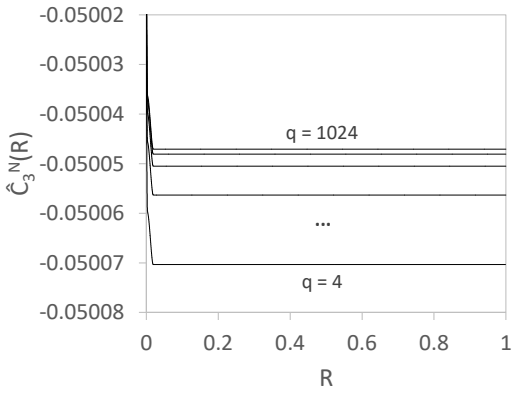

(d) $\hat{C}_5^N(R) \times R \in (0, 1)$

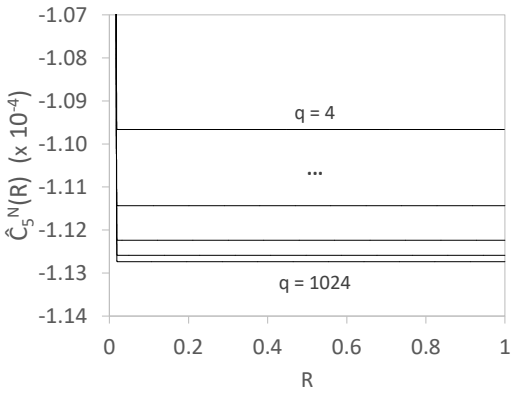

(e) $\hat{C}_7^N(R) \times R \in (0, 0.02)$

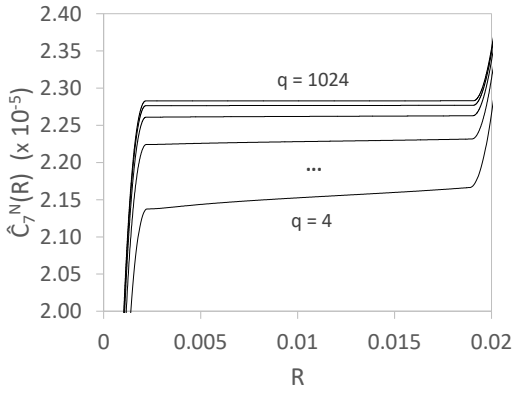

Source: The author.

approximations of u_r and u_θ that were obtained from a finite element discretization with N elements. The mesh nodes where $\hat{C}_i^N(R)$ is evaluated belong to the interval of definition of the corresponding expression in (6.52). We then have that

$$\begin{aligned}
C_1^N &\coloneqq \frac{1}{M_>^a}\sum_i \hat{C}_1^N(R_i) \qquad \forall i \in \{1,2,3,...,M\} \mid R_i \in (0, R_a^N),\\
C_2^N &\coloneqq \frac{1}{M_>^a}\sum_i \hat{C}_2^N(R_i) \qquad \forall i \in \{1,2,3,...,M\} \mid R_i \in (0, R_a^N),\\
C_3^N &\coloneqq \frac{1}{M_>^b}\sum_i \hat{C}_3^N(R_i) \qquad \forall i \in \{1,2,3,...,M\} \mid R_i \in (R_b^N, R_e),\\
C_5^N &\coloneqq \frac{1}{M_>^b}\sum_i \hat{C}_5^N(R_i) \qquad \forall i \in \{1,2,3,...,M\} \mid R_i \in (R_b^N, R_e),\\
C_7^N &\coloneqq \frac{1}{M_=}\sum_i \hat{C}_7^N(R_i) \qquad \forall i \in \{1,2,3,...,M\} \mid R_i \in (R_a^N, R_b^N).
\end{aligned} \tag{6.53}$$

where R_i is the position of the i-th mesh node and M, $M_>^a$, $M_=$ and $M_>^b$ are the number of mesh nodes in the intervals $(0, R_e)$, $(0, R_a^N)$, (R_a^N, R_b^N), and (R_b^N, R_e), respectively.

In Figure 43 we show graphs of C_i^N, $i = 1, 2, 3, 5, 7$, given by (6.53), versus the base 2 logarithm of the mesh parameter $q \in \{4, 16, 64, 256, 1024\}$. We see from these graphs that the numerical approximations C_i^N tend to a limit value as the mesh is refined. In addition, their change in value from the coarsest to the most refined mesh ranges, approximately, from 0.05%, for C_3^N to 5% for C_1^N. In view of the large difference in the number of finite elements used in both the coarsest and the most refined mesh, we consider that this range of values is small.

Next, we use the continuity condition of the displacement field across the boundary of $\mathcal{B}_=$ and the expressions (6.45), (6.47), and (6.51) together with the values of C_i^N, $i = 1, 2, 3, 5, 7$, shown in Figure 43 to find approximations of R_a and R_b, which we later denote by R_a^A and R_b^A, where the superscript 'A' stands for 'analytical'. We want to compare these values with the values of R_a^N and R_b^N that were found from numerical results. For this, we evaluate (6.51) at $R = R_a$ and $R = R_b$, where u_r and u_θ are given by (6.45) at $R = R_a$ and by (6.47) at $R = R_b$. In addition, we replace the constants of integration C_i, $i = 1, 2, 3, 5, 7$, by their respective approximations C_i^N, $i = 1, 2, 3, 5, 7$. We then have that imposition of continuity on $R = R_a$ yields

$$\left(C_1^N {R_a}^k + R_a\right)^2 + C_2^N\, {R_a}^2 - \varepsilon {R_a}^2 - C_7^N = 0 \tag{6.54}$$

and on $R = R_b$ yields

$$\left(C_3^N {R_b}^k + R_b + \frac{\bar{u}_r {R_e}^k - C_3^N {R_e}^{2k}}{{R_b}^k}\right)^2 + \left(C_5^N R_b + \frac{R_e \bar{u}_\theta - C_5^N {R_e}^2}{R_b}\right)^2 - \varepsilon {R_b}^2 - C_7^N = 0. \tag{6.55}$$

We numerically solve equations (6.54) and (6.55) for R_a and R_b, respectively, and for each one of the five meshes parameterized by q.

Figure 43 – Constants C_i^N, $i = 1, 2, 3, 5, 7$, versus the base 2 logarithm of the mesh parameter $q = 4, 16, 64, 256, 1024$.

(a) C_1^N

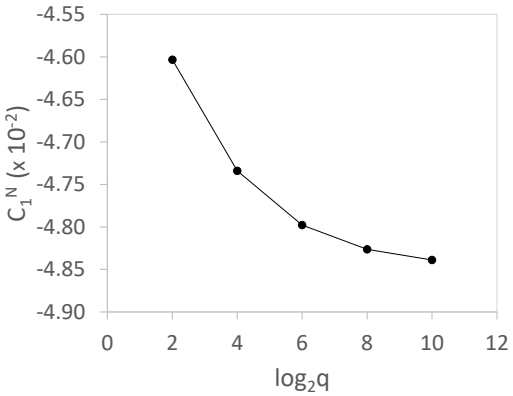

(b) C_2^N

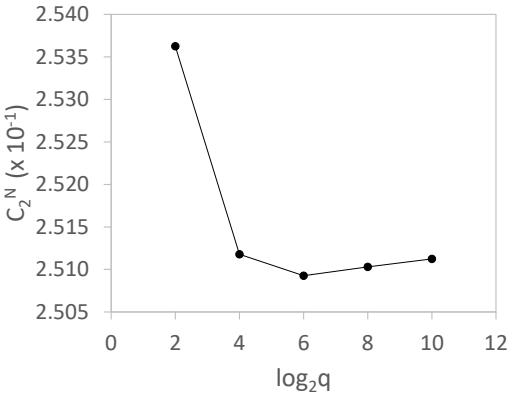

(c) C_3^N

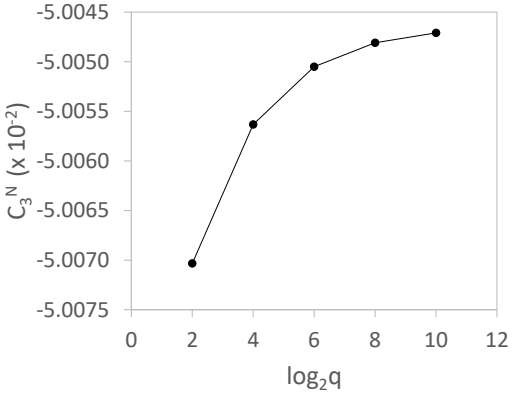

(d) C_5^N

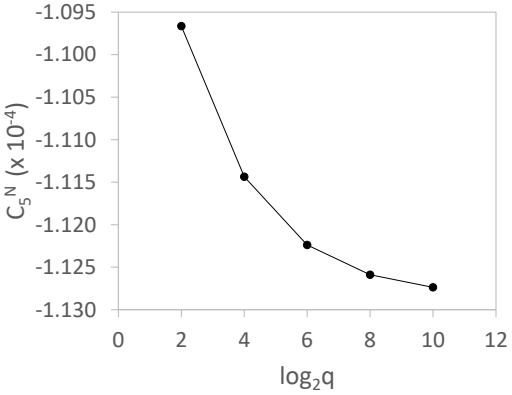

(e) C_7^N

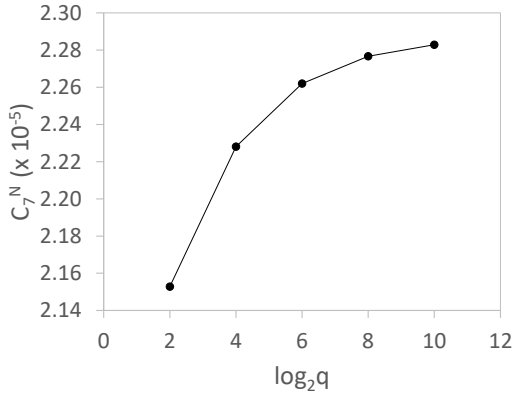

Source: The author.

In Figure 44 we show graphs of approximations of R_a and R_b versus the base 2 logarithm of the mesh parameter $q \in \{4, 16, 64, 256, 1024\}$. The solid lines and the dashed lines represent approximations of both R_a and R_b that were obtained by, respectively, the semi-analytic method and the finite element method. We see from Figure 44a that both R_a^A and R_a^N converge to the same limit value as q increases, i.e, as we refine the mesh. For Figure 44b, besides the convergence of R_b^A and R_b^N to the same limit value, we also see that both curves are close to each other for all the considered values of q. These convergence results indicate again the very good agreement between analytical and numerical results, which validates the assumption of rotationally symmetric displacement field presented in Section 6.2.

Figure 44 – Approximations of the radii R_a and R_b versus the base 2 logarithm of the mesh parameter $q = 4, 16, 64, 256, 1024$.

(a) R_a^A and R_a^N

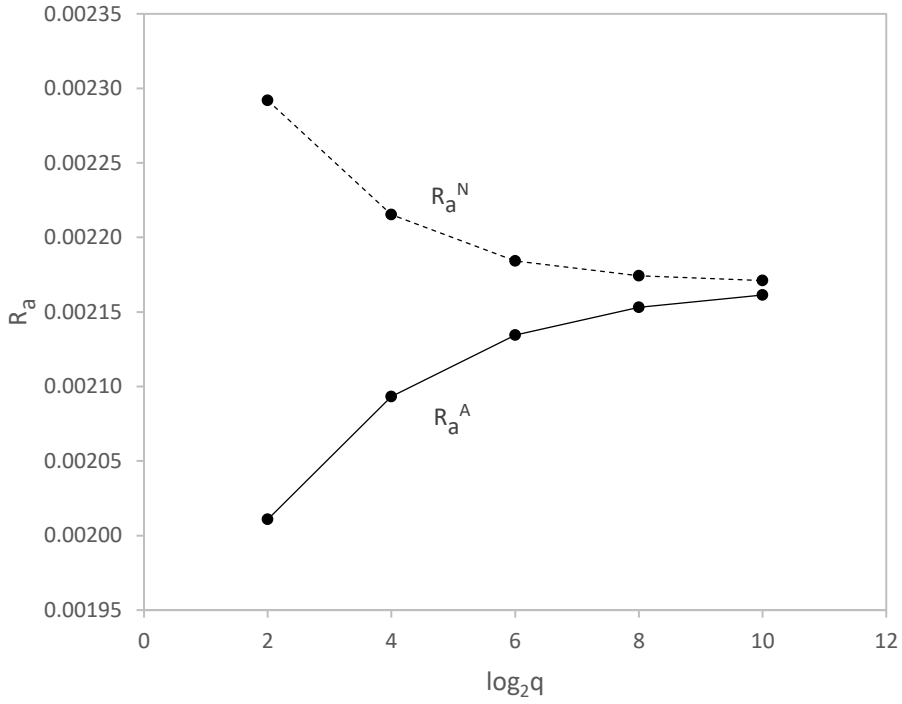

(b) R_b^A and R_b^N

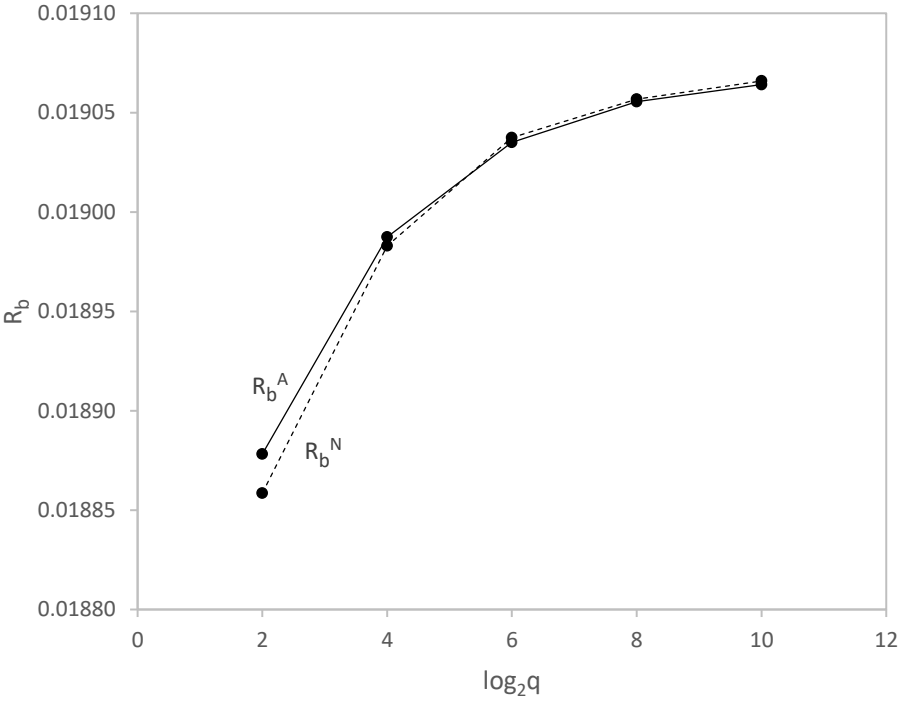

Source: The author.

7 FINAL CONSIDERATIONS

In this work we have studied some boundary value problems in mechanics known to have solutions that predict material overlapping in the context of the classical linear elasticity. To prevent this anomalous behavior, we have considered a constrained minimization theory proposed by Fosdick and Royer-Carfagni (2001), which consists of minimizing the total potential energy functional of classical linear elasticity $\mathcal{E}$ subject to the local injectivity constraint.

We have applied a numerical procedure based on an interior penalty formulation together with a standard finite element method to search for a displacement field $\mathbf{u}$ that minimizes $\mathcal{E}[\mathbf{u}]$ subject to the local injectivity constraint $J := \det(\mathbf{1} + \nabla\mathbf{u}) \geq \varepsilon > 0$. We have implemented a C++ code within the deal.II programming environment and simulated numerically the problems of an anisotropic sphere and an anisotropic disk in equilibrium with no body force and compressed along its boundary in the context of the constrained theory.

Initially, we have considered that the solutions of these problems were radially symmetric and that the boundary was compressed by a uniform normal pressure. We have generated results that are in very good agreement with results found in the literature. These simulations served to validate the numerical scheme based on minimization programming. We then focused on the disk problem and assumed that a secondary solution exists, which is rotationally symmetric. In this case, we have considered that the boundary is compressed by an imposed displacement rather than a uniform normal pressure. Based on the assumption of rotationally symmetric displacement field, we formulated the associated discrete problem in terms of a displacement field having both the radial and tangential components depending on the radius R only. This approach is different from the approach used by Fosdick, Freddi and Royer-Carfagni (2008), who have considered that both components depend on the polar coordinates R and the angle Θ. The main advantage of our approach is that it allows an in-depth investigation of convergence of both the numerical solutions and the influence of different parameters, such as the shear modulus c_{66}, on the behavior of the rotationally symmetric solution at a low computational cost.

Our results clearly suggest that, in order to obtain the secondary solution, a perturbation u_θ^0 to the tangential displacement must be introduced. Then, we obtained convergent results for the rotationally symmetric solution at a low computational cost. The convergent results seem to be in good agreement with results of Fosdick, Freddi and Royer-Carfagni (2008). There are, however, some differences between our results and the results obtained by these authors; mainly with respect to the behavior of the radial displacement u_r away from the center of the disk. The numerical approximations of u_r

obtained in our simulations are very close to u_r obtained from the classical unconstrained solution. On the other hand, the above authors show numerical results indicating that their approximations are very close to u_r obtained from the constrained radially symmetric solution.

To investigate these differences, we have also searched for secondary solutions that are fully asymmetric, that is, both components of $\mathbf{u}$ in polar coordinates depend on both coordinates R and Θ. For that, we have introduced the polar and the Cartesian formulations. In the polar formulation, the domain of integration of the penalized objective function $\mathcal{F}_\delta$ in (4.7) is a rectangle of dimensions $(0, R_e) \times (0, 2\pi)$ and in the Cartesian formulation, this domain is a circle of radius R_e. Even though the polar formulation is simpler to implement and has a lower computational cost than the Cartesian formulation, the latter was used for comparison purposes with the formulation of Fosdick, Freddi and Royer-Carfagni (2008), who have also discretized the circular disk. The numerical results obtained from both formulations indicate that the rotationally symmetric solution is the only possible secondary solution for the anisotropic disk problem. It also confirms the results based on the assumption of rotationally symmetric solution; in particular, the numerical approximations of u_r are indeed very close to u_r obtained from the unconstrained solution away from the origin.

In addition to the three numerical formulations mentioned above, we have introduced a semi-analytical method to find a general expression for the rotationally symmetric solution. It consists of the expressions (6.45), (6.46), and (6.51), where the constants of integration C_i, $i = 1, 2, 3, 5, 7$, are evaluated from numerical results. There is very good agreement between analytical and numerical results. In particular, the analytical results confirm the existence of a linear behavior of the tangential displacement near the origin and the fact that u_r of the rotationally symmetric solution is very close to u_r of the unconstrained solution away from the origin. We have also verified that the approximations of the radii R_a and R_b, which are the endpoints of the interval where $J = \varepsilon$, obtained analytically are in very good agreement with their counterparts obtained numerically.

Other results of interest are discussed below. The total potential energy calculated from the rotationally symmetric solution, here called $\mathcal{E}_s$, is lower than that from the radially symmetric solution, here called $\mathcal{E}_c$. As c_{66} increases, $\mathcal{E}_s$ increases, but seems to be always lower than $\mathcal{E}_c$. In addition, the rotationally symmetric displacement field tends to the radially symmetric displacement field as c_{66} increases. This result confirms the physical intuition that a large c_{66} hinders the rotation of the disk core.

We have also investigated the maximum value of the shear modulus, c_{66}^{max}, for which the rotationally symmetric solution exists for a given mesh. For $c_{66} > c_{66}^{max}$, we could obtain only the radially symmetric solution. Using our most refined mesh, we have obtained $c_{66}^{max} = 1.86 \times 10^5$. However, c_{66}^{max} increases as the mesh is refined and our results

could not indicate if there is a finite c_{66}^{max} as the number of elements in the mesh tends to infinity. In fact, it seems that the radially symmetric solution is the only solution as $c_{66} \to \infty$, which suggests that the rotationally symmetric solution is possible for any positive value of c_{66}. This result is different from what is reported in Fosdick, Freddi and Royer-Carfagni (2008). In their work they could obtain their asymmetric solution only for $c_{66} \leq 2 \times 10^4$. This difference is possibly due to the fact that Fosdick, Freddi and Royer-Carfagni (2008) did not introduce a sufficiently large perturbation to obtain their asymmetric solution for higher values of c_{66}. We believe that their perturbation was due to the approximation of the boundary of the disk by segments of second degree polynomial functions and that it had the role of our perturbation u_θ^0. However, this perturbation was not large enough to make the numerical procedure converge to their asymmetric solution for $c_{66} > 2 \times 10^4$.

We have also investigated the influence of the imposed displacement on the boundary on the existence of the rotationally symmetric solution holding fixed all the other parameters, including c_{66}. Given a mesh, there is a minimum value of the modulus of the imposed radial displacement, $\bar{u}_r^{min}$, below which we could not obtain the rotationally symmetric solution. However, this value of $\bar{u}_r^{min}$ decreases as the mesh is refined. This result could indicate that the rotationally symmetric solution exists for any value of imposed radial displacement $\bar{u}_r < 0$. This aspect of the research remains open and could be addressed in future works together with a further investigation on the existence of a value of c_{66} above which only the radially symmetric solution exists.

Finally, we have used a regular perturbation method to find approximate solutions of the disk problem in the context of the classical linear elasticity theory, and we have verified that these solutions converge to the closed-form solution of the problem as a perturbation parameter tends to zero. The aim of this study is to use this method to investigate more complex problems for which closed-form solutions are not known, such as the investigation of material overlapping in the context of a nonlinear elasticity theory.

REFERENCES

AGUIAR, A.; FOSDICK, R. On the corner behavior of a non-linear elastic wedge under mixed boundary conditions. **International Journal of Non-Linear Mechanics**, v. 66, p. 111–125, nov 2014. ISSN 00207462.

AGUIAR, A. R. Local and global injective solution of the rotationally symmetric sphere problem. **Journal of Elasticity**, v. 84, n. 2, p. 99–129, 2006. ISSN 03743535.

AGUIAR, A. R.; FOSDICK, R. Self-intersection in elasticity. **International Journal of Solids and Structures**, v. 38, n. 28-29, p. 4797–4823, 2001. ISSN 00207683.

AGUIAR, A. R.; FOSDICK, R.; SÁNCHEZ, J. A study of penalty formulations used in the numerical approximation of a radially symmetric elasticity problem. **Journal of Mechanics of Materials and Structures**, v. 3, n. 8, p. 1403–1427, oct 2008. ISSN 1559-3959.

ANTMAN, S. S.; NEGRÓN-MARRERO, P. V. The remarkable nature of radially symmetric equilibrium states of aeolotropic nonlinearly elastic bodies. **Journal of Elasticity**, v. 18, n. 2, p. 131–164, 1987. ISSN 03743535.

ARAVAS, N.; SHARMA, S. An elastoplastic analysis of the interface crack with contact zones. **Journal of the Mechanics and Physics of Solids**, v. 39, n. 3, p. 311–344, jan 1991. ISSN 00225096.

ARNDT, D. et al. The deal.II Library, Version 9.1. **Journal of Numerical Mathematics**, jun 2019. ISSN 1570-2820. Available at: <http://www.degruyter.com/view/j/jnma.just-accepted/jnma-2019-0064/jnma-2019-0064.xml>.

CHRISTENSEN, R. M. Properties of carbon fibers. **Journal of the Mechanics and Physics of Solids**, v. 42, n. 4, p. 681–695, 1994. ISSN 00225096.

CIARLET, P. G. **Mathematical elasicity: Volume I Three-dimensional elasticity**. Amsterdam: Elsevier Science, 1988. (Studies in mathematics and its applications). ISBN 9780444817761.

COMNINOU, M. The interface crack. **Journal of Applied Mechanics**, v. 44, n. 4, p. 631–636, dec 1977. ISSN 0021-8936.

ENGLAND, A. H. A Crack Between Dissimilar Media. **Journal of Applied Mechanics**, v. 32, n. 2, p. 400–402, jun 1965. ISSN 0021-8936.

FOSDICK, R.; FREDDI, F.; ROYER-CARFAGNI, G. Bifurcation instability in linear elasticity with the constraint of local injectivity. **Journal of Elasticity**, v. 90, n. 1, p. 99–126, 2008. ISSN 03743535.

FOSDICK, R.; ROYER-CARFAGNI, G. The constraint of local injectivity in linear elasticity theory. **Proceedings of the Royal Society A: Mathematical, Physical and Engineering Sciences**, v. 457, n. 2013, p. 2167–2187, 2001. ISSN 13645021.

GURTIN, M. E. **An introduction to continuum mechanics**. New York: Academic Press, 1981. ISBN 0-12-309750-9.

HUANG, X. Fabrication and properties of carbon fibers. **Materials**, v. 2, n. 4, p. 2369–2403, dec 2009. ISSN 1996-1944.

JOHN, F. Plane strain problems for a perfectly elastic material of harmonic type. **Communications on Pure and Applied Mathematics**, v. 13, n. 2, p. 239–296, may 1960. ISSN 00103640.

KNOWLES, J. K.; STERNBERG, E. On the singularity induced by certain mixed boundary conditions in linearized and nonlinear elastostatics. **International Journal of Solids and Structures**, v. 11, n. 11, p. 1173–1201, 1975. ISSN 00207683.

LEKHNITSKII, S. G. **Anisotropic plates**. New York: Gordon & Breach, 1968.

MUSKHELISHVILI, N. I. **Some Basic Problems of the Mathematical Theory of Elasticity**. Dordrecht: Springer Netherlands, 1977. ISBN 978-90-481-8245-9.

NAYFEH, A. H. **Introduction to Perturbation Techniques**. New York: Wiley, 1993.

OBEIDAT, K. et al. Numerical analysis of elastic problems with injectivity constraints. In: **European Conference on Computational Mechanics (ECCM-2001)**. Cracow: [s.n.], 2001.

SOKOLNIKOFF, I. **Mathematical theory of elasticity**. 2nd. ed. New York: McGraw-Hill, 1956.

TARN, J. Q. Stress singularity in an elastic cylinder of cylindrically anisotropic materials. **Journal of Elasticity**, v. 69, n. 1-3, p. 1–13, 2002. ISSN 03743535.

TING, T. C. Remarkable nature of radially symmetric deformation of spherically uniform linear anisotropic elastic solids. **Journal of Elasticity**, v. 53, n. 1, p. 47–64, 1998. ISSN 03743535.

WILLIAMS, M. L. On the stress distribution at the base of a stationary crack. **Journal of Applied Mechanics**, v. 24, n. 1, p. 109–114, 1956.

_____. The stresses around a fault or crack in dissimilar media. **Bulletin of the Seismological Society of America.**, v. 49, n. 2, p. 199–204, 1959.

WILLIAMS, M. L.; PASADENA, C. Stress Singularities Resulting From Various Boundary Conditions in Angular Corners of Plates in Extension. **Journal of Applied Mechanics**, v. 19, n. 4, p. 526–528, 1952.